Ministère de l'Enseignement Supérieur et de la Recherche Scientifique
Université Hassiba Benbouali de Chlef
Faculté Technologie
Département Électrotechnique

THÈSE

Présentée pour l’obtention du diplôme de

DOCTORAT

Filière : Génie Électrique
Spécialité : Électrotechnique des Énergies Renouvelable

Par
NABIL OBEIDI

Thème :

CONTRIBUTION À LA MAXIMISATION DE PUISSANCE DANS LES SYSTÈMES PHOTOVOLTAÏQUE

(CONTRIBUTION TO POWER MAXIMIZATION IN PHOTOVOLTAIC SYSTEMS)

Soutenue le 08/10/2023, devant le jury composé de :

Abdelkadir DJAHBAR	Professeure	Université de Chlef	Président
Bachir BELMADANI	Professeure	Université de Chlef	Rapporteur
El hadj BOUNADJA	MCA	Université de Chlef	Examinateur
Abdelkadir BELHADJ DJILALI	MCA	Université de Chlef	Examinateur
Abdelhafidh MOUALDIA	Professeure	Université de Medea	Examinateur
Abdelkrim ALLAG	Professeure	Université d’El oued	Co-encadrant

Acknowledgements

Above all, I thank ‘ALLAH’ for giving me the strength, courage, and will to carry out this modest work.

I would like to thank all those who have helped me, from near or far, for the development of this project, in particular my parents who have devoted their existence to build me, through their love, patience, concern and affection.

I would also like to express deeply and sincerely my thanks and gratitude to Professor BELMADANI Bachir, for having supervised me in the best conditions, for his great advice and for the trust he has shown in me.

I warmly thank Professor ALLAG Abdelkrim, Doctor KERMADI Mostefa, and Professor MKHILEF Saad for their invaluable advice and help. I also want to express my deepest gratitude to all the teachers, without whom we would not have reached this level.

Finally, I would like to thank my family and friends for their encouragement and support during these long years.

Dedications

I would be honoured to dedicate this thesis work to my parents, my wife, my family, my teachers and many close friends. To the two persons that gave me the tools and values necessary to be where I am standing today. I will never finish to thank my father and my mother for all the opportunities they have offered me. For all the teachings that they have told me and for every piece of advice that has come out of their mouth. I am so grateful to them for trusting me that I would do a Good job at the university.

ملخص:

في أنظمة الطاقة الكهروضوئية (PV)، يعد إستعمال تقنية maximum power point tracking (MPPT) عنصرا رئيسيا لضمان إستخراج أقصى طاقة ممكنة من الألواح الكهروضوئية. في الوقت الحاضر، تم اقتراح العديد من تقنيات MPPT المختلفة في الأدبيات باستخدام طرق مختلفة. في هذا العمل، أجرينا أولاً دراسة مقارنة شاملة لتقنيات MPPT الأكثر اعتمادًا. بخلاف ذلك، تم تحليل ودراسة أداء ثلاثة محولات DC-DC نموذجية لوحدة التحكم MPPT بدون اعتماد على مستشعرات التيار من أجل التطبيقات الكهروضوئية. بالإضافة إلى ذلك، يقدم هذا العمل التحكم بدون مستشعر للتيار لمحول buck-boost من أجل تتبع أقصى نقطة طاقة للأنظمة الكهروضوئية. تم أيضًا اقتراح نهج معدل يعمل بدون مستشعر للتيار لتتبع أعظم نقطة للطاقة للأنظمة الكهروضوئية المظللة جزئيًا. تم إنشاء مخطط الطرق المقترح باستخدام دالة موضوعية محددة مسبقًا مشتقة من النموذج الرياضي لمحول DC-DC. من جهة أخرة لتعزيز كفاءة هذه الطرق المقترحة، تم إجراء الأختبارات التجريبية للتحقق من دقة تتبع MPP وGMPP للأنظمة الكهروضوئية في ظل ظروف إشعاعات شمسية موحدة وتحت شروط التظليل الجزئي. تم تنفيذ الخوارزمية المقترحة الأولى باستخدام لوحة Arduino DUE التي تدمج متحكم ARM Cortex-M3 والثانية باستخدام TMS320F240 DSP للوحة dSPACE DS1104. ونتيجة لذلك، فإن كلا الطريقتين المقترحتين توفران تخفيضًا في عبء الحمل الحسابي وتكلفة تنفيذ المستشعر بنسبة 24.3٪ و27.95٪ على التوالي.

الكلمات المفتاحية: النظام الكهروضوئي، التحكم بدون مستشعر للتيار لإستخراج أقصى طاقة ممكنة.

Abstract:

In Photovoltaic (PV) systems, using the maximum power point tracking (MPPT) technique is a main key element for PV systems to guarantee the extraction of the maximum possible power from PV panels. Nowadays, different MPPT techniques have been proposed in the literature using different methods. In this work, we initially performed a comprehensive comparative study of the most adopted MPPT techniques. Otherwise, assessments of DC-DC converters performance for current sensorless-based MPPT controllers in PV applications are studied. This work introduces a current sensorless control of buck-boost converter for maximum power point tracking in photovoltaic applications. Additionally, a modified current sensorless approach for global maximum power point tracking of partially shaded photovoltaic systems is presented too. The proposed methods scheme was established using a predefined objective function derived from the mathematical model of the DC-DC converter for their implementation. Tests are made to verify the tracking accuracy of the MPP and GMPP for PV systems under uniform insolation conditions and partially shaded conditions. The first proposed algorithm was implemented using an Arduino DUE board which integrates an ARM Cortex-M3 MCU, and then the second by the TMS320F240 DSP of dSPACE DS1104 board. The proposed methods have reduced the computation burden and the sensor cost of implementation by 24.3%, and 27.95%, respectively.

Keywords: Photovoltaic (PV) system, Current sensorless-based MPPT controller.

Résumé:

Dans les systèmes photovoltaïques (PV), l'utilisation de la technique de suivi du point de puissance maximale (MPPT) est le principal élément des systèmes PV pour garantir l'extraction de la puissance maximale possible. Aujourd'hui, différentes techniques MPPT ont été proposées dans littérature en utilisant différentes méthodes. Dans ce travail, nous avons d'abord faire une étude comparative complète des techniques MPPT les plus adoptées sur les systèmes PV. En plus, les évaluations des performances des convertisseurs DC-DC pour le contrôleur MPPT sans capteur de courant dans les applications PV sont étudiées. Par la suite, ce travail introduit un contrôle sans capteur de courant du convertisseur buck-boost pour le suivi du point de puissance maximale dans les applications photovoltaïques. De plus, une approche sans capteur de courant modifiée pour le suivi du point de puissance maximale des systèmes photovoltaïques partiellement ombragés est également présentée. Le schéma des methodes proposés en utilisant une fonction objective prédéfinie dérivée du modèle mathématique du DC-DC convertisseur. Différents tests sont effectués pour vérifier la précision du suivi MPP et du GMPP pour les systèmes PV dans des conditions d'ensoleillement uniformes et partiellement ombragés. Le première algorithme proposé a été implémenté à l'aide de la carte Arduino DUE qui intègre un microcontrôleur ARM Cortex-M3 et le deuxième par DSP TMS320F240 de la carte dSPACE DS1104. Les méthodes proposée a réduit la charge de calcul et le coût de mise en œuvre du capteur de 24,3 % et 27,95 %, respectivement.

Mots clés: Système photovoltaïque (PV), contrôleur MPPT sans capteur de courant.

TABLE OF CONTENTS

GENERAL INTRODUCTION

CHAPTER I

LITERATURE SURVEY OF THE PHOTOVOLTAIC SYSTEMS

CHAPTER II

ASSESSMENT OF DC-DC CONVERTER PERFORMANCE FOR CURRENT SENSORLESS-BASED MPPT CONTROLLER FOR PV APPLICATIONS

CHAPTER III

A CURRENT SENSORLESS MPPT CONTROL OF BUCK-BOOST CONVERTER FOR PHOTOVOLTAIC SYSTEMS

CHAPTER IV

MODIFIED CURRENT SENSORLESS APPROACH FOR MAXIMUM POWER POINT TRACKING OF PARTIALLY SHADED PHOTOVOLTAIC SYSTEMS

GENERAL CONCLUSION

APPENDICES

Nomenclature

D: Duty Cycle.

G: Irradiance (W/m^2).

Q: Objective function.

Q_{th}: Threshold value of the objective function.

η: Efficiency.

k: Region number of peak power.

D_{MPP}: Optimal duty cycle.

V_{MPP}: Optimal PV module voltage (V).

V_{PV_mod}: PV module voltage (V).

V_{out}: Output voltage (V).

V_{IN}: Input voltage (V).

I_{out}: Output current (V).

I_{PV_panel}: Current of the PV panel (A).

V_{PV_panel}: Voltage of the PV panel (V).

$D_{\mathrm{k},min}$: Lower duty cycle limits.

$D_{\mathrm{k},max}$: Upper duty cycle limits.

R_{eq}: Equivalent resistance of PV module (Ω).

R_L: Load resistance (Ω).

T_S: Sampling time (mS).

V_{oc_mod}: Open-circuit voltage of the PV module (V).

D_{GMPP}: Duty cycle at GMPP.

P_{GMPP}: PV module power at GMPP (W).

$0.8V_{OC}$: PV module voltage at 80% of the open-circuit voltage (V).

I_{SC}: Short-circuit current (A).

V_{OC}: Open-circuit voltage (V).

V_{MPP}: PV module voltage at MPP (V).

I_{MPP}: PV module current at MPP (A).

n: Number of bypass diodes.

D_S: Step-size.

Φ_D: Small factor of step-size.

i: gradient of recording the state of duty cycle.

$\mathcal{L}$: Lyapunov function.

fs: Switching frequency (kHz).

X: State matrix.

Y: output of state vector.

A: Converter's state space matrix.

u: Input and command vector of the system.

Abbreviations

ADC: Analog to digital conversion.

GMPP: Global maximum power point.

CMM: Continues conduction mode.

LMPP: Local maximum power point.

MCSL: Modified current sensorless.

MPPT: Maximum power point tracking.

PV: Photovoltaic.

PSC: Partial shading condition.

LIST OF FIGURES AND TABLES

1. The figures

2. The tables

GENERAL INTRODUCTION

1. An overview of the research area

The foundation of modern life and an important tool for quick manufacturing operations is electrical energy. Due to the rising demand for energy, the industry encourages research to speed up on alternative energy resources and find solutions to the burden of traditional energy resources with undesirable environmental consequences. Photovoltaic (PV) solar system is one of the most promising renewables among the alternative energy sources available. PV energy is an easily installed and friendly natural resource. In order to generate energy without any gas emissions, PV systems provide clean electricity and their operating service is almost silent. In addition, in terms of its construction, it is easy and requires little maintenance. Large-scale PV systems nowadays become widely used in many countries, and every year the need for such power increases.

Algeria has offered significant aspirational projects to increase the use of renewable energy. In order to provide variety and make a contribution to the utilization of renewable and sustainable energy sources, Algeria country has exploited three categories of them, The first and most commonly used resource of these is solar photovoltaic. Second, concentrated solar power (CSP) which preferred for large-scale renewable power plants. Otherwise, the third is wind energy exploited in a specific and windy region. Thus, Algeria's plan for renewable energy is focused on using solar energy resources to increase electricity production. This is because the area has a lot of potential for solar energy.

PV power is projected to cross more than 37% of national electricity output by 2030. Large-scale photovoltaic power plants normally have significant initial exploration requirements; however, numerous initiatives to upgrade the national utility grid are being carried out in many regions of Algeria [1].

Although Rooftop Solar efforts have been widely successful in other countries, their implementation in Algeria has not yet been able to reach grid parity i.e. the interval at the time when the cost of power generated is less than the cost of electricity received from the grid. Strong capital spending investment is the key challenge. Nevertheless, in the near term, Rooftop solar is projected to be cost-effective, considering the continued decrease in the price of PV modules and the continued depletion of traditional resources [2].

To invest in PV power generation, unused areas like the top of buildings of homes, industries, and big buildings could be used the Rooftop Solar systems easily.

The performance of the entire PV system relies on various key elements: photovoltaic cells, power electronics devices, and the control model such as the algorithm to track the maximum power point (MPPT). Scientists are also constantly working to improve the performance of solar cells. Conventional crystalline silicon solar cells' effectiveness has been attained between 22% and 26% [3]. Regarding cells with a single junction, and after measurements, the best reported is 26.7 for Silicon (Si) crystalline cells. It has been reported that the performance of four-junction wafer-bonded concentrator solar cells may reach 46.1% [4]. In a research prototype using silicon carbide (SiC) transistors, at the power electronic device level, the Fraunhofer Institute for Solar Energy Systems ISE achieved a performance score of 98.7 for solar inverters [5], which will increase the reliability of the PV applications.

2. Goal and significance of the research area

The goal of our study is to suggest, test, and then implement a low-cost current sensorless MPPT algorithm for PV applications under uniform irradiance and partial shading conditions.

The first suggested algorithm is based on a digital control approach with a current sensorless algorithm driven by a low-cost microcontroller, and then the second suggested algorithm is a modified version of the current sensorless approach with a direct control scheme to deal with partial shading conditions. The schemes incorporate a direct control technique to avoid the PI control loop and reduce the computational time, where the searching is based on the *Q-D* characteristics, unlike the hill-climbing approach, which is based on the *P-V* or *P-D* characteristics of the PV curve. The probable results of the proposed methods are effective MPPT tracking under uniform conditions as well as under partial shading conditions.

3. Organization of the thesis

Four chapters make up the body of this thesis. The accomplishments, goals, and scopes of the investigation are described in this chapter. In addition to that, a summary of the most recent MPPT techniques that have been suggested in the literature may be found in this chapter too. Consequently, these MPPT methods are divided into four categories: 1) MPPT based on conventional methods, 2) MPPT based on soft computing, and 3) modified conventional MPPT. And then 4) MPPT-based hybrid methods.

In Chapter 2, the typical DC-DC converters are modelled, and then the performance of the converters for current sensorless MPPT controllers in PV applications is evaluated.

In Chapter 3, we present a current sensorless MPPT control of a buck-boost converter for PV applications. Additionally, we designed the latter using the Stateflow tool, where the proposed approach is examined in a Matlab/Simulink environment. Then, the algorithm was evaluated in a set-up experimental environment that was driven by a low-cost microcontroller, such as the Arduino Due. In Chapter 4, a modified version of the current sensorless MPPT is developed to overcome the shortcomings of conventional methods.

In fact, the algorithm's working principle, the proposed method's design, flowcharts, and the hardware used to carry out the proposed method are all explained in detail. The proposed method's powerful advantage is well highlighted.

Finally, a summary and highlights of the key conclusions from the study are presented. Additional research initiatives are suggested for improving the current sensorless MPPT controller to drive PV applications in the future.

4. References

[1] I. E. A. International Energy Agency, ("https://www.iea.org/policies/95-renewable-energy-and-energy-efficiency-development-plan-2011-2030," 2017) [Online].

[2] M. Shi et al., "Opportunity of rooftop solar photovoltaic as a cost-effective and environment-friendly power source in megacities," vol. 25, no. 9, 2022.

[3] K. Masuko et al., "Achievement of more than 25% conversion efficiency with crystalline silicon heterojunction solar cell," vol. 4, no. 6, pp. 1433-1435, 2014.

[4] F. Dimroth et al., "Four-junction wafer-bonded concentrator solar cells," vol. 6, no. 1, pp. 343-349, 2015.

[5] F. I. f. S. E. S. Fraunhofer-Institut Für Solare Energie Systeme ISE, ("https://www.ise.fraunhofer.de/en/press-media/press-releases/2015/fraunhofer-ise-develops-highly-efficient-compact-inverter-for-uninterruptible-power-supplies.html," 2015) [Online].

CHAPTER I

LITERATURE SURVEY OF THE MPPT TECHNIQUES

I.1 Introduction

In recent years, the world faced many challenges for fossil fuel power plants, including rising costs and concerns about supply. Furthermore, the burning of fossil fuels is the primary cause of the rising quantity of carbon dioxide, which alters the ecological equilibrium by releasing chemical vapors and other potentially hazardous substances into the atmosphere. To prevent a catastrophic event on a global scale and to preserve fossil fuel reserves on Earth, we must immediately adopt renewable technologies that use natural fuels like energy from the sun to generate electricity in a clean and efficient manner [1].

Solar photovoltaic (PV) systems are one of the sustainable and renewable technologies that play an essential role in addressing both present and future electrical problems. This is due to the fact that these technologies utilize solar radiation, which is both a limitless source of energy and a source that is accessible every day. In addition to this, it is able to conserve energy on the batteries over the day so that it can be used again during the night, which not only makes it the most advantageous technology among sustainable and renewable technologies but also makes it competitive with power plants that run on natural fuels [2].

In this chapter, we will highlight the photovoltaic system, which transforms solar energy into electricity directly without the need for any supplementary equipment compared to other renewable systems such as concentrated solar power (CSP) that need to drive conventional generators to produce the electricity [3].

Besides, this chapter provides general descriptions of PV panels and their behavior under environmental uniform conditions as well as under partial shading conditions. In addition to that, this chapter is considered an academic literature review that provides a comparison to the four categories of maximum power point tracking (MPPT) techniques used to harvest the energy from the PV panels i.e. to extract the maximum power produced from the PV panels. This work shows the most MPPT techniques used in academic and industrial photovoltaic applications.

I.2 The solar resource for electricity production from renewable energy systems

Today, photovoltaic solar energy contributes intensively to the world's electricity production due to its regular distribution on the surface of the terrestrial globe. Nevertheless, photovoltaic solar energy systems need solar irradiation, and temperature, and therefore need to harvest the maximum power by using special controllers. PV system requires enough solar irradiation, so it is unsuitable for all geographic regions. Fig. I.1 shows the potential for installing PV and CSP in different regions around the world [4].

In this context, the best places for the implantation of PV, and CSP technology are in the equatorial belt commonly called the solar belt, i.e. in the sunniest area of the planet, for the investment of a large part of radiation. This is where solar power generation is most beneficial. Fig. I.1 indicates that PV and CSP systems are particularly suited to the Mediterranean rim, the Middle East, the American Southwest, and the deserts of Australia. PV power plants must become competitive with conventional thermal power plants in areas with strong sunlight and thus contribute to global climate protection [4].

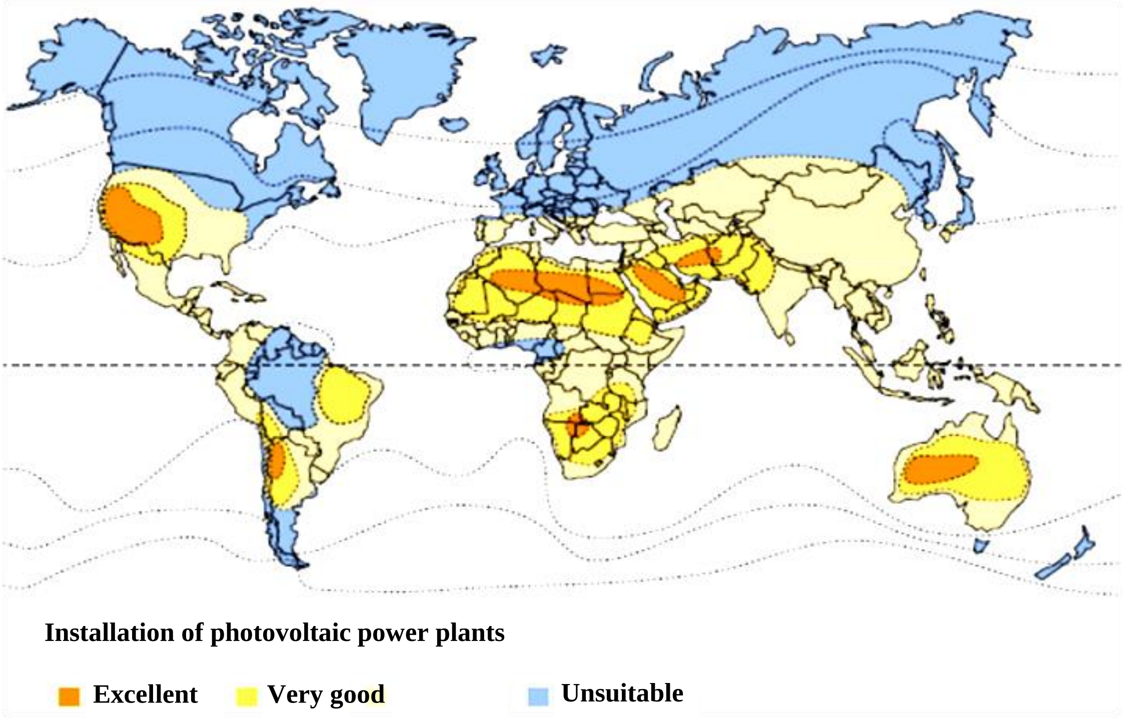

Figure I.1. The solar belt regions of the globe.

Algeria is a country in the solar belt region where a high intensity of solar radiation is received; over 2,000,000 km^2 gets an amount per year of sunlight that is equivalent to 2500 kWh/m^2, and the average yearly amount of sunshine gets 2650 hours. On the coastline to 3500 hrs in the south. This available resource can be used through photovoltaic power plants to face the issue of the rising annual demand for energy [3].

I.3 The photovoltaic system

Photovoltaic systems consist of interconnected photovoltaic modules/arrays. A photovoltaic system may include an MPPT controller, battery backup, and an inverter. The entire system is built to control and generate electricity, which is then connected to the grid. These systems include battery backup, as shown in Fig. I.2. The system uses energy stored in the form of batteries to keep "critical load" circuits running during a power outage. When a power outage occurs [5, 6].

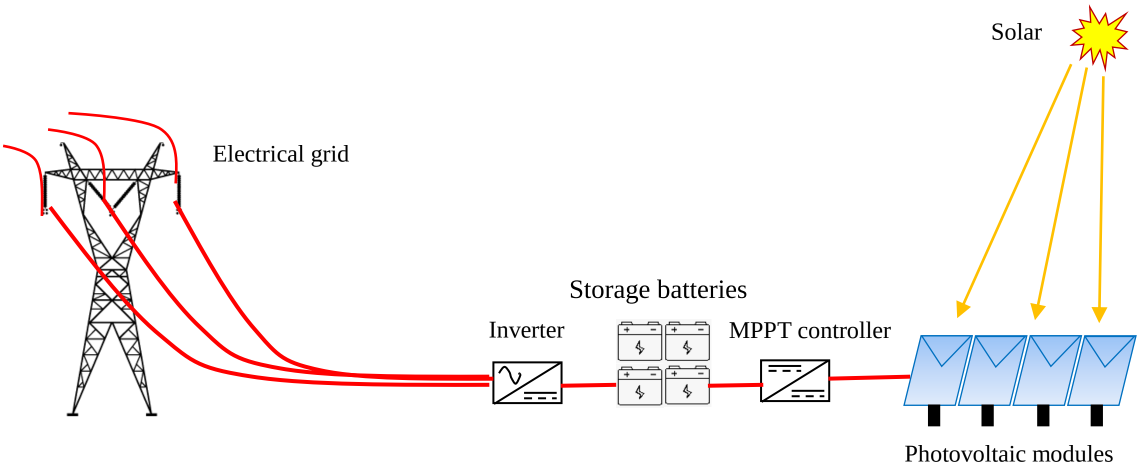

Figure I.2. Schematic diagram of the photovoltaic system.

I.3.1 Principle of operation of the photovoltaic modules

Solar photovoltaic cells are constructed from the key component called semiconductors such as Silicon solar cells, their principle of operation depends on the characteristics of these semiconductors to directly convert solar radiation into electrical energy [7, 8]. They contain no moving parts and can be linked in series and parallel to build photovoltaic modules that can generate electricity with different capacities depending on module area and efficiency.

Solar photovoltaic cells have a working life of more than 25 years. The relatively weak intensity of zenith 1 kW/m^2, daytime variation, and nighttime disappearance is the main drawback. The investment cost of installation, although quickly decreasing below $1/W, is still relatively high. A product of the rapidly evolving electronics industry, solar cells have made an impressive advance in achieving higher efficiencies with low-cost over the past two decades [9].

In particular, the performance of photovoltaic modules is characterized by an *I-V* curve, which is the relationship between the photoelectric output current *I* of the module and the potential difference *V* between the two terminals of the PV module. This is in the condition when the solar irradiance is 1000W/m^2, and the working temperature of the module is 25°C. For further illustration, *I-V* and *P-V* curves are shown in Fig I.3. It can be seen the key elements for assessing the performance of a photovoltaic module on the *I-V* and *P-V* curve are three points: 1) *Isc* short-circuit current, which is the maximum photocurrent generated by the module. 2) *Voc* open-circuit voltage, that is, the maximum voltage at which the module can work. This voltage occurs when the load resistance is infinite, so I = 0. And then 3) MPP maximum power point, which is the maximum power that the PV module can produce. It can be seen from Fig. I.3, the MPP is exist around 0.8V_{oc} where V_{oc} is the open circuit voltage of the PV module. The PV output power is calculated by multiplying each output current by its corresponding load voltage [10]. The output power generated by the PV module is illustrated on the *P-V* characteristics curve as depicted in Fig. I.3.

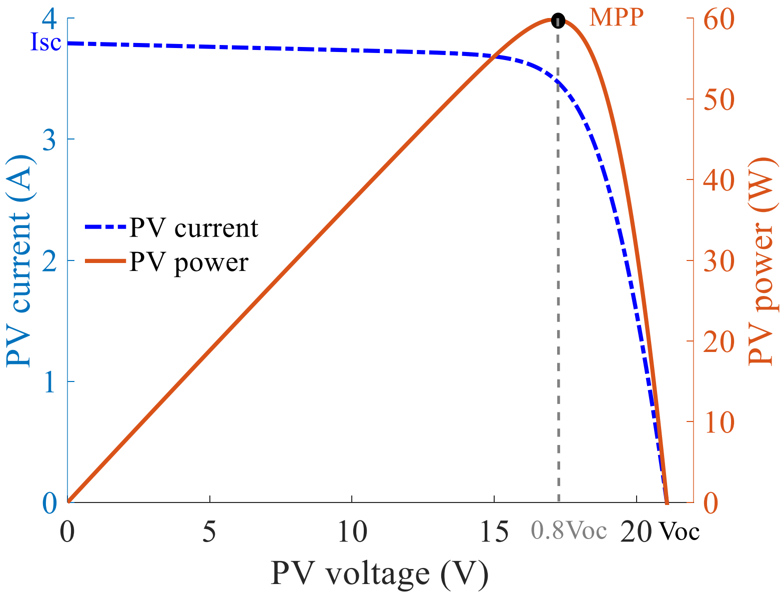

Figure I.3. The electrical *I-V* and *P-V* curve characteristics of the photovoltaic module.

I.3.2 The photovoltaic cell

Studying and modelling the photovoltaic modules to assess their performance according to the simulation environment is still an important part of the research in general. In particular, the field of this study i.e. the renewable energy system. A common modelling of the photovoltaic cell is an equivalent electrical circuit. In the literature, two models are distinguished, namely the single-diode equivalent circuit and the double-diode equivalent circuit [11]. The latter models were established can define *I-V* curves with all cases of solar irradiance *G* and solar temperature *T* values according to the parametric equations, the shape of the *I-V* and *P-V* curves being determined by these parameters, as well as the amplitude.

I.3.2.1 The single-diode equivalent circuit of photovoltaic cell

Fig. I.4 illustrates the circuit diagram of the equivalent one-diode model of the PV cell [12]. The output voltage of the PV cell and the total current of the PV panel (*I*) can be obtained as follows:

$$V = R_{sh} I_{Rsh} - R_s I \tag{I.1}$$

where $I_{Rsh} = I_{ph} - I_D - I$

$$I = I_{ph} - I_{rs}\left(e^{\frac{q(V+IR_s)}{N_S nkT}} - 1\right) - \left(\frac{V+IR_s}{R_{sh}}\right) \tag{I.2}$$

where the diode current (I_D) is introduced as follows:

$$I_D = I_{rs}\left(e^{\frac{q(V+IR_s)}{N_S nkT}} - 1\right) \tag{I.3}$$

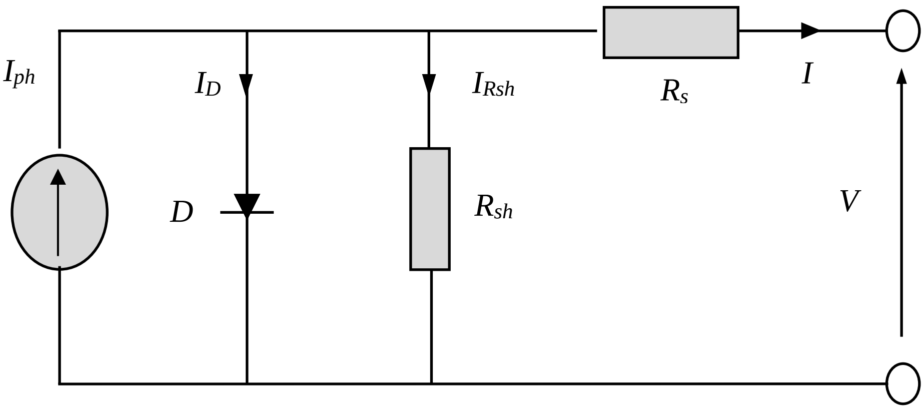

Figure I.4. Equivalent circuit of one diode model of PV cell.

Indeed, the diode has a phenomenon called the saturation current (*Irs*) which is denoted as:

$$I_{rs} = I_{rs\_ref}\left(\frac{T}{T_{ref}}\right)^{3}\left(e^{\frac{qEg}{nk}\left(\frac{1}{T_{ref}}-\frac{1}{T}\right)}\right) \tag{I.4}$$

where the saturation current reference (I_{rs_ref}) is given as:

$$I_{rs\_ref} = \frac{Icc}{\left(e^{\frac{qV_{oc}}{N_S nkT_{ref}}}\right)-1} \tag{I.5}$$

In this context, the open circuit voltage of the PV cell is calculated as:

$$V_{oc} = V_{oc\_ref} + K_V \Delta T \tag{I.6}$$

where ΔT is the difference between the actual temperature (T) and the reference temperature (T_{ref}) i.e. at standard test conditions STC.

On the other hand, the PV current is calculated as:

$$I = \frac{G}{G_{STC}}\left(I_{sc\_ref} + K_I \Delta T\right) \tag{I.7}$$

where I_{ph} is the photocurrent, I_D is given by the Schockley equation, which defines the *I-V* characteristic of an ideal diode, R_{sh} and R_s are the shunt and series resistances, respectively. Furthermore, the given values of the equivalent PV circuit are, the band gap (Eg) is 1.1 [ev], extinction coefficient K is $1.38e^{-23,}$ [j/k], electron charge (q) is $1.6e^{-19}$, and junction ideality factor (n) is 1.3. In total, five unknown parameters in the model are required to be determined, i.e. *I*, *Irs*, *n*, *Rs*, and *Rsh*.

I.3.2.2 The two-diode equivalent circuit of photovoltaic cell

Fig. I.5 illustrates the circuit diagram of the equivalent two-diode model of the PV cell [11]. Where this model was established with extended parameters to be more accurate, but in the environment of simulation, there is no significant difference and both of the models are considered in a wide range of literature research.

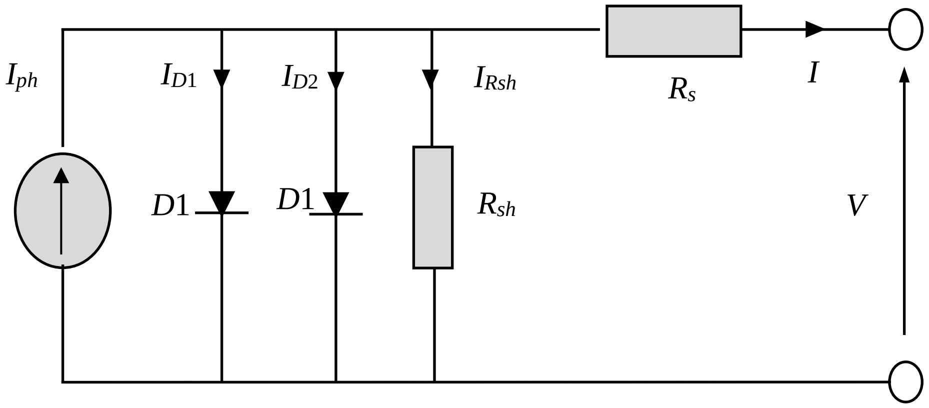

Figure I.5. Equivalent circuit of two-diode model of PV cell.

The voltage of the PV cell and total current generated by the two-diode equivalent circuit of the PV cell as shown in Fig. I.5 is given as follows:

$$V = R_{sh}(I_{ph} - I_{D1} - I_{D2} - I) - R_s I \tag{I.8}$$

$$I = I_{ph} - I_{rs1}\left(e^{\frac{q(V+IR_s)}{n_1 N_S kT}} - 1\right) - I_{rs2}\left(e^{\frac{q(V+IR_s)}{n_2 N_S kT}} - 1\right) - \left(\frac{V+IR_s}{R_{sh}}\right) \tag{I.9}$$

*Irs*1, *n*1 and *Irs*2, *n*2 identify the saturation current as well as the ideality factor of the first diode and the second diode, respectively. There are a total of seven parameters, or variables, that need to be identified in this model. i.e. *I*, *Irs*1, *Irs*2, *n*1, *n*2, R_s, and R_{sh}.

I.3.3 The photovoltaic module behavior under uniform environmental conditions

For the dynamic behavior analysis of the PV panel, its characteristics are listed in Table I.1.

I.3.3.1 Under irradiance changes

As can be seen in Fig. I.6 and 17, respectively in the case study when changing the environmental condition that a PV module is subjected to, e.g. when the solar irradiance decrease occurs with the fixed temperature at 25° C, the maximum power values i.e. (*P*-*V*) curves are decreased and their current-voltage (*I-V*) curves for the PV current are decreased too. It can be concluded, that the MPP region exists at approximately to 0.8*Voc* for all *P-V* curves.

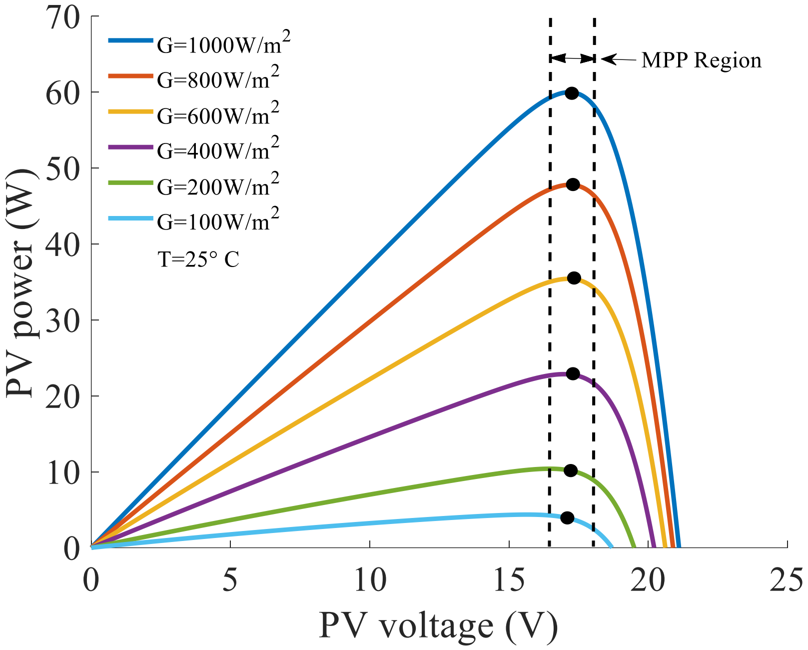

Figure I.6. Electrical *P-V* characteristics of the PV module under variation of the irradiance with fixed temperature at 25° C.

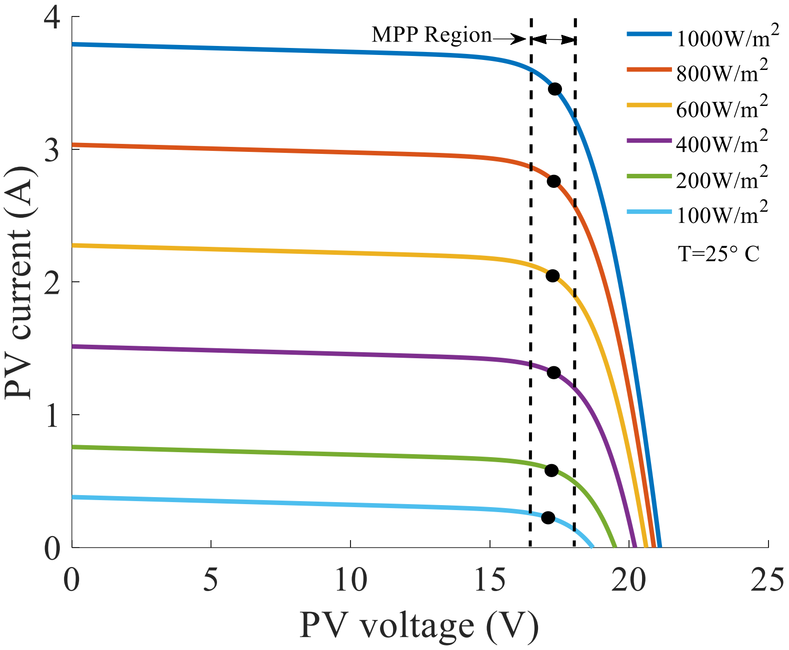

Figure I.7. Electrical *I-V* characteristics of the PV module under variation of the irradiance with the fixed temperature at 25° C.

I.3.3.2 Under temperature changes

On the other hand, as can be seen in Fig. I.8 and I.9, respectively when the temperature decrease occurs with fixed solar irradiance at 1000 W/m^2, the maximum power values increased and the voltage values are increased too, contrary to the previous case. Here, it can be concluded, the MPP region exists at around to 0.8V_{oc} for all *P*-*V* curves but is a bit big.

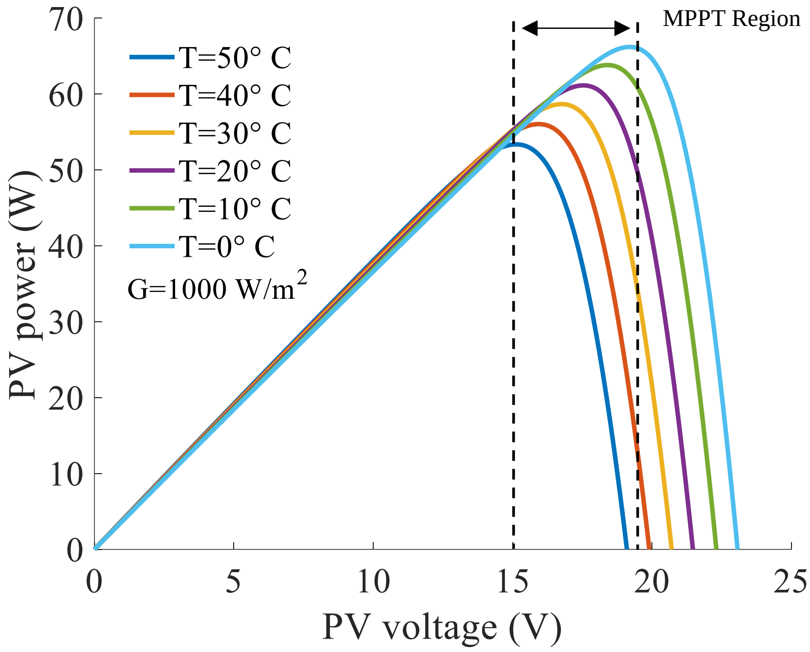

Figure I.8. Electrical *P*-*V* characteristics of the PV module under variation of the temperature with fixed irradiance at 1000 W/m^2.

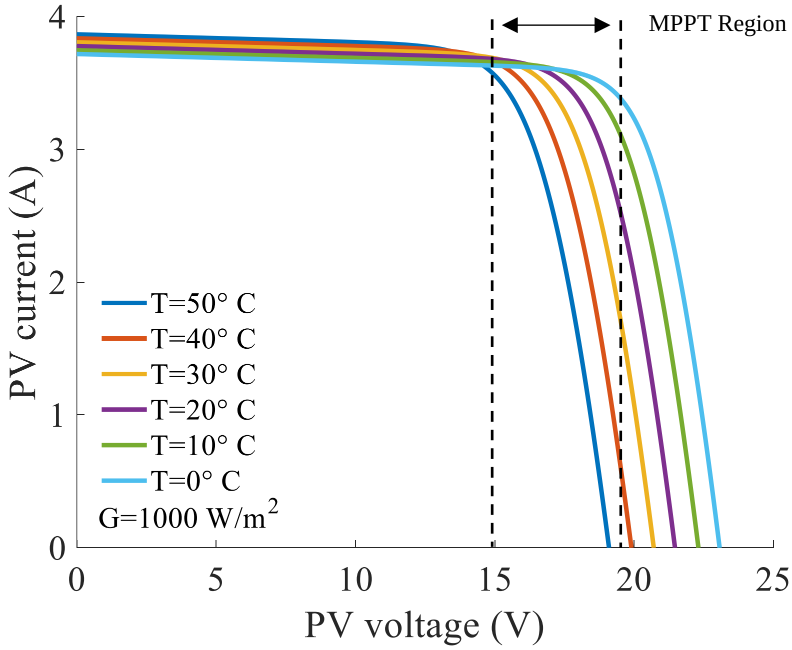

Figure I.9. Electrical *I*-*V* characteristics of the PV module under variation of the temperature with fixed irradiance at 1000 W/m^2.

Table I.1. Characteristics of MSX60 Panel at Standard Test Conditions (STC).

Parameters	**Labels**	**Values**
Max Power	P_{max}	60 W
Max Voltage	V_{max}	17.1 V
Max current	I_{max}	3.5 A
Short-Circuit	I_{sc}	3.8 A
Open Circuit voltage	V_{oc}	21.1 V
Temperature coefficient of *ISC*	K_V	0.003 %/^{o} C
Temperature coefficient of *VOC*	K_I	-0.08 %/^{o} C
Number of cells	N_S	36

I.3.4 The photovoltaic modules' behavior under partial shading conditions

Photovoltaic applications are usually constructed by a number of PV modules such as solar rooftop PV systems or water pumping. In such applications, the PV array might be subjected to partial shading conditions when the environment is not regular and the weather is cloudy where the part of the string/array i.e. PV modules will be subjected to a wide range of different levels of solar irradiation [13]. In addition, the electrical *P-V* characteristics curves for each pattern will have multiple peaks, as depicted in Fig I.10.

It can be observed, for assessing the performance of a photovoltaic string on the *P-V* curve there are important points namely Local MPP (LMPP) and Global MPP (GMPP), as shown in Fig. I.10 the *P-V* characteristics of a PV array under twenty patterns. For these patterns, it can be seen that the local MPP (LMPP) region is confined within the [$D_{\mathrm{k},min}$, $D_{\mathrm{k},max}$] interval, where D_{min} and D_{max} are, respectively, the lower and upper duty cycle (D) limits at every region k. These multiple peaks of power occur when the string/array operates under different solar irradiance values [14]. Thus, the multiple peaks of PV power exist approximately on $k0.8V_{oc}$ where V_{oc} is the open circuit voltage of the PV module, and k is 1, 2, 3, and 4 for this illustrative example, where the patterns continue left, middle and right side of a PV string.

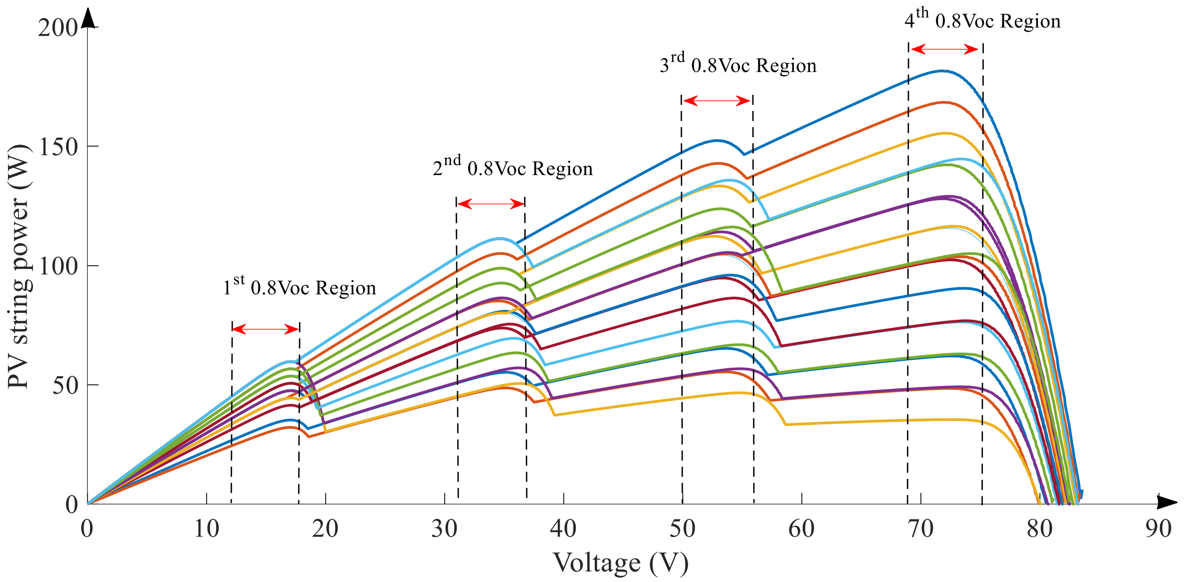

Figure I.10. Twenty *P-V* patterns contain left, middle and right side of a PV string composed of four modules, where the MPP of each region (i.e., 1st, 2nd, 3rd, and 4th) is confined within the k×0.8V_{oc_mod} region.

As can be seen in Table I.2, The 20 scenarios i.e. patterns of the PSCs that were subjected to the four modules of the PV string that depicted in Fig I.10. As Obvious, the *P-V* patterns contain left, middle and right side, where the MPP of each region (i.e., 1st, 2nd, 3rd, and 4th) is confined within the k×0.8V_{oc_mod} region.

Table I.2 The 20 Scenarios i.e. Patterns of the PSCs that were Subjected to the PV String Composed of Four Modules.

Pattern	***G (W/m^2) subjected to PV module 1***	***G (W/m^2) subjected to PV module 2***	***G (W/m^2) subjected to PV module 3***	***G (W/m^2) subjected to PV module 4***
1	**1000**	**900**	**800**	**700**
2	**590**	**850**	**750**	**650**
3	**900**	**800**	**700**	**600**
4	**850**	**750**	**650**	**550**
5	**800**	**700**	**600**	**500**
6	**750**	**650**	**550**	**450**
7	**700**	**600**	**500**	**400**
8	**600**	**450**	**350**	**250**
9	**550**	**400**	**300**	**200**
10	**150**	**250**	**400**	**1000**
11	**200**	**300**	**450**	**1000**
12	**250**	**350**	**500**	**950**
13	**300**	**400**	**550**	**900**
14	**300**	**450**	**600**	**850**
15	**350**	**500**	**650**	**800**
16	**400**	**550**	**700**	**750**
17	**450**	**650**	**750**	**600**
18	**550**	**700**	**800**	**500**
19	**600**	**800**	**900**	**400**
20	**700**	**900**	**1000**	**550**

I.4 Literature review of the MPPT techniques

In literature, the PV system provides DC voltage however, the main challenge of it is that the electrical behaviors are non-linear in nature and change with environmental effects, such as sunlight irradiance and temperature. Thus, the PV system requires specific methods to extract the maximum power point (MPP) from the PV source. This work highlights the main categories of the MPP tracking (MPPT) methods. Several MPPT methods have been established to enhance the efficiency of photovoltaic systems. There was in fact, broad agreement that it is necessary to identify the global maximum power point (GMPP) when multiple peaks characterize the power-voltage (*P-V*) curve under partial shading conditions (PSCs) [15].

Indeed, different MPPT techniques capable of extracting the MPP from PV sources have been presented in literature. These techniques can be basically divided into the following:

Category one: Conventional MPPT techniques: The approach of the conventional techniques is based on the perturbation of the duty cycle according to climbing from one point to another point until reaches the desired power. At this moment, the algorithm will decide to return back one step and then check, and then increase or decrease the duty cycle around three points called three-level duty cycle perturbation as shown in Fig. I.3. Thus, this guarantees that this is the region of the MPP. Among them, hill climbing (HC) [16], constant voltage (CV) [17], perturb and observe (P&O) [18], and incremental conductance (INC) [19] techniques. They effectively track MPP under uniform irradiance levels of all PV modules, and are, nonetheless, projected to lean towards failure under PSCs due to the presence of multiple-peak power phenomena in the power-voltage (*P-V*) or power-duty-cycle (*P-D*) characteristics curves. In particular, the most commonly used conventional MPPT technique is P&O, Fig. I.11, and Fig. I.12 describe the principle operation of P&O and their flowchart, respectively.

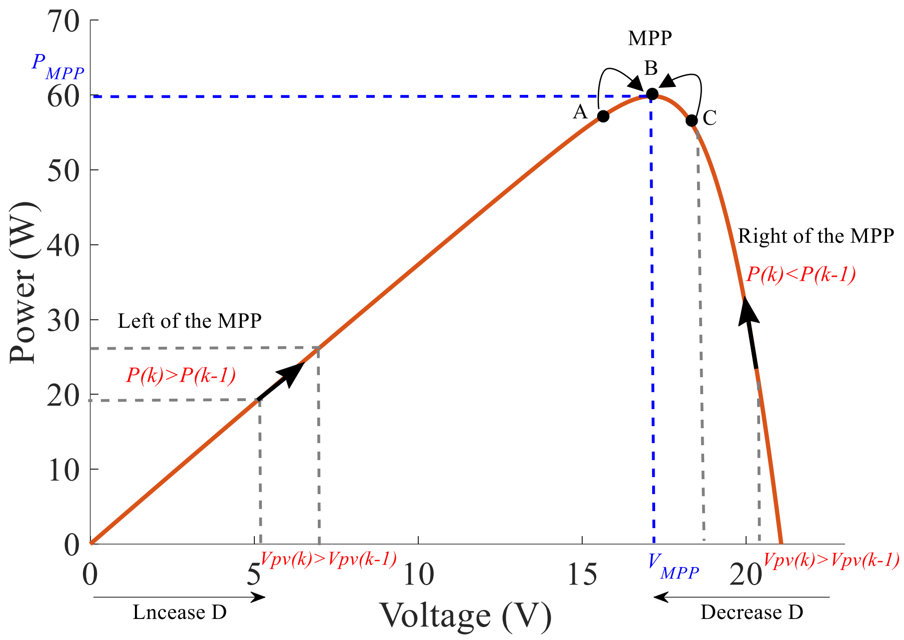

Figure I.11. Principal operation of the P&O algorithm of the electrical *P*-*V* characteristics curve.

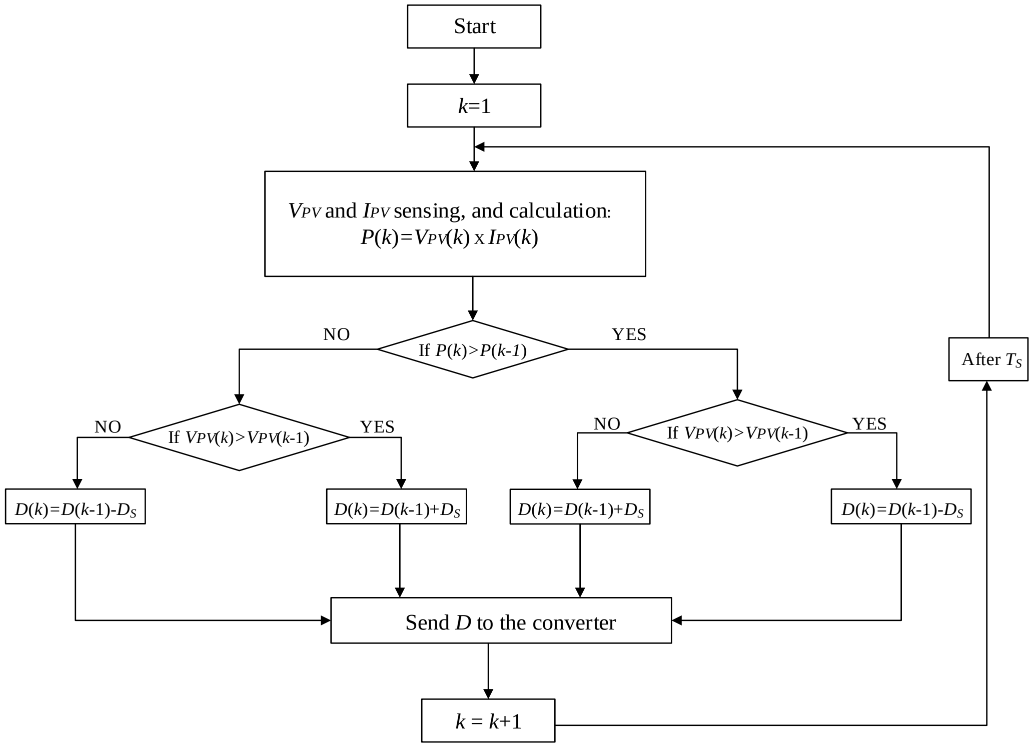

Figure I.12. Flowchart of the P&O-MPPT algorithm [18].

Category two: Soft computing-based MPPT techniques: significantly, over the last few years, several researchers have drawn attention to the above-mentioned issues and sought to improve the performance of MPPT controllers under PSCs. Since furthermore, these techniques had been established based on the number of soft computing metaheuristic algorithms; such as differential evolution-based MPPT (DE) [20], flower pollination algorithm (FPA) [21], partial swarm optimization (PSO) [22], and dynamic leader based collective intelligence (DLCI) [23]. Additionally, artificial intelligence-based MPPT techniques have also been proposed in order to overcome the effect of PSCs, such as artificial neuron networks (ANN) [24], deep learning (DL) [25], and fuzzy logic control (FLC) [26]. Soft computing techniques are able to handle partial shading conditions. In addition to that, the commonly used soft computing for the MPPT is the PSO technique, Fig. I.13. and Fig. I.14 describe the principle of operation of PSO and their flowchart, respectively.

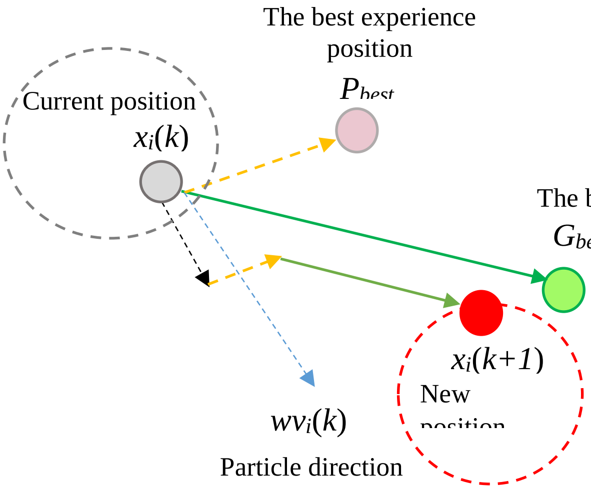

Figure I.13. Principal operation of the PSO technique with movement of the agent in the search area.

Particle swarm optimization (PSO) is a stochastic, population-based EA search approach, established based on the behavior of bird flocks [22]. A PSO technique maintains a swarm of particles, all of which stand for a potential solution. Particles follow a straightforward behavior pattern in which they emulate the accomplishments and successes of both nearby particles and themselves. Consequently, the best particle in the vicinity affects a particle's placement. P_{best}, in addition to the perfect solution discovered by the particle itself, G_{best}. Particle position, x_i, has been adapted by:

$$x_i^{k+1} = x_i^k + v_i^{k+1} \tag{I.10}$$

in which the velocity, vi, denotes the step-size. The velocity is given by:

$$v_i^{k+1} = wv_i^k + c_1r_1(P_{besti} - x_i^k) + c_2r_2(G_{besti} - x_i^k) \tag{I.11}$$

while the weight of inertia (w), c_1 and c_2 are the acceleration coefficients, r_1 , r_2 ϵU(0,1) , $P_{best\ i}$ is the personal best position of particle i, and G_{best} is the best position of the particles. It should be taken into account that r_1 and r_2 are random numbers.

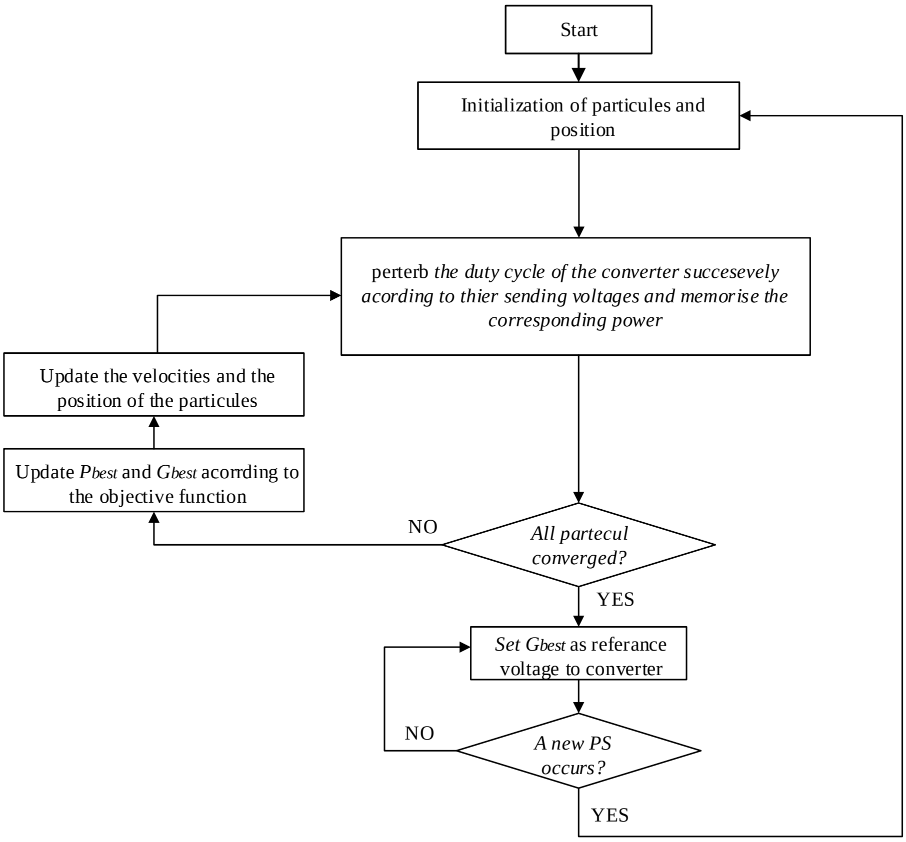

Figure I.14. Flowchart of the PSO-based MPPT method [22].

Category three: Hybrid MPPT techniques: The high computational burden is the main drawback of soft computing techniques [15]. Thus, hybrid approaches have been recently introduced to enhance MPPT performance and efficiency by integrating two or more MPPT techniques [27]. Consequently, experimental results show that hybrid methods can effectively track the GMPP under various PSCs. Nonetheless, all the aforementioned techniques that depend on soft computing benefit from the advantages of powerful processors to track GMPP accurately. Thus, making them costly for low-cost PV applications. In addition to that, the commonly used hybrid MPPT is P&O with PSO technique, Fig. I.15 describes the principle of operation of P&O with PSO and their flowchart, respectively.

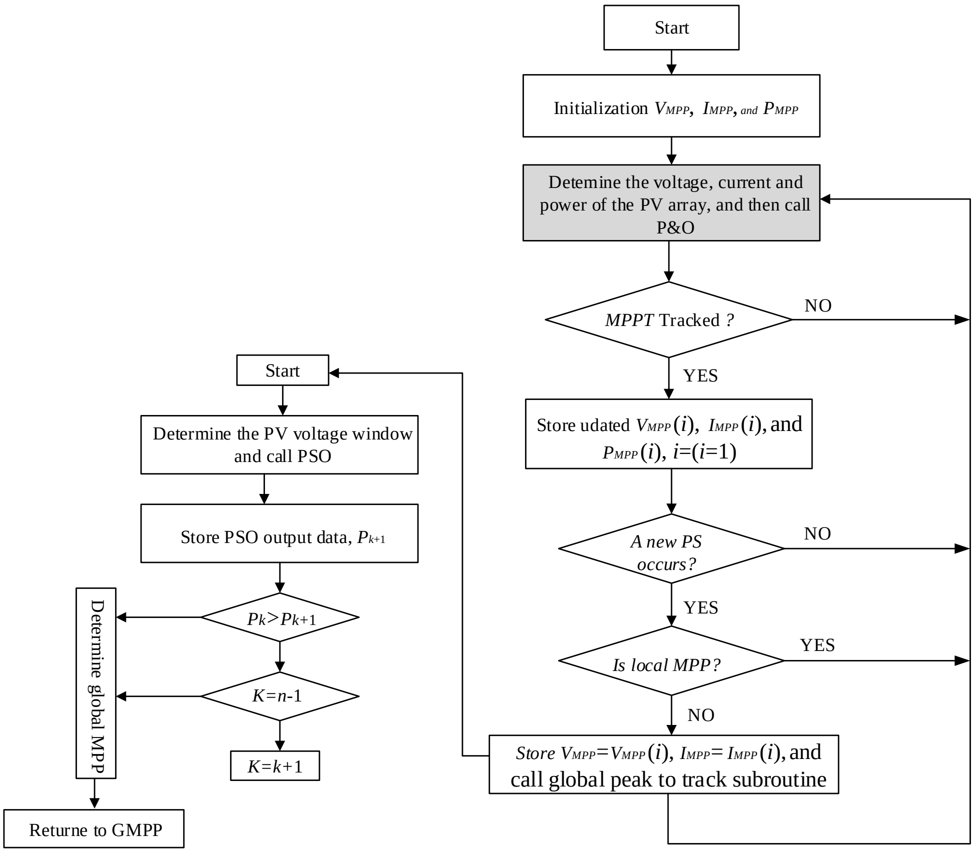

Figure I.15. Flowchart of the hybrid P&O with PSO-based MPPT method [27].

Category four: Modified conventional MPPT techniques: Modified conventional MPPT techniques are less complex and efficient in GMPP tracking. Some typical examples of this are proposed in [10, 14], where authors introduced novel MPPT approaches based on the 0.8×V_{oc_mod} model (V_{oc_mod} is the open-circuit voltage of a PV module) by exploiting the ability of 0.8×V_{oc_mod} model to assume that the peaks of a PV string are located nearly at the multiples of 0.8×V_{oc_mod}. In addition to that, the most commonly used of the MPPT techniques is a modified 0.8Voc MPPT technique, Fig. I.16 describe the principle of operation of modified 0.8Voc and their flowchart, respectively.

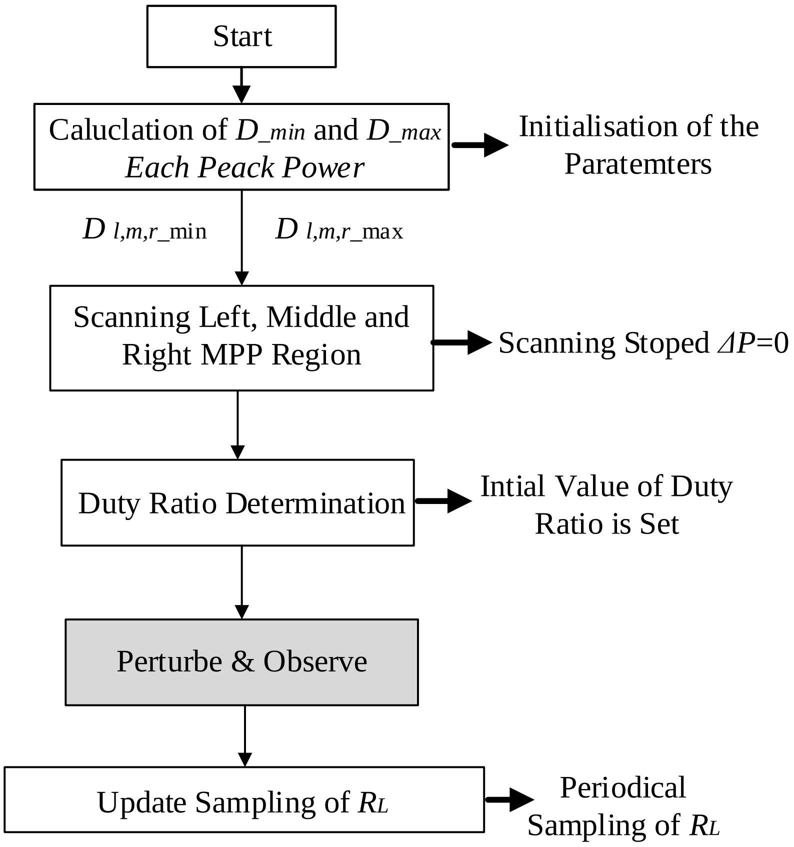

Figure I.16. Flowchart of the modified $0.8V_{oc}$ MPPT method [10].

Table I.3 summarizes the relevant MPPT techniques that have been studied in the literature.

Table I.3 Literature Survey of the Most MPPT Techniques.

Category		MPPT algorithm	DC-DC Converter used	Sensor used		Computational burden	Steady-state oscillation level	Tracking ability under PSC test	Sensor cost
				Current	Voltage				
Conventional MPPT methods	Two ADC channels	HI [16]	Boost	Yes	Yes	Low	Very High	No	High
		P&O [18]	Boost	Yes	Yes	Low	High	No	High
		INC [19]	Boost	Yes	Yes	Low	High	No	High
	One ADC channel	Single sensor-based MPPT [28]	Boost	No	Yes	Medium	High	No	Low
		SIV-based MPPT [29]	SEPIC	No	Yes	Medium	High	No	Low
Modified MPPT algorithms	Two ADC channels	Modified INC [13]	SEPIC	Yes	Yes	Medium	Medium	Yes	High
		ST [30]	Boost	Yes	Yes	Medium	Medium	Yes	High
		Improved 0.8V_{OC} [10]	SEPIC	Yes	Yes	Medium	Medium	Yes	High
	One ADC channel	Modified MPT with modified SSJ [33]	Boost	Yes	No	Medium	Low	Yes	Low
Soft computing metaheuristic algorithms	Two ADC channels	FPA [21]	Boost	Yes	Yes	High	Low	Yes	High
		DL [32]	high step up	Yes	Yes	High	Low	Yes	High
		MSSA [31]	Boost	Yes	Yes	High	Low	Yes	High
		DLCI [23]	Boost	Yes	Yes	High	Low	Yes	High
	One ADC channel	HPO [32]	Boot	Yes	Estimated	High	Low	Yes	Low
Hybrid methods	Two ADC channels	PSO-P&O [27]	Buck-boost	Yes	Yes	High	Low	Yes	High
		GA-PSO [34]	Boost	Yes	Yes	High	Low	Yes	High

I.5. Conclusion

In the next chapters, we will study new MPPT techniques based on the proposal of new MPPT algorithms with reduce the number of sensors used in MPPT techniques. This study will contribute significantly to the evaluation of the performance of the current sensorless MPPT techniques proposed in this thesis.

In conclusion, what we have presented in this chapter, PV technology is the most popular technology on the technical and commercial levels. As a stand-alone system or hybrid system, this technology could provide the needed electricity at a low cost and with few economic risks. Therefore, PV technologies with promising low carbon emissions will play an important role in future global energy supplies.

This chapter presented an overview of solar photovoltaic systems in power plants. Each PV system depends on the type of MPPT technique used, and the topology of the converter structure. It should be noted that since the investment cost of these technologies is still very high, these are not yet accessible to most countries in the world. It is therefore imperative today to think about new technologies that could considerably reduce the cost of investment and thus allow an appropriation of this type of technology in all countries around the world.

The advantage of certain compelling potential made available by PV technology offers an opportunity for Algeria country. Algeria not only has one of the largest gas reserves in the world, but it also has huge renewable energy resources, including solar energy. Algeria sees ideal opportunities to combine Algerian natural gas with solar PV systems. Therefore, this is among the adopted solutions that will reduce investment costs.

I.6 References

[1] H. Ghasemi-Mobtaker, F. Mostashari-Rad, Z. Saber, K.-w. Chau, and A. Nabavi-Pelesaraei, "Application of photovoltaic system to modify energy use, environmental damages and cumulative exergy demand of two irrigation systems-A case study: Barley production of Iran," *Renewable Energy,* vol. 160, pp. 1316-1334, 2020.

[2] F. Hosseini-Fashami, A. Motevali, A. Nabavi-Pelesaraei, S. J. Hashemi, and K.-w. Chau, "Energy-Life cycle assessment on applying solar technologies for greenhouse strawberry production," *Renewable and Sustainable Energy Reviews,* vol. 116, p. 109411, 2019.

[3] L. Achour, M. Bouharkat, O. Assas, and O. Behar, "Hybrid model for estimating monthly global solar radiation for the Southern of Algeria:(Case study: Tamanrasset, Algeria)," *Energy,* vol. 135, pp. 526-539, 2017.

[4] D. N. B. J. N. Roy, "Photovoltaic Science and Technology," *Cambridge University Press,* 2017.

[5] J. N. Roy and D. N. Bose, *Photovoltaic Science and Technology*: Cambridge University Press, 2018.

[6] I. Laib, A. Hamidat, M. Haddadi, N. Ramzan, and A. G. Olabi, "Study and simulation of the energy performances of a grid-connected PV system supplying a residential house in north of Algeria," *Energy,* vol. 152, pp. 445-454, 2018.

[7] S. Abdelhady, M. S. Abd-Elhady, and M. M. Fouad, "An understanding of the operation of silicon photovoltaic panels," *Energy Procedia,* vol. 113, pp. 466-475, 2017.

[8] A. Ndiaye, A. Charki, A. Kobi, C. M. Kébé, P. A. Ndiaye, and V. Sambou, "Degradations of silicon photovoltaic modules: A literature review," *Solar Energy,* vol. 96, pp. 140-151, 2013.

[9] E. Ndzibah, G. Andrea Pinilla-De La Cruz, and A. Shamsuzzoha, "End of life analysis of solar photovoltaic panel: roadmap for developing economies," *International Journal of Energy Sector Management,* vol. 16, pp. 112-128, 2022.

[10] M. E. Başoğlu, "An improved 0.8 V OC model based GMPPT technique for module level photovoltaic power optimizers," *IEEE Transactions on Industry Applications,* vol. 55, pp. 1913-1921, 2018.

[11] M. Kermadi, S. Mekhilef, Z. Salam, J. Ahmed, and E. M. Berkouk, "Assessment of maximum power point trackers performance using direct and indirect control methods," *International Transactions on Electrical Energy Systems,* vol. 30, p. e12565, 2020.

[12] A. Loukriz, M. Haddadi, and S. Messalti, "Simulation and experimental design of a new advanced variable step size Incremental Conductance MPPT algorithm for PV systems," *ISA transactions,* vol. 62, pp. 30-38, 2016.

[13] K. S. Tey and S. Mekhilef, "Modified incremental conductance algorithm for photovoltaic system under partial shading conditions and load variation," *IEEE Transactions on Industrial Electronics,* vol. 61, pp. 5384-5392, 2014.

[14] Z. Bi, J. Ma, K. L. Man, J. S. Smith, Y. Yue, and H. Wen, "An Enhanced 0.8$\text {V} _\text {OC} $-Model-Based Global Maximum Power Point Tracking Method for Photovoltaic Systems," *IEEE Transactions on Industry Applications,* vol. 56, pp. 6825-6834, 2020.

[15] J. S. Goud, R. Kalpana, and B. Singh, "A hybrid global maximum power point tracking technique with fast convergence speed for partial-shaded PV systems," *IEEE Transactions on Industry Applications,* vol. 54, pp. 5367-5376, 2018.

[16] M. Lasheen and M. Abdel-Salam, "Maximum power point tracking using Hill Climbing and ANFIS techniques for PV applications: A review and a novel hybrid approach," *Energy conversion and management,* vol. 171, pp. 1002-1019, 2018.

[17] N. Karami, N. Moubayed, and R. Outbib, "General review and classification of different MPPT Techniques," *Renewable and Sustainable Energy Reviews,* vol. 68, pp. 1-18, 2017.

[18] R. Boukenoui, M. Ghanes, J.-P. Barbot, R. Bradai, A. Mellit, and H. Salhi, "Experimental assessment of Maximum Power Point Tracking methods for photovoltaic systems," *Energy,* vol. 132, pp. 324-340, 2017.

[19] V. Jately and S. Arora, "Development of a dual-tracking technique for extracting maximum power from PV systems under rapidly changing environmental conditions," *Energy,* vol. 133, pp. 557-571, 2017.

[20] K. S. Tey, S. Mekhilef, H.-T. Yang, and M.-K. Chuang, "A differential evolution based MPPT method for photovoltaic modules under partial shading conditions," *International Journal of Photoenergy,* vol. 2014, 2014.

[21] J. P. Ram and N. Rajasekar, "A novel flower pollination based global maximum power point method for solar maximum power point tracking," *IEEE Transactions on Power Electronics,* vol. 32, pp. 8486-8499, 2016.

[22] K. Ishaque, Z. Salam, M. Amjad, and S. Mekhilef, "An improved particle swarm optimization (PSO)–based MPPT for PV with reduced steady-state oscillation," *IEEE transactions on Power Electronics,* vol. 27, pp. 3627-3638, 2012.

[23] B. Yang, T. Yu, X. Zhang, H. Li, H. Shu, Y. Sang, *et al.*, "Dynamic leader based collective intelligence for maximum power point tracking of PV systems affected by partial shading condition," *Energy Conversion and Management,* vol. 179, pp. 286-303, 2019.

[24] M. Kermadi and E. M. Berkouk, "Artificial intelligence-based maximum power point tracking controllers for Photovoltaic systems: Comparative study," *Renewable and Sustainable Energy Reviews,* vol. 69, pp. 369-386, 2017.

[25] Y. Du, K. Yan, Z. Ren, and W. Xiao, "Designing localized MPPT for PV systems using fuzzy-weighted extreme learning machine," *Energies*, vol. 11, p. 2615, 2018.

[26] D. Bawa and C. Patil, "Fuzzy control based solar tracker using Arduino Uno," *International Journal of Engineering and Innovative Technology,* vol. 2, pp. 179-187, 2013.

[27] M. Kermadi, Z. Salam, J. Ahmed, and E. M. Berkouk, "An effective hybrid maximum power point tracker of photovoltaic arrays for complex partial shading conditions," *IEEE Transactions on Industrial Electronics,* vol. 66, pp. 6990-7000, 2018.

[28] N. Dasgupta, A. Pandey, and A. K. Mukerjee, "Voltage-sensing-based photovoltaic MPPT with improved tracking and drift avoidance capabilities," Solar energy materials and solar cells, vol. 92, pp. 1552-1558, 2008.

[29] M. Killi and S. Samanta, "Voltage-sensor-based MPPT for stand-alone PV systems through voltage reference control," *IEEE Journal of Emerging and Selected Topics in Power Electronics,* vol. 7, pp. 1399-1407, 2018.

[30] S. Hosseini, S. Taheri, M. Farzaneh, and H. Taheri, "A high-performance shade-tolerant MPPT based on current-mode control," *IEEE Transactions on Power Electronics,* vol. 34, pp. 10327-10340, 2019.

[31] B. Yang, L. Zhong, X. Zhang, H. Shu, T. Yu, H. Li, *et al.*, "Novel bio-inspired memetic salp swarm algorithm and application to MPPT for PV systems considering partial shading condition," *Journal of cleaner production,* vol. 215, pp. 1203-1222, 2019.

[32] Y. Du, K. Yan, Z. Ren, and W. Xiao, "Designing localized MPPT for PV systems using fuzzy-weighted extreme learning machine," *Energies,* vol. 11, p. 2615, 2018.

[32] N. Kumar, I. Hussain, B. Singh, and B. K. Panigrahi, "Single sensor based MPPT for partially shaded solar photovoltaic by using human psychology optimisation algorithm," *IET Generation, Transmission & Distribution,* vol. 11, pp. 2562-2574, 2017.

[33] G. Zhou, Q. Bi, Q. Tian, M. Leng, and G. Xu, "Single Sensor Based Global Maximum Power Point Tracking Algorithm of PV System With Partial Shading Condition," *IEEE Transactions on Industrial Electronics,* vol. 69, pp. 2669-2683, 2021.

[34] C.-C. Hua and Y.-J. Zhan, "A hybrid maximum power point tracking method without oscillations in steady-state for photovoltaic energy systems," *Energies,* vol. 14, p. 5590, 2021.

CHAPTER II

ASSESSMENT OF DC-DC CONVERTERS PERFORMANCE FOR CSL-BASED MPPT METHOD FOR PV APPLICATIONS

II.1 Introduction

In the research that has been done, many circuits that function as DC-DC converters have been investigated with the objective of either adjusting the amplitude of the DC voltage or reversing its polarity. An in-depth analysis of the most popular DC-DC converter circuits and their conversion ratios is presented in this chapter. Additionally, the mathematical modelling of each DC-DC converter is investigated and analyzed as part of this study. Each topology has its unique way of implementing the switches, although they all need a power transistor and a diode. Other types of semiconductor switches, such as IGBTs and MOSFETs, have the ability to replace the transistor [1, 2].

The current sensorless approach based-MPPT is a reasonable choice to increase the system's reliability and reduce power losses, and implementation costs. Their design is performed using a specified objective function (*Q*) generated from their DC-DC converter's mathematical model and does not involve the use of any current sensor. Unlike the first category group, in which operation paths are displayed in the *P-V* or *P-D* curves, the *Q-D* curves of these techniques show the actual paths taken during operation. Although load disturbance and irradiance change are major factors, the DC-DC converter's working area in the *Q-D* plane for the objective function mathematical model is still crucial [3]. These objective functions are determined by the DC-DC converter mathematical models according to their schemes. Consequently, this work focused on studying the performance assessment of three current sensorless MPPT schemes based on their objective functions of DC-DC converters models to highlight their MPP operating region under uniform conditions and then compared between each other topologies, where the schemes are PV-buck, PV-boost, and PV-buck-boost converter, respectively.

II.2 Typical DC-DC converters for the PV applications

II.2.1 The buck converter

In Fig II.1, the conceptual model of the DC-DC buck converter is seen, which is constructed for reducing the input voltage V_{IN} to the less voltage in output V_{OUT}. The components of this converter are the switch *S*, the diode *D* that prevents *S*, the inductor *L*, and the capacitor *C* to maintain relatively stable output. During the operating time of $T \epsilon [0, DTs]$, the state of switch *S* is close, the current flows toward the load begin to increase, and the inductor will generate an opposing polarity between its terminals, in this moment a voltage drop responds the input voltage and consequently decreases the output voltage through the load. During the time of $T \epsilon [DTs, Ts]$, the state of switch *S* is open, the inductor *L* discharges the energy stored in the magnetic form to the load, while the current is still changing, then there will always be a voltage drop through the inductor, so the output voltage will be less than the input voltage source [4].

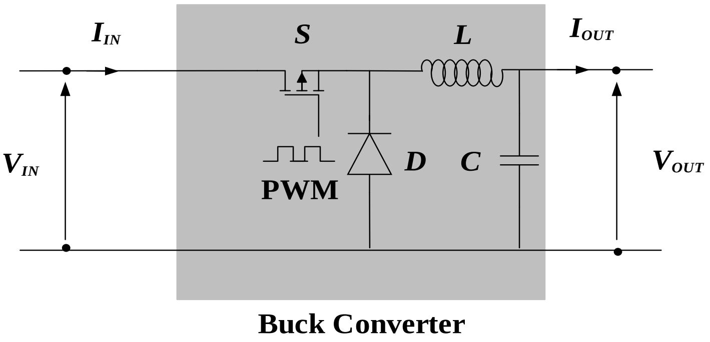

Figure II.1. Electrical circuit of the buck converter.

II.2.1.1 Principle of operation of the buck converter:

Depending on the position of switch *S*, the buck converter's functionality can be separated into two stages:

- When switch *S* is in the ON position, the voltage that is passing through the inductor to the load makes *L* absorbs energy and reduces the voltage at the output.
- For the switch *S* in the OFF position, the current that is flowing through the inductor will begin to decrease and as that happens the magnetic field will begin to collapse, thus it's

going to induce a voltage with opposite polarity. The load will see current from the inductor, and as a result, step up the current and step down the voltage.

II.2.1.2 Buck converter circuit modelling and the state-space representation:

The buck converter's mathematical modelling starts with the converter's key elements such as the inductor and capacitor. An equation for the buck converter's capacitor current is provided in [5] as follows:

$$i_C(t) = C\frac{dv_C(t)}{dt} \tag{II.1}$$

In such case, the equation for the voltage of the inductor is presented as follows:

$$v_L(t) = L\frac{di_L(t)}{dt} \tag{II.2}$$

The following two equations, which together make up the state representation, may be used to explain the development of the system as a function of time.

$$\begin{cases} \overset{\bullet}{X} = f(x,u,t);\ \text{state equation} \\ Y = g(x,u,t);\ \text{output equation} \end{cases} \tag{II.3}$$

The state representation looks like this if the system under consideration is linear:

$$\begin{cases} \overset{\bullet}{X} = Ax + Bu \\ Y = CX \end{cases} \tag{II.4}$$

The following representation of the state matrix *X* is given for the buck converter case:

$$X = \begin{bmatrix} i_L \\ v_{OUT} \end{bmatrix} \tag{II.5}$$

where *X* is a representation of the state variable, *Y* is a representation of the output vector, *u* is a representation of the command vector or input, and *A* is a converter's state space matrix.

When the buck converter is working in the ON (switching) mode, as shown in Fig. II.2, the continuous conduction mode is assumed, and the corresponding equations for the state space are given as follows:

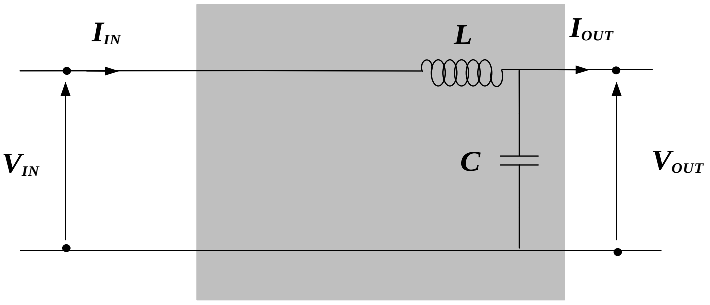

Buck Converter when Switch ON

Figure II.2. Electrical circuit of the buck converter for ON switching mode.

$$\begin{cases} \dfrac{di_L}{dt} = \dfrac{1}{L}(v_{IN} - v_{OUT}) \\ \dfrac{dIv_{OUT}}{dt} = \dfrac{1}{C}(i_L - \dfrac{v_{OUT}}{R}) \end{cases} \tag{II.6}$$

The state matrix *X* and the output result *Y* are calculated as follows, using Eq. (II.8) as the basis:

$$\overset{\bullet}{X} = \begin{bmatrix} \dfrac{di_L}{dt} \\ \dfrac{dv_{OUT}}{dt} \end{bmatrix} = \begin{bmatrix} 0 & -\dfrac{1}{L} \\ \dfrac{1}{C} & -\dfrac{1}{RC} \end{bmatrix} \times \begin{bmatrix} i_L \\ v_{OUT} \end{bmatrix} + \begin{bmatrix} \dfrac{1}{L} \\ 0 \end{bmatrix} \times \left[v_{IN} \right] \tag{II.7}$$

In contrast, the buck converter's state space equations may be derived as follows when the switching mode is OFF, as shown in Fig. II.3:

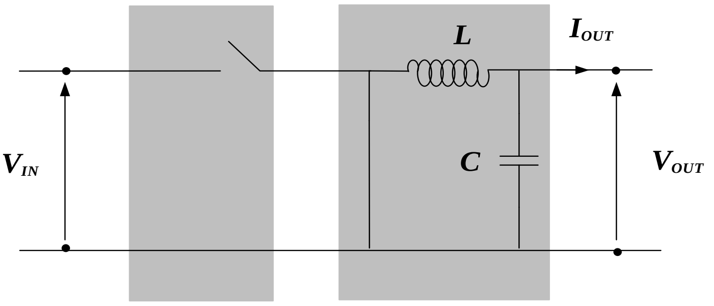

Buck Converter when Switch OFF

Figure II.3. Electrical circuit of buck converter for OFF switching mode.

$$\begin{cases} \dfrac{di_L}{dt} = \dfrac{1}{L}(-v_{OUT}) \\ \dfrac{dv_{OUT}}{dt} = \dfrac{1}{C}(i_L - \dfrac{v_{OUT}}{R}) \end{cases} \tag{II.8}$$

The representationof the state matrix X and the output Y using Eq. (II.8) yields the following:

$$\overset{\bullet}{X} = \begin{bmatrix} \dfrac{di_L}{dt} \\ \dfrac{dv_{OUT}}{dt} \end{bmatrix} = \begin{bmatrix} 0 & -\dfrac{1}{L} \\ \dfrac{1}{C} & -\dfrac{1}{RC} \end{bmatrix} \times \begin{bmatrix} i_L \\ v_{OUT} \end{bmatrix} + \begin{bmatrix} 0 \\ 0 \end{bmatrix} \times \left[v_{IN} \right] \tag{II.9}$$

Consequently, according to (II.7) and (II-9), here is the state space representation of the buck converter:

$$\overset{\bullet}{X} = \begin{bmatrix} \dfrac{di_L}{dt} \\ \dfrac{dv_{OUT}}{dt} \end{bmatrix} = \begin{bmatrix} 0 & -\dfrac{1}{L} \\ \dfrac{1}{C} & -\dfrac{1}{RC} \end{bmatrix} \times \begin{bmatrix} i_L \\ v_{OUT} \end{bmatrix} + \begin{bmatrix} \dfrac{D}{L} \\ 0 \end{bmatrix} \times \left[v_{IN} \right] \tag{II.10}$$

$$Y = \begin{bmatrix} 0 & 1 \end{bmatrix} \times \begin{bmatrix} i_L \\ v_{OUT} \end{bmatrix} + \left[0 \right] \times \left[v_{IN} \right] \tag{II.11}$$

When the operating case of the inductor is in a steady state, it can be concluded that the value of inductor current (I_L) at the end of the OFF state and the value of I_L at the start of the ON state must be the same. Meaning that, the sum of the variations of I_L throughout the OFF and ON states must equal zero as given as follows.

$$\Delta I_{LON} + \Delta I_{LOFF} = 0 \tag{II.12}$$

As a function of the duty cycle D and T_S, the formula that expresses the relationship between input voltage v_{IN} and output voltage v_{OUT} is given as follows:

$$\frac{(v_{IN} - v_{OUT})DT_S}{L} = \frac{v_{OUT}(1-D)T_S}{L} \tag{II.13}$$

The buck converter's conversion ratio can be expressed as follows using equation (II.13):

$$M(D) = \frac{v_{OUT}}{v_{IN}} = D \tag{II.14}$$

Particularly, the duty cycle switching ratio D is proportional to the conversion ratio M(D). Fig. II.4 shows the curve that explains the conversion ratio of the buck converter.

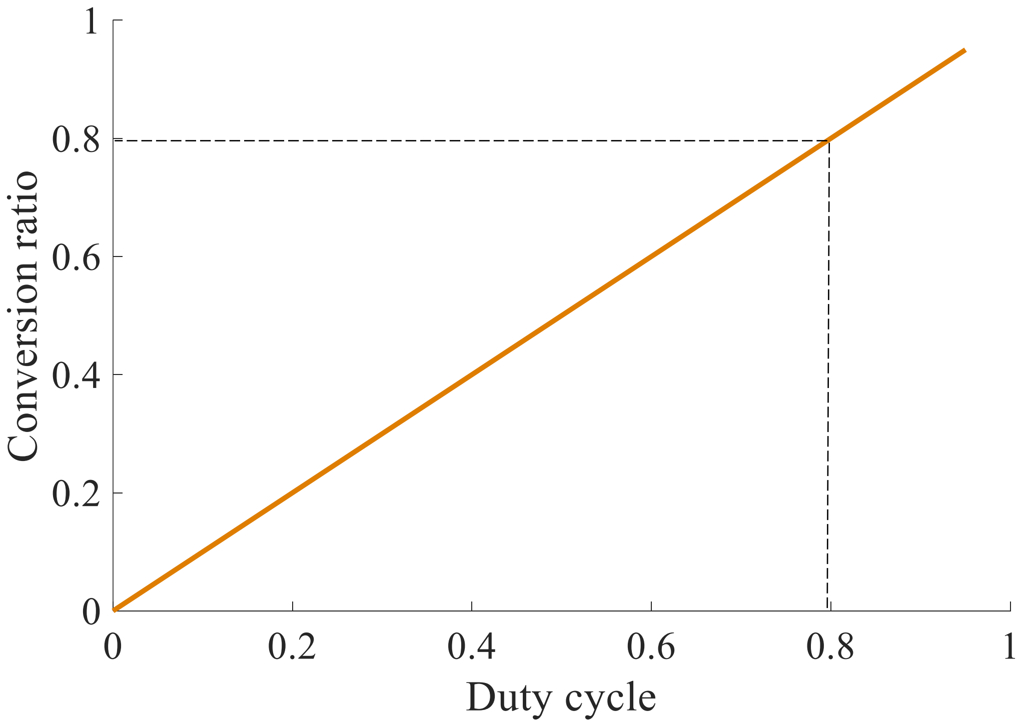

Figure II.4. Conversion ratio of buck converter.

II.2.2 The boost converter

A boost converter, also known as a step-up converter, takes an input DC voltage and transforms it into another DC voltage at the output with a greater magnitude. This converter is made up of the switch (*S*), the inductor (*L*), and the diode (*D*), which stops current from flowing backwards through the switch *S*. And then the capacitor (*C*) keeps the output voltage steady and smooth. It is feasible to utilize this kind of converter in order to harvest the maximum amount of power i.e. MPP possible from the PV system [6].

II.2.2.1 Principle of operation of the boost converter:

Depending on the position of switch *S* as depicted in Fig. II.5, the boost converter's functionality can be separated into two stages:

- During the energy accumulation sequence: in the state of the switch *S* is closed, the inductor current increases, storing magnetic energy. Diode *D* is blocked and the load becomes unconnected.
- The inductor is connected in series with the input voltage while the switch is turned on and its emf is added to the source's (booster effect). Via the diode *D*, capacitor *C*, and load *R*, the inductor current goes to its terminal. Hence, the energy stored in the inductor is discharged into the capacitor and then to the load.

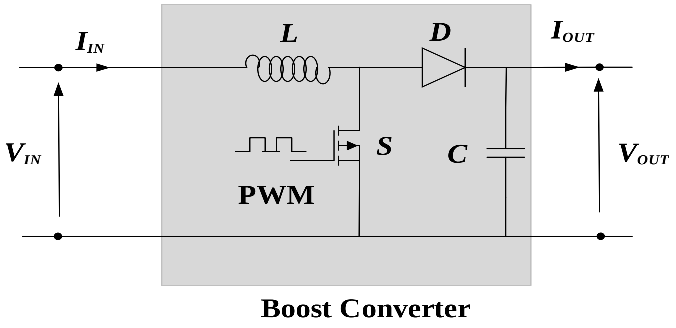

Figure II.5. Electrical circuit of a boost converter.

II.2.2.2 Boost converter circuit model and the state-space representation:

The inductor and capacitor, two crucial components of the boost converter, serve as the starting point for the mathematical modelling of the converter as a whole. Time-domain and frequency-domain analyses of boost converters are possible with the use of mathematical models developed using the state space technique. The following steps show how to construct a state space model of a boost converter using standard large-signal modelling. The state representation of a system, which describes its behavior as a function of time, consists of the two equations below [7].

$$\begin{cases} \dot{X} = f(x,u,t); \text{ state equation} \\ Y = g(x,u,t); \text{ output equation} \end{cases} \tag{II.15}$$

In the case when it is assumed that the system under consideration is linear, the representation of the state is as follows:

$$\begin{cases} \dot{X} = Ax + Bu \\ Y = CX + Du \end{cases} \tag{II.16}$$

The matrix state X is presented in the following manner with regard to the boost converter case:

$$X = \begin{bmatrix} i_L \\ v_{OUT} \end{bmatrix} \tag{II.17}$$

where A, B, C, and D stand for the matrices of the converter's state space representation, in which X represents the state variable, u represents the input, and Y represents the output.

Fig II.6 depicts a boost converter in which the switching mode is ON; in this instance, the continuous conduction mode is assumed for the operating case, and the corresponding equations for the state space are given as follows.

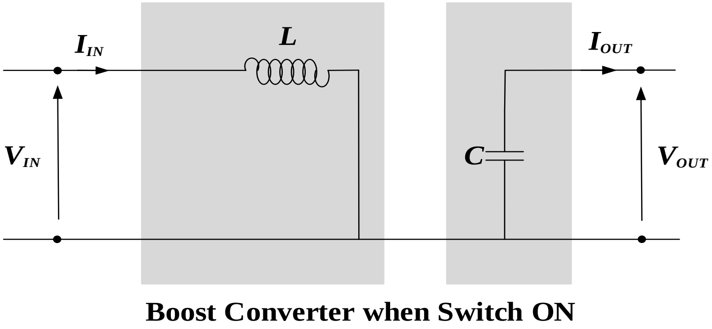

Figure II.6. Electrical circuit of a boost converter in case of ON switching mode.

$$\begin{cases} \frac{di_L}{dt} = \frac{1}{L}(v_{IN}) \\ \frac{dv_{OUT}}{dt} = \frac{1}{C}(-\frac{v_{OUT}}{R}) \end{cases} \tag{II.18}$$

The state matrix *X* and the output *Y* can be found by using the following formula, which is derived from equation II.18:

$$\overset{\bullet}{X} = \begin{bmatrix} \frac{di_L}{dt} \\ \frac{dv_{OUT}}{dt} \end{bmatrix} = \begin{bmatrix} 0 & 0 \\ 0 & -\frac{1}{RC} \end{bmatrix} \times \begin{bmatrix} i_L \\ v_{OUT} \end{bmatrix} + \begin{bmatrix} \frac{1}{L} \\ 0 \end{bmatrix} \times \begin{bmatrix} v_{IN} \end{bmatrix} \tag{II.19}$$

$$Y = \begin{bmatrix} 0 & 1 \end{bmatrix} \times \begin{bmatrix} i_L \\ v_{OUT} \end{bmatrix} + \begin{bmatrix} 0 \end{bmatrix} \times \begin{bmatrix} v_{IN} \end{bmatrix} \tag{II.20}$$

Nevertheless, when the switching operation of the boost converter is turned OFF, as shown in Fig. II.7, the state space equations are as described in the following:

$$\begin{cases} \frac{di_L}{dt} = \frac{1}{L}(v_{IN} - v_{OUT}) \\ \frac{dv_{OUT}}{dt} = \frac{1}{C}(i_L - \frac{v_{OUT}}{R}) \end{cases} \tag{II.21}$$

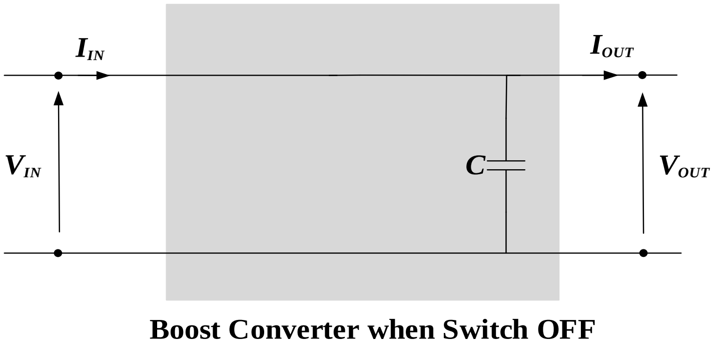

Figure II.7. Electrical circuit of a boost converter in case of OFF switching mode.

State matrix *X* and output matrix *Y* can be calculated using Eq. (II.21), as shown below.

$$\overset{\bullet}{X} = \begin{bmatrix} \frac{di_L}{dt} \\ \frac{dv_{OUT}}{dt} \end{bmatrix} = \begin{bmatrix} 0 & -\frac{1}{L} \\ \frac{1}{C} & -\frac{1}{RC} \end{bmatrix} \times \begin{bmatrix} i_L \\ v_{OUT} \end{bmatrix} + \begin{bmatrix} \frac{1}{L} \\ 0 \end{bmatrix} \times \left[v_{IN} \right] \tag{II.22}$$

The average large signal state space model can be defined as follows when the averaging approach is used to the boost converter equations for the switching mode ON and OFF.

$$\overset{\bullet}{X} = \begin{bmatrix} \frac{di_L}{dt} \\ \frac{dv_{OUT}}{dt} \end{bmatrix} = \begin{bmatrix} 0 & -\frac{(1-D)}{L} \\ \frac{(1-D)}{C} & -\frac{1}{RC} \end{bmatrix} \times \begin{bmatrix} i_L \\ v_{OUT} \end{bmatrix} + \begin{bmatrix} \frac{1}{L} \\ 0 \end{bmatrix} \times \left[v_{IN} \right] \tag{II.23}$$

$$Y = \begin{bmatrix} 0 & 1 \end{bmatrix} \times \begin{bmatrix} i_L \\ v_{OUT} \end{bmatrix} + \left[0 \right] \times \left[v_{IN} \right] \tag{II.24}$$

During the operating case of the inductor is at the steady state, it can be concluded that the value of inductor current (I_L) at the end of the OFF state and the value of I_L at the start of the ON state must be the same. Meaning that, the sum of the variations of I_L throughout the OFF and ON states must equal zero as expressed hereafter.

$$\Delta I_{LON} + \Delta I_{LOFF} = 0 \tag{II.25}$$

As a function of the duty cycle D, the formula that expresses the relationship between input voltage v_{IN} and output voltage v_{OUT} is given as follows:

$$\frac{(v_{IN})DT_S}{L} = \frac{(v_{OUT} - v_{IN}) \times (1-D) \times T_S}{L} \tag{II.26}$$

The boost converter's conversion ratio can be expressed as follows using equation (II.26):

$$M(D) = \frac{v_{OUT}}{v_{IN}} = \frac{1}{1-D} \text{ so } D = 1 - \frac{v_{IN}}{v_{OUT}} \tag{II.27}$$

The curve of the boost converter's conversion ratio is shown in Fig. II.8 as an illustrative example.

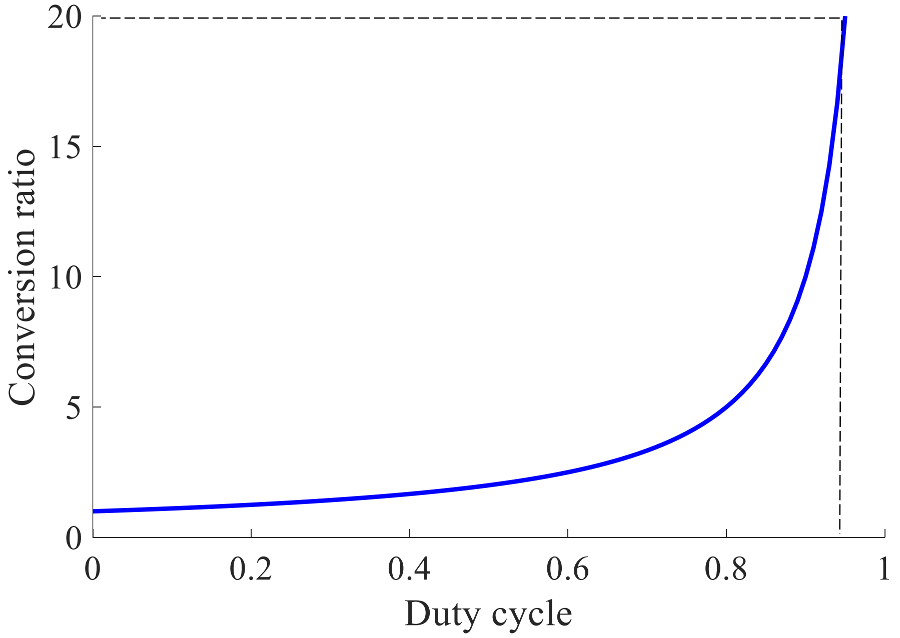

Figure II.8. Conversion ratio of boost converter.

II.2.3 The buck-boost converter

In Fig II.9, we see a buck-boost converter, another kind of simple switched-mode converter. The buck-boost converter has the ability to produce an output voltage that is either higher than or lower than the voltage that is input voltage into the device. This circuit operates on the same premise as the previous converter circuits converting a DC input voltage to a desired output voltage with the same characteristics as the first two converters [8].

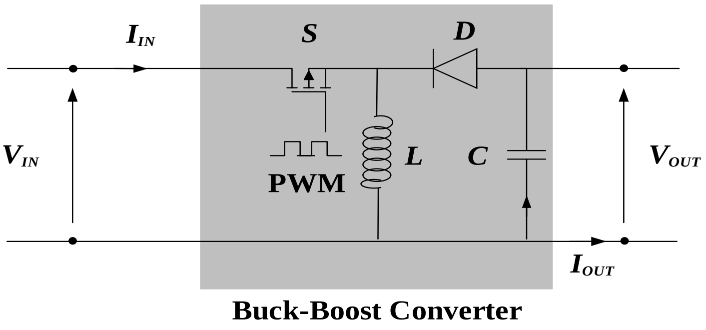

Figure II.9. Electrical circuit of a buck-boost converter.

II.2.3.1 Principle of operation of the buck-boost converter:

Depending on the position of switch *S*, the buck-boost converter's functionality can be separated into two stages:

- When the switch *S* is in its ON position, current flows through it, and the inductor stores great energy.
- The switch *S* is open in the OFF position. Capacitance and load are two more factors that affect the inductor. The latter causes the stored energy in the inductor to be transferred to the load and the capacity. The key distinctions between buck and boost converters are:
- The polarity of the output voltage is the exact opposite of that of the input voltage.
- This device is called a "buck-boost converter." The output voltage may change from 0 to 50% of the duty cycle ratio and behave as a buck converter or step-down converter. From 50% to 100% of the duty cycle ratio behave as a boost converter, or step-up, converter.

II.2.3.2 Buck-boost converter circuit model and the state-space representation:

The inductor and capacitor are the fundamentals for the mathematical modelling of the buck-boost converter since they are the most fundamental components of the converter. The following stages explain how to construct a state-space model of the buck-boost converter based on modelling an average large signal. In the vast majority of instances, the development of the system as a function of time may be characterized by the two equations that are shown below; these equations make up the state representation [9].

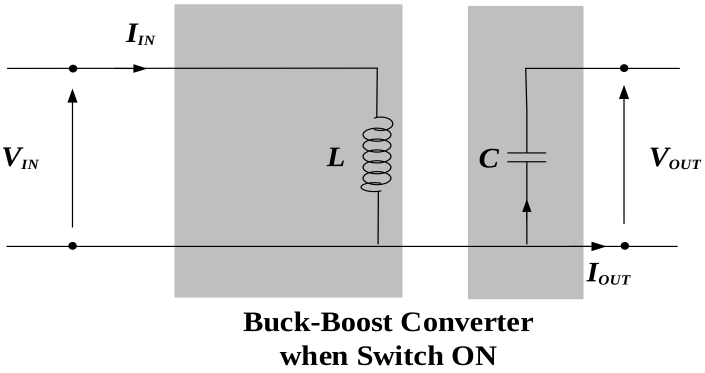

Figure II.10. Electrical circuit of a buck-boost converter in ON switching mode.

$$\begin{cases} \overset{\bullet}{X} = f(x,u,t); \text{ state equation} \\ Y = g(x,u,t); \text{ output equation} \end{cases} \tag{II.28}$$

In the case when it is assumed that the system under consideration is linear, the state representation is as follows:

$$\begin{cases} \overset{\bullet}{X} = Ax + Bu \\ Y = CX + Du \end{cases} \tag{II.29}$$

The following is an introduction to the matrix state *X* for the buck-boost converter case:

$$X = \begin{bmatrix} i_L \\ v_{OUT} \end{bmatrix} \tag{II.30}$$

where *X* represents the state variable, *u* represents the input, *Y* represents the output, and *A*, *B*, *C*, and *D* represent the matrix of the converter's state space.

We analyze the functioning of the corresponding circuit with switch *S* open and closed to derive the mathematical model of the buck-boost converter.

When the switching mode of the buck-boost converter is set to ON, as shown in Fig. II.10, the operating case for the buck-boost converter is the continuous conduction mode. This model is considered to be an assuming mode, and it is in this mode that the state space equations can be determined as follows:

For $T \in [0 \quad DT_S]$, S is close:

$$\begin{cases} \dfrac{di_L}{dt} = \dfrac{1}{L}(v_{IN}) \\ \dfrac{dv_{OUT}}{dt} = \dfrac{1}{C}(-\dfrac{v_{OUT}}{R}) \end{cases} \tag{II.31}$$

Following are the steps that need to be taken in order to generate the state matrix X and the output Y based on Eq. (II.31):

$$\overset{\bullet}{X} = \begin{bmatrix} \dfrac{di_L}{dt} \\ \dfrac{dv_{OUT}}{dt} \end{bmatrix} = \begin{bmatrix} 0 & 0 \\ 0 & -\dfrac{1}{RC} \end{bmatrix} \times \begin{bmatrix} i_L \\ v_{OUT} \end{bmatrix} + \begin{bmatrix} \dfrac{1}{L} \\ 0 \end{bmatrix} \times [v_{IN}] \tag{II.32}$$

$$Y = [0 \quad 1] \times \begin{bmatrix} i_L \\ v_{OUT} \end{bmatrix} + [0] \times [v_{IN}] \tag{II.33}$$

Otherwise, if the buck-boost converter is operating with the switching mode OFF, as shown in Fig. II.11, the corresponding equations for the state space are as follows:

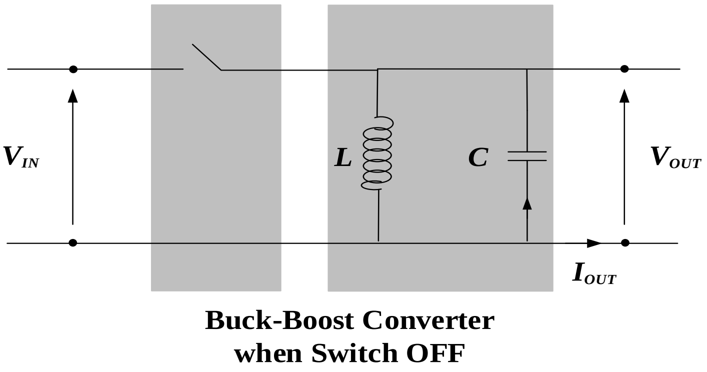

Figure II.11. Electrical circuit of a buck-boost converter in OFF switching mode.

For $T \in [DT_S \quad T_S]$, S is open:

$$\begin{cases} \dfrac{di_L}{dt} = \dfrac{1}{L}(v_{IN} - v_{OUT}) \\ \dfrac{dv_{OUT}}{dt} = \dfrac{1}{C}(-I_L - \dfrac{v_{OUT}}{R}) \end{cases} \tag{II.34}$$

Following are the steps that need to be taken in order to generate the state matrix *X* and the output *Y* based on Eq. (II.34):

$$\overset{\bullet}{X} = \begin{bmatrix} \dfrac{di_L}{dt} \\ \dfrac{dv_{OUT}}{dt} \end{bmatrix} = \begin{bmatrix} 0 & -\dfrac{1}{L} \\ \dfrac{1}{RC} & -\dfrac{1}{RC} \end{bmatrix} \times \begin{bmatrix} i_L \\ v_{OUT} \end{bmatrix} + \begin{bmatrix} \dfrac{1}{L} \\ 0 \end{bmatrix} \times [v_{IN}] \tag{II.35}$$

The matrix representation of the system so becomes as:

$$\overset{\bullet}{X} = \begin{bmatrix} 0 & \dfrac{1-D}{L} \\ \dfrac{1-D}{C} & -\dfrac{1}{RC} \end{bmatrix} \times \begin{bmatrix} i_L \\ v_{OUT} \end{bmatrix} + \begin{bmatrix} \dfrac{D}{L} \\ 0 \end{bmatrix} \times [v_{IN}] \tag{II.36}$$

$$Y = [0 \;\; 1] \times \begin{bmatrix} i_L \\ v_{OUT} \end{bmatrix} + [0] \times [v_{IN}] \tag{II.37}$$

At a steady state, it can be concluded that the value of inductor current (I_L) at the end of the OFF state and the value of I_L at the start of the ON state must be the same. Meaning that, the sum of the variations of I_L throughout the OFF and ON states must equal zero as:

$$\Delta I_{LON} + \Delta I_{LOFF} = 0 \tag{II.38}$$

As a function of the duty cycle *D* and T_S, the formula that expresses the relationship between input voltage v_{IN} and output voltage v_{OUT} is given as follows:

$$\frac{v_{IN} \times DT_S}{L} = \frac{v_{OUT} \times (1-D) \times T_S}{L} \tag{II.39}$$

The buck-boost converter's conversion ratio can be expressed using equation (II.39) as:

$$M(D) = \frac{v_{OUT}}{v_{IN}} = \left(\frac{D}{1-D}\right) \text{so } D = \frac{v_{OUT}}{v_{OUT} - v_{IN}} \tag{II.40}$$

As illustrated in Fig. II.12, which depicts the conversion ratio of the buck-boost converter, the range in which the converter operates as a buck converter when the duty cycle is less than 0.5, and the range in which the converter operates as a boost converter when the duty cycle value is greater than 0.5.

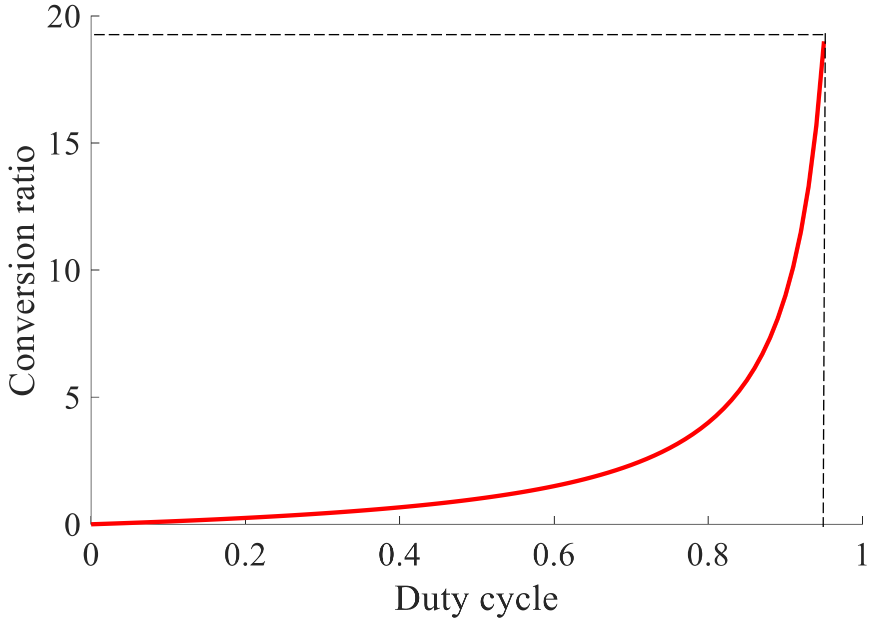

Figure II.12. Conversion ratio of buck-boost converter.

Fig. II.13 expressed the comparison between three ratios of conversion of the three DC-DC converters topologies.

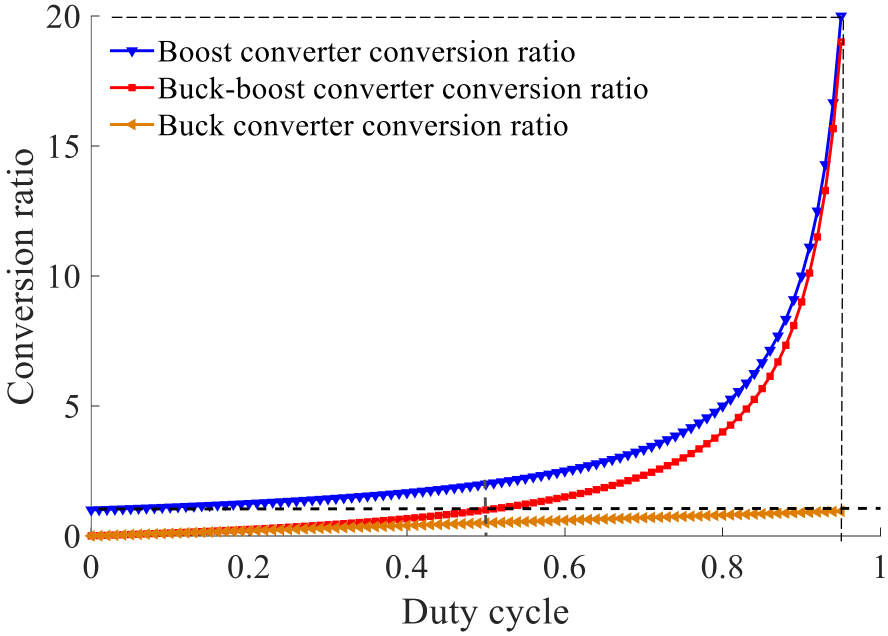

Figure II.13. Conversion ratio of converter buck, boost, and buck-boost.

I.3 The critical analysis of the PV-DC-DC-converters systems characteristics

II.3.1 The schemes under study

To show the dynamic behaviors of the objective functions for the different DC-DC converters depending on the duty cycle when the PV system is subjected to changing the irradiance and disturbance of the load, the three typical structure diagrams have been considered, which are shown in Figs. II.14 (a-b), and (c) for this study. Since these schemes are performed using only voltage sensor signal information, the combined characteristics of the PV panel and their objective functions of DC-DC converters mathematical models are analyzed. Table II.1 provides an overview of the PV panel's technical specifications. Additionally, the power conversion between the PV panel and the load is realized by incorporating DC-DC converters i.e., the buck, boost, and buck-boost, respectively.

Tableau II.1. Characteristics of DM-85 PV Panel at Standard Test Conditions (STC).

Parameters	Labels	Values
Max Power	*Pmax*	85 W
Max Voltage	*Vmax*	17.85 V
Max current	*Imax*	4.77 A
Short-Circuit	*Isc*	5.15 A
Open Circuit voltage	*Voc*	21.8 V
Temperature coefficient of *ISC*	K_V	0.06 %/° C
Temperature coefficient of *VOC*	K_I	-0.35 %/° C
Number of cells	N_S	36

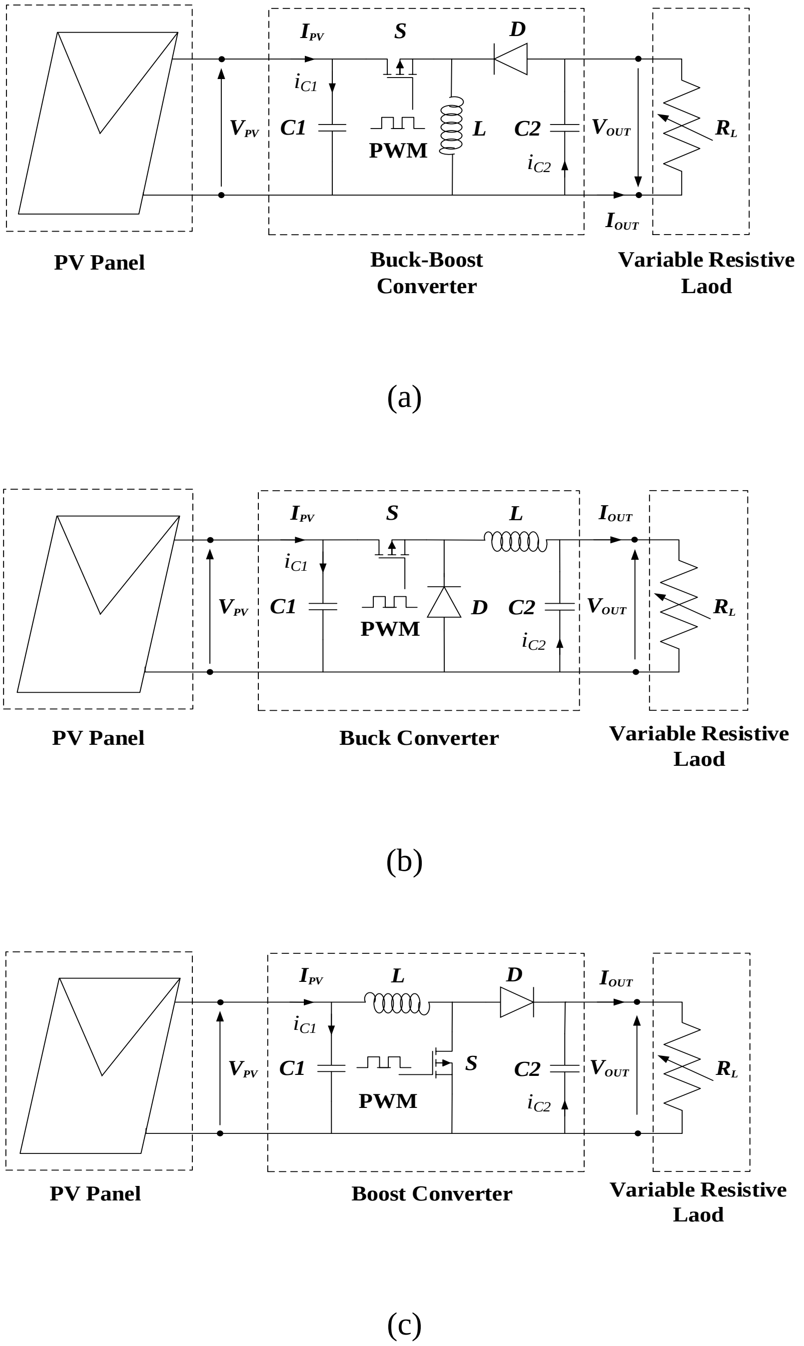

Figure II.14. The structure diagrams of the PV systems under study, (a) PV-buck-boost, (b) PV-buck, and (c) PV-boost converter.

II.3.2 Establishment of the objective functions of three different DC-DC converters mathematical models

The three different DC-DC converters' objective functions are established depending on merging the electrical PV panel characteristics and DC-DC converters' mathematical models' equations, which include only PV input voltage V_{PV_panel} and D with their perturbation as well i.e., ΔV and ΔD. The steps to be followed are described hereafter. The equivalent input resistance (R_{eq}) of PV-buck-boost system can be given in [10] as follows:

$$R_{eq} = \eta \left(\frac{1-D}{D} \right)^2 R_L \tag{II.41}$$

In this study, the effect of the parasitic resistor has been ignored, where Eq. (II.42) describe the relationship between input-output voltage at a steady state of buck-boost with respect to D [10]. These formulas present the key element for objective function Q i.e., gain transfer of a buck-boost converter as follows:

$$V_{out} = \frac{D}{1-D} V_{PV\_panel} \tag{II.42}$$

Considering equation Eq. (II.41), the formula of PV module power (P) is given as follows:

$$P = \frac{{V_{PV\_panel}}^2}{R_{eq}} \tag{II.43}$$

By integrating Eq. (II.41) and Eq. (II.42) in Eq. (II.43), the PV power equation can be expressed as follows:

$$P = \frac{{V_{PV\_panel}}^2}{\eta R_L}\left(\frac{D}{1-D}\right)^2 \tag{II.44}$$

To avoid the issue of the calculation complex process of the objective function, the PV power under square root ($\sqrt{P}$) is used, thus the square root of P can be expressed as:

$$\sqrt{P} = \sqrt{\frac{{V_{PV\_panel}}^2}{\eta R_L}\left(\frac{D}{1-D}\right)^2} \tag{II.45}$$

As obvious in Fig. II.15, both P and $\sqrt{P}$ slopes at MPP are zeroed. Consequently, the objective function Q at MPP can be expressed from the derivative formula $d\sqrt{P}/dD = 0$ as follows:

$$\frac{d\sqrt{P}}{dD} = \left(V_{PV\_panel}\frac{(1-D)+D}{(1-D)^2} + \left(\frac{D}{1-D}\right)\left(\frac{dV_{PV\_panel}}{dD}\right)\right)\frac{1}{\sqrt{\eta R_L}} = 0 \tag{II.46}$$

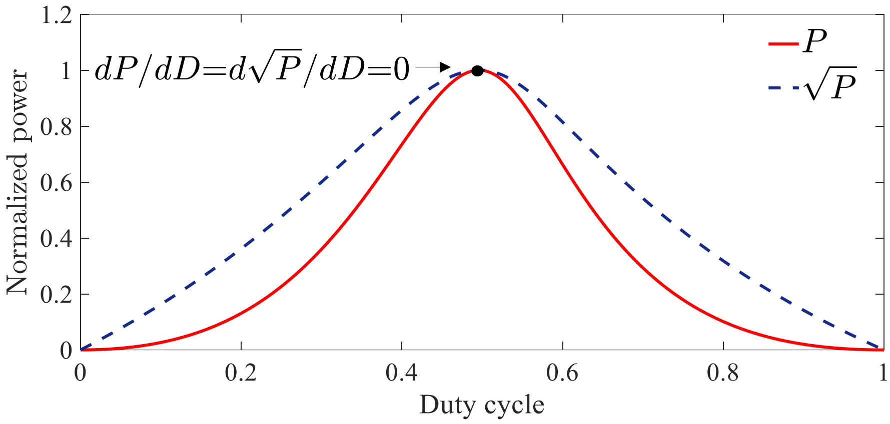

Figure II.15. Variation of P and $\sqrt{P}$ with respect to D.

To simplify this expression formula can be written as follows:

$$\frac{d\sqrt{P}}{dD}=\left(\frac{V_{PV\_\mathrm{mod}}dD+D(1-D)dV_{PV\_\mathrm{mod}}}{(1-D)^2\,dD}\right)\frac{1}{\sqrt{\eta R_L}}=0 \qquad \text{(II.47)}$$

Thus, the following equation expresses the objective function $Q_{buck\text{-}boost}$ of the buck-boost converter:

$$\text{where } Q_{buck-boost} \text{ is } (V_{PV\_panel}+D(1-D)dV_{PV\_panel}/dD) \qquad \text{(II.48)}$$

Since the input-output voltage considered in the formula for the buck converter is introduced in [11] as:

$$V_{out}=DV_{PV\_panel} \qquad \text{(II.49)}$$

Then, by using the same derivation manner of $Q_{buck\text{-}boost}$, the objective function that considers buck converter Q_{buck} can be expressed as:

$$\text{where } Q_{buck} \text{ is } (V_{PV\_panel}dD+DdV_{PV\_panel}) \qquad \text{(II.50)}$$

while the relationship that comprises the input-output voltage in the specific formula of the boost converter is formulated in [12] as follows:

$$V_{out}=\frac{1}{1-D}V_{PV\_panel} \qquad \text{(II.51)}$$

Using the same context for the boost converter, its objective function formula can be written as follows:

$$\text{where } Q_{boost} \text{ is } (dV_{PV\_panel} + (dDV_{PV\_panel}) / (1-D)) \qquad \text{(II.52)}$$

where the perturbative sequence of the *Q* considering the states of duty cycle within three levels is described hereafter:

The variation of *Q* is shown in Fig II.14. When the MPP is tracked, *Q* oscillates around zero during the steady-state regime around three points, it is pulled away from the zero during the search for a new MPP.

II.3.3 Establishment of the combined PV current with DC-DC converter mathematical model with respect to PV characteristics of the three topologies

To combine the PV characteristics with the DC-DC converter mathematical models, the gain transfer at a steady state of the buck-boost converter may be expressed as follows, given the input-output current of this PV system:

$$I_{out} = \frac{1-D}{D} I_{PV\_panel} \qquad \text{(II.53)}$$

where I_{PV_panel} and I_{out} are the PV panel current and output system current, while the formula that describes the load line with respect to the duty cycle for buck-boost converter that is seen by PV can be formulated as:

$$I_{PV\_panel} = \frac{V_{PV\_panel}}{R_L} \left(\frac{D}{1-D} \right)^2 \qquad \text{(II.54)}$$

In the same context, the formula of buck converter can be expressed as:

$$I_{PV\_panel} = \frac{V_{PV\_panel}}{R_L} D^2 \tag{II.55}$$

And then, for boost converter can be presented as follows:

$$I_{PV\_panel} = \frac{V_{PV\_panel}}{R_L} \left(\frac{1}{1-D} \right)^2 \tag{II.56}$$

In addition to that, with respect to the expression of the ideal output current of the PV panel (I_{PV_panel}) that is given as:

$$I_{PV\_panel} = I_{sc} - I_{rs} \left(e^{\frac{V_{PV\_panel}}{\alpha V_T}} - 1 \right) \tag{II.57}$$

where I_{rs} is the diode reverse saturation current, I_{SC} is the short circuit current, α is the diode ideality factor, and V_T is the temperature potential of the p-n junction. Thus, by using Eq. (II.56) and Eq. (II.57), the equation that represents the combination between PV and buck-boost converter i.e. PV-buck-boost system can be expressed as follows:

$$I_{sc} - I_{rs} \left(e^{\frac{V_{PV\_panel}}{\alpha V_T}} - 1 \right) - \frac{V_{PV\_panel}}{R_L} \left(\frac{D}{1-D} \right)^2 = 0 \tag{II.58}$$

Likewise, replacing Eq. (II.55) in Eq. (II.57) for the PV-buck system,

$$I_{sc} - I_{rs}\left(e^{\frac{V}{\alpha V_T}} - 1\right) - \frac{V_{PV\_panel}}{R_L} D^2 = 0 \tag{II.59}$$

Also, when replacing Eq. (II.56) in Eq. (II.57) can be written for the PV-boost system as follows:

$$I_{sc} - I_{rs}\left(e^{\frac{V}{\alpha V_T}} - 1\right) - \frac{V_{PV\_panel}}{R_L}\left(\frac{1}{1-D}\right)^2 = 0 \tag{II.60}$$

II.3.4 PV-DC-DC converters behavior under irradiance changing

The electrical characteristics of the PV-DC-DC converters systems are shown in Fig. II.16, which depicted the power, objective function, and voltage versus duty cycle using the three converter topologies. The level of irradiation *G* is changed, while R_L is fixed at 10 Ω. In addition, the state of *T* is not considered due to its changing is much slower compared to *G*; accordingly, its effect on the MPP tracking is almost negligible. Thus, *T* is the choice according to STC 25°C.

The *P-D*, *Q-D*, and *V-D* characteristic curves are different from one PV-DC-DC converter to another with regard to the duty cycle characteristics. In particular, there are "non-operational" regions for PV-buck and PV-boost systems. These regions are characterized by a specific value of DMPP that is either greater than unity or lower than zero, depending on the system. As an illustration, when *G* is equal to 500 to 1000 W/m^2, the operating region, or DMPP, of MPP for the PV-buck system can be found to be greater than 1. Contrary to when considering the PV-boost system, the operating region is less than zero for G = 100 to 500 W/m^2, respectively. As a result of the inability to achieve this scenario in the context of practice implementation, both converters are unable to operate in the regions under consideration. Otherwise, the MPP will always be within the operational range of the PV-buck-boost system, which is defined as 0 to 1 for the DMPP. This demonstrates the capability of buck-boost to implement MPPT in an efficient manner across a full *P-D* plane.

It is also possible to see this phenomenon illustrated in Fig. II.16, in which the position of the MPP along the *P-D* or *P-Q* curves moves substantially with regard to *G*. This is opposite to the *P-D* curve, which shows a more constrained change in the position of DMPP. In a similar case, for PV-buck-boost, the DMPP remains constrained within a limited range (0.33 to 0.63) even as *G* increases from 500 to 1000 W/m^2.The *P-D* curve that is displayed in Fig. II.16(f) provides an indication of this region. As will be demonstrated in the following section, the objective function must be close to zero in order to accomplish maximum power point tracking (MPPT) when the irradiation and the load both change.

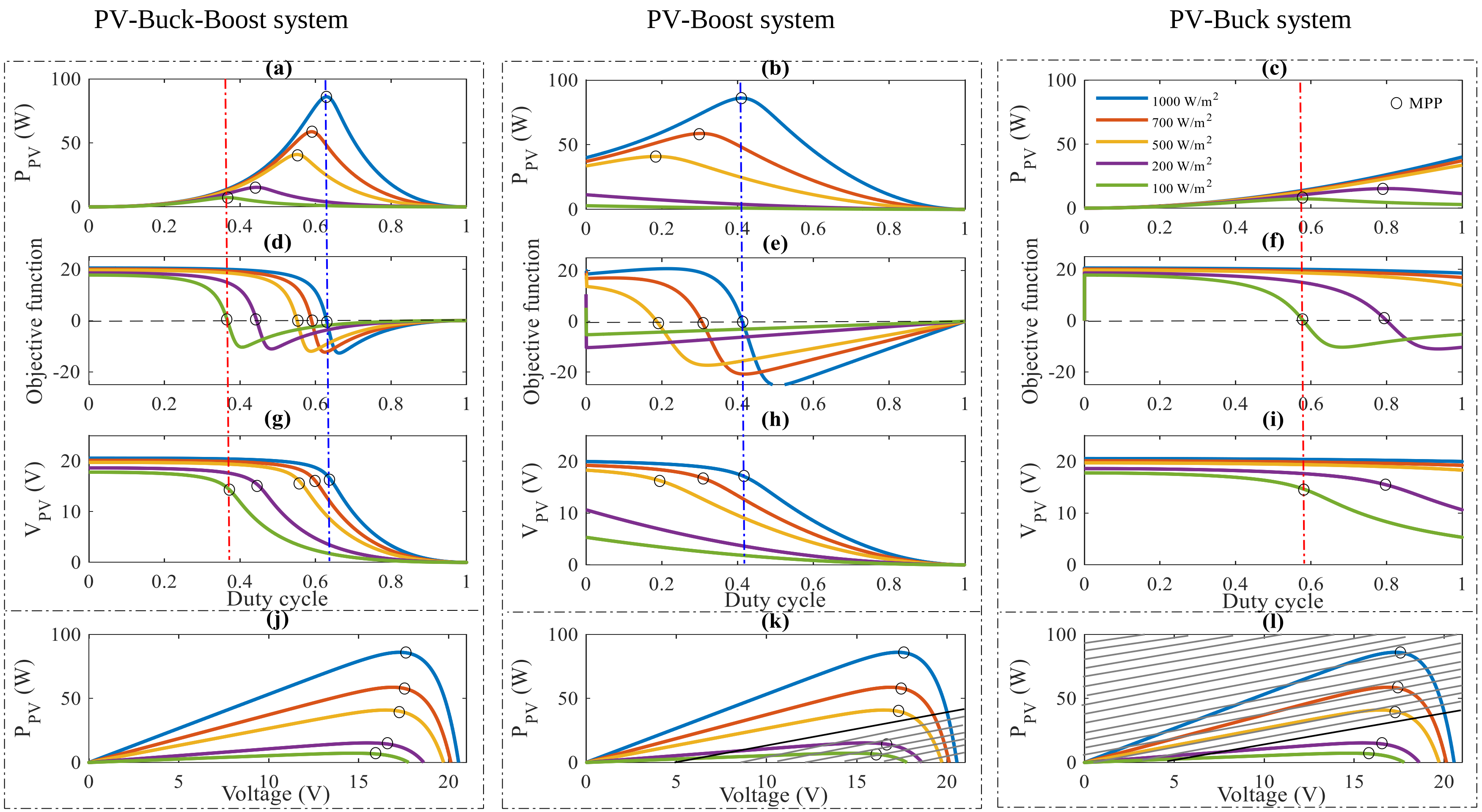

Figure II.16. Electrical characteristics under changing the irradiance with fixed load value at 10 Ω. The *P-D*, *Q-D* and *V-D* characteristics are shown in Fig. II.16. (a), (d) and (g), for PV-buck-boost converter, and (b), (e), and (h) for PV-boost converter, while for PV-buck converter are shown in (c), (f), and (i) respectively. Moreover, the *P-V* characteristics at different irradiance levels are shown in Fig. II.16. (j), (k), and (l) for the PV-buck-boost, PV-boost, PV-buck, respectively.

II.3.5 PV-DC-DC converters behavior under load disturbance

In Fig. II.17, we can observe the way the objective function *Q* behaves during the load disturbance as well as the electrical characteristics of the PV-DC-DC converter systems. Thus, it can be seen that the duty cycle for PV-buck-boost at maximum power point (DMPP) is limited to values between 0.28 and 0.8 when the load value varies from 1 Ω to 100 Ω while *G* remains constant at 500 W/m^2. The buck-boost converter's operating region is the entire *P*-*D* or *Q*-*D* plane, which is able to work at any load level. When there is an unexpected change in load, DMPP will move to the right when the load increases and to the left when the load decreases. Consequently, power versus duty cycle (*P* versus *D*), objective function versus duty cycle (*Q* versus *D*), and voltage versus duty cycle (*V* versus *D*) can all be seen clearly in Fig. II.17 (a), (d), and (g), respectively.

Conversely, there are "non-operational" zones for PV-buck and PV-boost systems, where the theoretical value of DMPP is greater than unity or less than zero. For R_L = 50 Ω and 100 Ω, for instance, the MPP for the PV-buck system is found at DMPP > 1. Yet, with R_L = 50 Ω, 5 Ω, and 1 Ω in the PV-boost system, DMPP < 0. However, the DMPP remained relatively constant between [0.3 and 0.8] for PV-buck-boost while R_L varied from 1 Ω to 50 Ω. The *P*-*D* and *Q*-*D* curves in Fig. II.17(a) and (d) provide an indication of this region.

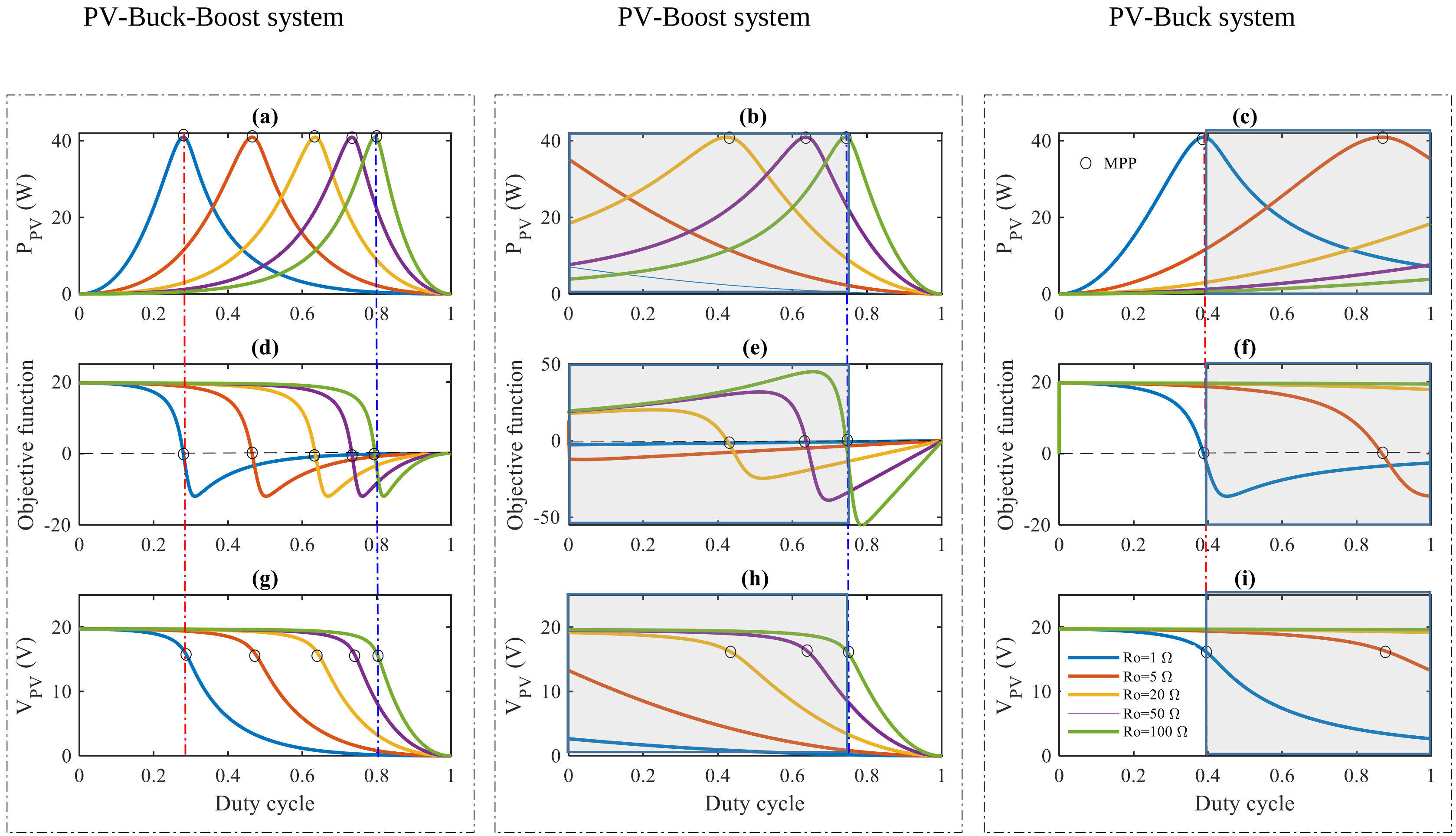

Figure II.17. *P-D*, *Q-D*, and *V-D* characteristics under disturbance of the load with fixed irradiance value at 500 W/m^2. The characteristics of PV-buck-boost are shown in Fig. II.17. (a) and (d), (g), and (b), (e), and (h) for the PV- boost, while (c), (f), and (i) for PV-buck, respectively.

II.3.6 PV-DC-DC converters behavior under temperature changing

In Fig. II.18, we can observe the way the objective function Q behaves during the temperature change as well as the electrical characteristics of the PV-DC-DC converter systems. Thus, for PV-buck-boost it can be seen that the duty cycle at maximum power point (DMPP) is limited to values between 0.47 and 0.53 when the temperature value varies from 10° C to 50° C while G remains constant at 300 W/m^2 and the load 10 Ω. The buck-boost converter's operating region is the entire P-D or Q-D plane, which is able to work at any temperature level. When there is an unexpected temperature change, DMPP will move to the right when the temperature increases and to the left when the temperature decreases. Consequently, power versus duty cycle (P versus D), objective function versus duty cycle (Q versus D), and voltage versus duty cycle (V versus D) can all be seen clearly in Fig. II.18 (a), (d), and (g), respectively.

Conversely, there are "non-operational" zones for PV-buck and PV-boost systems, where the theoretical value of DMPP is greater than unity or less than zero. For T = 30° C and 50° C, for instance, the MPP for the PV-buck system is found at DMPP > 1. Yet, with T = 10° C and 30° C, in the PV-boost system, DMPP < 0. However, the DMPP remained relatively constant between [0.47 and 0.53] for PV-buck-boost while T varied from 10° C to 50° C. The P-D and Q-D curves in Fig II.18(a) and (d) provide an indication of this region.

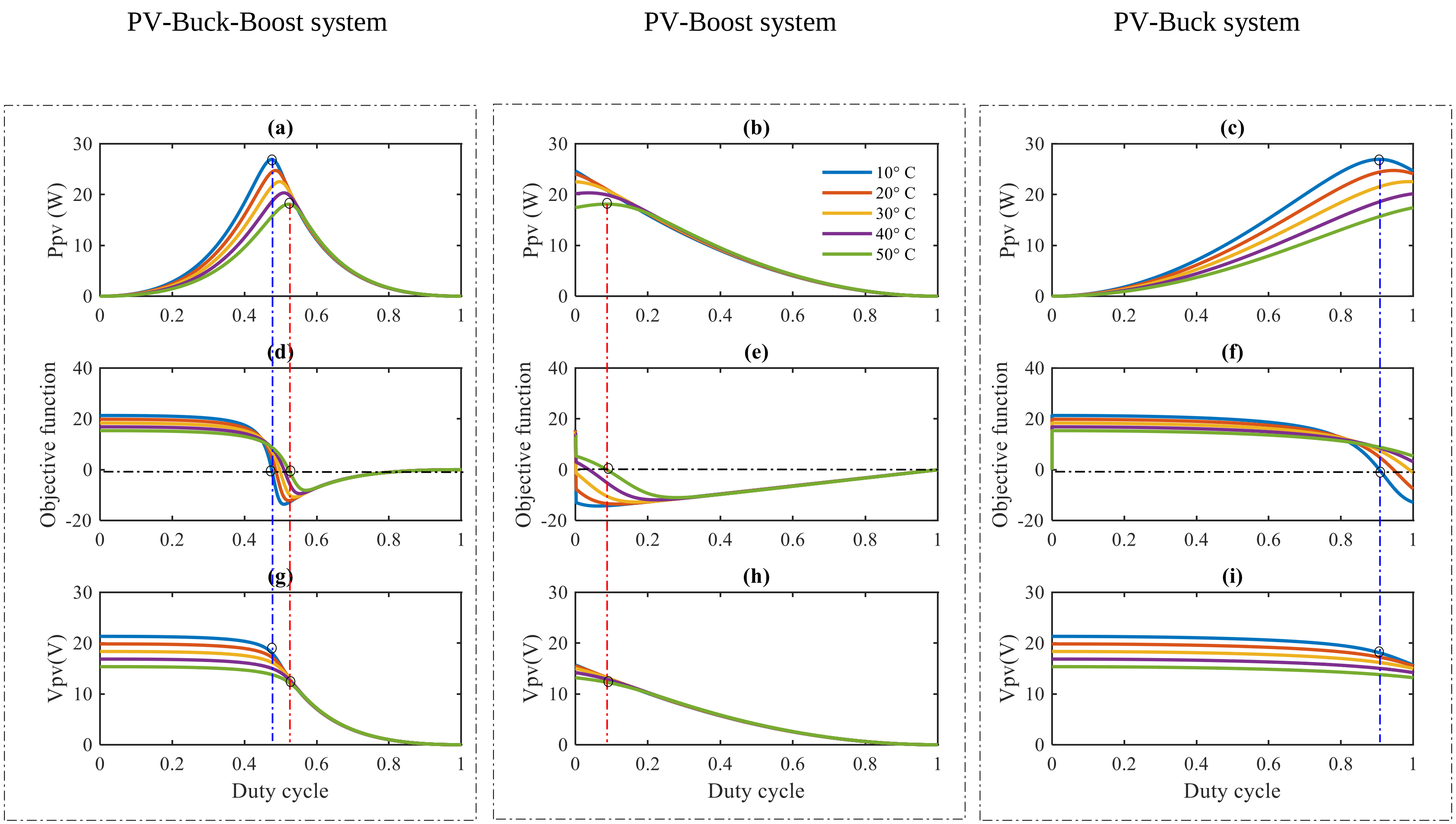

Figure II.18. *P-D*, *Q-D*, and *V-D* characteristics under temperature changing with fixed irradiance value at 300 W/m^2 and 10 Ω for the load. The characteristics of PV-buck-boost are shown in Fig. II.18. (a) and (d), (g), and (b), (e), and (h) for the PV- boost, while (c), (f), and (i) for PV-buck, respectively.

II.4 Conclusion

In the present study, the DC-DC converters for current sensorless controllers are analyzed. The simulation environment is perfect for developing and modelling circuits, as well as for comprehending the dynamic behavior of various converter architectures. The predefined objective function of the three converters are well established. For further illustration, the dynamic behavior of each converter are displayed for different scenarios such as changing the irradiance, disturbance in the load and temperature changing. As a consequence, the findings of the simulation indicate that the buck-boost converter is able to perform full-range operation regardless of the load disturbances or irradiance change that can occur. An in-depth study of the DC-DC converters' behaviors using state-space models for the buck, boost, and buck-boost converters are considered. The first device is referred to as a buck converter, and it works by reducing the DC voltage using a conversion ratio that is equal to D i.e. $M(D) = D$. In the second architecture, known as a boost converter, the switch and the inductor are placed in opposite positions. The converter generates an output voltage that is higher than the input voltage that it receives. The ratio of conversion is denoted by $M(D) = 1/.(1 - D)$. The last converter is a buck-boost converter, and it works by using a switch to link the inductor to the input and output voltages of the power supply in an alternating manner. Its ratio for the conversion is $M(D) = D/(1 - D)$.

II.5 References

[1] H. M. Mahery and E. Babaei, "Mathematical modeling of buck–boost dc–dc converter and investigation of converter elements on transient and steady state responses," *International Journal of Electrical Power & Energy Systems,* vol. 44, pp. 949-963, 2013.

[2] S. Surya and M. Arjun, "Mathematical modeling of power electronic converters," *SN Computer Science,* vol. 2, p. 267, 2021.

[3] M. Killi and S. Samanta, "Voltage-sensor-based MPPT for stand-alone PV systems through voltage reference control," *IEEE Journal of Emerging and Selected Topics in Power Electronics,* vol. 7, pp. 1399-1407, 2018.

[4] J. Ejury, "Buck converter design," *Infineon Technologies North America (TFNA) Corn Desion Note,* vol. 1, 2013.

[5] P. N. Reddy, "STATE SPACE MODELING AND SIMULATION OF DC-DC CONVERTERS USING SIMULINK," 2018.

[6] S. A. Lopa, S. Hossain, M. Hasan, and T. Chakraborty, "Design and simulation of DC-DC converters," *International Research Journal of Engineering and Technology (IRJET),* vol. 3, pp. 63-70, 2016.

[7] V. V., "A Complete Mathematical Modeling, Simulation and Computational Implementation of Boost Converter Via MATLAB/Simulink," 2019.

[8] F. S. Dinniyah, W. Wahab, and M. Alif, "Simulation of buck-boost converter for solar panels using PID controller," *Energy Procedia,* vol. 115, pp. 102-113, 2017.

[9] X. Zhou and Q. He, "Modeling and simulation of buck-boost converter with voltage feedback control," in *MATEC web of conferences*, 2015, p. 10006.

[10] E. Duran, M. Sidrach-de-Cardona, J. Galan, and J. Andujar, "Comparative analysis of buck-boost converters used to obtain I–V characteristic curves of photovoltaic modules," in *2008 IEEE Power Electronics Specialists Conference*, 2008, pp. 2036-2042.

[11] Y.-J. Lee, A. Khaligh, and A. Emadi, "A compensation technique for smooth transitions in a noninverting buck–boost converter," *IEEE Transactions on power electronics,* vol. 24, pp. 1002-1015, 2009.

[12] T.-F. Wu and Y.-K. Chen, "Modeling PWM DC/DC converters out of basic converter units," *IEEE transactions on Power Electronics,* vol. 13, pp. 870-881, 1998.

CHAPTER III

A CURRENT SENSORLESS MPPT CONTROL OF BUCK-BOOST CONVERTER FOR PHOTOVOLTAIC SYSTEMS

III.1 Introduction

In the past decade, the world has faced huge challenges in terms of fluctuations in the cost of fossil fuels such as petroleum and natural gas, along with exhaustion and future shortages of these reserves, which has raised concerns about future energy supply [1]. From the available renewable energy sources, photovoltaic energy is one of the most important alternative solutions to ensure clean electricity production and cater to the pollution problems associated with conventional electricity generation methods. However, the high cost of implementation is one of the main challenges for the big-scale applications of photovoltaic (PV) generation systems [2].

In such applications, the array is composed of a few number of panels and rarely being subjected to partial shading conditions. Therefore, since there is no need to implement complex MPPT algorithms, the cost of implementation can be reduced by implementing simple MPPT algorithms using rapid microcontrollers. Among them, the open-source Arduino rapid prototyping platform is being used recently as a tool for hardware implementation of various types of MPPT with different complexity levels. Table III.1 lists several works that used the Arduino platform for MPPT implementation. Recently, Matlab has added a package toolbox for a wide range of microcontrollers available in the market enabling them to be as target hardware for developed model-based controllers under Simulink. Thus, more complex algorithms developed in the Simulink environment can be easily compiled and loaded into rapid microcontrollers [3].

Table III.1. MPPT Algorithms Experimentally Validated using Arduino Platform.

Authors	MPPT algorithm	Microcontroller used
Killi *et al*, 2015 [4]	Voltage-based MPPT	Atmega2560
Fannakh *et al*, 2018 [3]	Fuzzy logic	Atmega2560
Motahir *et al*, 2018 [5]	Modified Incremental Conductance (IncCond)	Atmega328p
Killi *et al*, 2018 [6]	Voltage-Reference-based MPPT	Atmega2560

Although the operating area of the buck-boost converter is the full *I-V* plane regardless of the load value [7], there is no attempt yet made to propose a voltage-based sensor MPPT using the buck-boost converter. Within this context, the main contribution of this work is firstly to propose a simple and easy way to implement the current sensorless (CSL) MPPT algorithm for buck-boost converters. Second is to present a novel way for hardware validation of Stateflow model-based controllers using a rapid prototyping platform through Simulink support package for Arduino hardware. Thus, the proposed approach is developed using the Stateflow tool and validated under Matlab/Simulink environment. Then, the proposed algorithm is experimentally validated using an Arduino DUE microcontroller board.

The rest of this chapter is arranged as follows: Section 2 presents the system under study and the mathematical model of its components. Section 3 describes the steps to be followed to derive the objective function from the mathematical model of the buck-boost converter. The objective function is the key element for the proposed CSL-MPPT algorithm and the Stateflow chart of the proposed CSL algorithm. Section 4 presents the results of the comparative study among the proposed CSL algorithm and the P&O algorithm obtained via simulation under Matlab/Simulink environment. The hardware implementation of the Stateflow-based CSL algorithm using the rapid Arduino prototyping platform along with the experimental results are presented in Section 5. Conclusion is presented in the last Section.

III.2 The PV system under study

Fig. III.1 shows the topology for the PV system under study with the proposed CSL-MPPT digital controller. The power transformation process from the source (PV panel) to the load (resistive load) is connected through the buck-boost converter. The buck-boost is chosen since of its capacity to work as a step-up/step-down converter, and its capacity to work in the maximum operating range of the *I-V* plane [8, 9, 10,11]. The MPPT digital controller keeps adjusting the PWM duty cycle of the power converter to ensure the operation at the maximum power point (MPP).

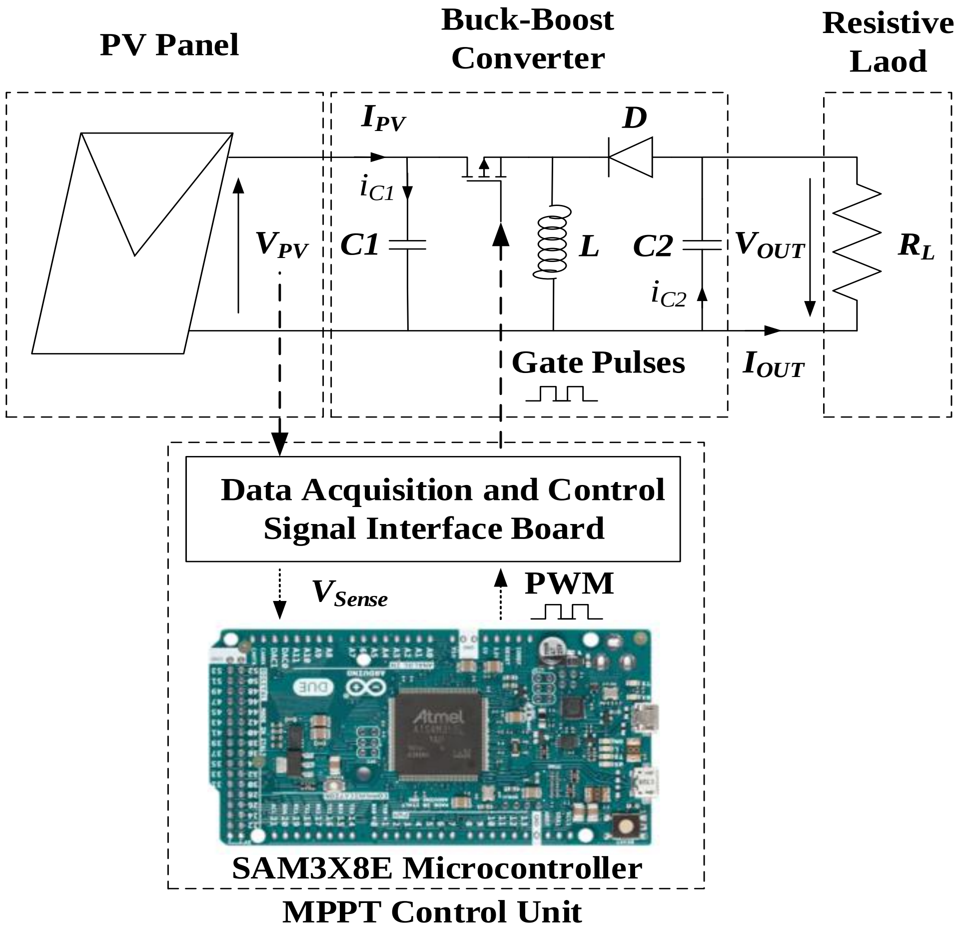

Figure III.1. Topology for the PV system under study and its associated MPPT control unit.

III.3 The proposed current sensorless MPPT algorithm

III.3.1 Establishment of the objective function from the mathematical model of the buck-boost converter

The key element of the proposed CSL-MPPT algorithm is annulling the objective function (*Q*) so that the operating point can be operated at the MPP. The procedure to establish the mathematical formula of *Q* is described hereafter:

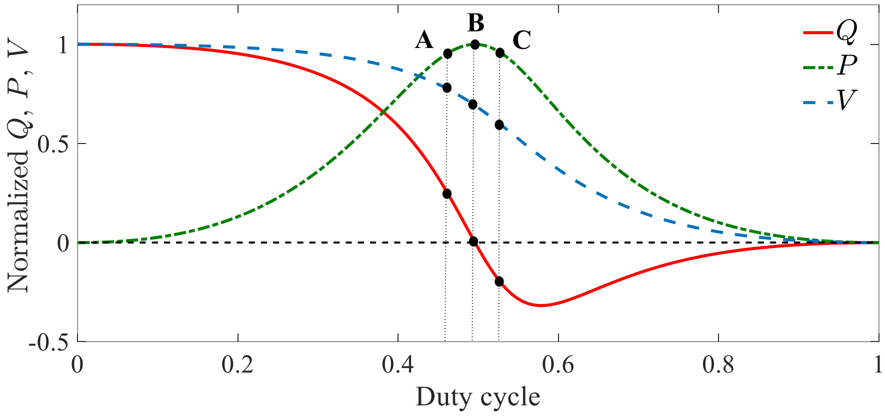

Figure III.2. Operation of the MPP on the *P-D*, *Q-D*, and *V-D* characteristics for the buck-boost converter.

According to Eq. (II.48) the expression of Q for buck-boost converter can be written as follows:

$$Q = V_{PV} + \left(D(1-D)\,dV_{PV} \right) / \,dD \tag{III.1}$$

$$\text{where } Q \begin{cases} = 0, & \text{The operating point is at the MPP} \\ > 0, & \text{The operating point is at the left of the MPP} \\ < 0, & \text{The operating point is at the right of the MPP} \end{cases} \tag{III.2}$$

A plot diagram showing the variation of Q with respect to D with projection on the *P-D* and *V-D* characteristics is depicted in Fig. III.2. Unlike conventional hill-climbing methods, the proposed CSL-MPPT is developed based on the *Q-D* characteristics instead of *P-D* characteristics. Here the objective is to annul Q, i.e. operating around zero, to guarantee the operation at MPP thus $dP/dD = d\sqrt{P}/dD = 0$.

The behavior of the objective function Q and the electrical characteristics of the PV-buck-boost converter system under the load variation are shown in Figs. III. 3(a), (b), and (c), respectively. As can be seen from these figures, the value of the duty cycle at maximum power point (D_{MPP}) is confined between 0.33 to 0.83 with the changing load value from 1 Ω to 100 Ω. As it can be observed that, the operating area of the buck-boost converter is the full *P-D* or *Q-D* plane regardless of the load value. When a sudden change in load occurs, D_{MPP} will be slightly shifted towards the right side when the load increases, and vice versa. Furthermore, obviously in Figs. III. 3(a), (b), and (c), the power versus duty cycle (*P-D*), objective function versus duty cycle (*Q-D*), and voltage versus duty cycle (*V-D*), respectively, where the PV power (*P*), the objective function (*Q*), and the PV voltage (V_{PV}) values at MPP will remain constant; just slightly shifted towards the right side or the left side when the load increases or decreases. It can be concluded that the values of *P*, *Q*, and V_{PV} are not affected by the sudden change in the load, considering the load changing transient.

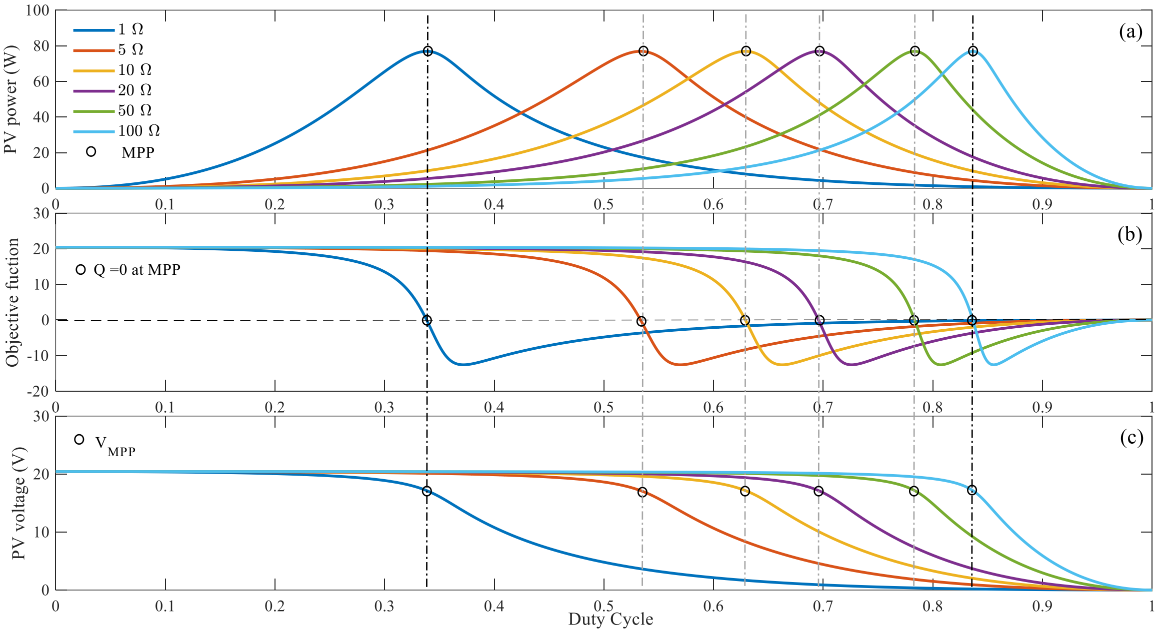

Figure III.3. Electrical characteristics of the PV-buck-boost converter under variation of the load with fixed irradiance at 900 W/m^2 (a) *P-D* characteristics, (b) *Q-V* characteristics, and (c) *V-D* characteristics.

Table III.2 summarizes the published voltage sensor-based MPPT methods using the concept of annulling the objective function (*Q*) derived from the mathematical model of the power converter used for tracking.

Table III.2. Review of Different Published Current Sensorless MPPT Techniques.

Authors	**Objective function (*Q*)**	**Converter**	**Controller Type**
Killi *et al*[4]	$D(1-D)dV_{PV}+V_{PV}dD$	SEPIC	Atmega2560 (AVR core)
Dasgupta *et al*[12]	$V_{PV}dD+DdV_{PV}$	Buck	ADuC831 (8052 core)
Harrag *et al*[13]	ANN based on $dV_{PV}=-(dDV_{PV})/(1-D)$	Boost	Matlab/ Simulink
Proposed	$V_{PV}+D(1-D)dV_{PV}/dD$	Buck-boost	SAM3X8E (ARM- Cortex M3 core)

III.3.2 Stability requirement analysis of *Q*using Lyapunov's second method

The Lyapunov's second method [14] is utilized to analyze the stability of *Q*. The discrete form of *Q* (given in Eq. (III.1)) could be expressed as:

$$Q(k)=V_{PV}(k)+D(1-D)\Delta V(k)/\Delta D(k) \tag{III.3}$$

where *k* is the sampling instant. The objective is to find the requirement that guarantees the stability of *Q*, i.e., *Q* = 0.

where $\Delta V(k)=V_{PV}(k)-V_{PV}(k-1)$ (III.4)

$$\Delta D(k)=D(k)-D(k-1) \tag{III.5}$$

Let's consider the globally positive-definite Lyapunov function ($\mathcal{L}$) given by:

$$\mathcal{L} = \frac{1}{2} Q^2 \tag{III.6}$$

The time derivative of $\mathcal{L}$, denoted by ($\dot{\mathcal{L}}$), is given as follows:

$$\dot{\mathcal{L}} = Q \times \dot{Q} \tag{III.7}$$

To ensure the global asymptotic stability of $\mathcal{L}$, $\dot{\mathcal{L}}$ should be globally negative-definite function i.e., $\dot{\mathcal{L}} < 0$. By using Euler-forward approximation, $\dot{\mathcal{L}}$ can be re-written as:

$$\dot{\mathcal{L}} = Q(k)\left[\frac{Q(k+1) - Q(k)}{T_S}\right] \tag{III.8}$$

where T_S is the sampling time. Assuming that there exist an α strictly positive ($\alpha > 0$) for which $\dot{\mathcal{L}}$ given below is strictly negative-definite function:

$$\dot{\mathcal{L}} = -\alpha Q^2(k) < 0 \tag{III.9}$$

where $Q^2(k) \in \mathbb{R} > 0$. By using Eq. (III.8), and Eq. (III.9), α could be expressed as follows:

$$\alpha = \left[1 - \frac{Q(k+1)}{Q(k)}\right]\frac{1}{T_S} \tag{III.10}$$

From Eq. (III.10), α is strictly positive only when $Q(k+1)/Q(k) < 1$. Thus, to guarantee the global asymptotic stability of Q, the perturbation of D should be designed in such a way that $|Q(k+1)|$ is always inferior than $|Q(k)|$. Hence, the control objective of the proposed CSL-MPPT technique is to annual Q.

As illustrated in Fig. III.2, if the operating point is in the left side of the MPP point A, dP/dD is positive and Q is positive as a consequence. Therefore, D has to be increased

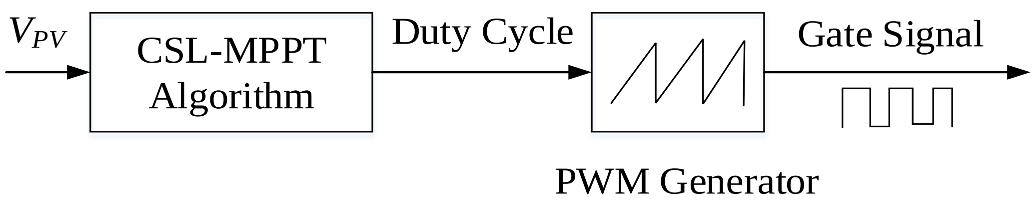

Figure III.4. The control diagram of the proposed CSL-MPPT control.

to perturb the operating point towards the right side of point *B*. Otherwise, if the operating point is in the right side of the MPP point *C*, *dP/dD* is negative thus making *Q* negative too. Therefore, *D* has to be decreased to perturb the operating point towards the left side. Depending on the observed facts, the rule of perturbation of *D* in the proposed CSL-MPPT algorithm is defined as follows:

$$\begin{cases} D(k+1) = D(k) + D_S, \ \text{if the operating of } Q > 0 \\ D(k+1) = D(k) - D_S, \ \text{if the operating of } Q < 0 \end{cases} \tag{III.11}$$

III.3.3 Description of the proposed CSL-MPPT

Fig. III.4 displays the topology of the direct control scheme of the proposed CSL-MPPT. The duty cycle value is calculated and updated directly without the need of any control loop such as PI. This scheme offers several advantages: First, it streamlines the hierarchy of the control strategy. Second, eliminates the need of current sensor. Third, it has lower computational time, since only one ADC conversion is required. Fundamentally, it streamlines the execution of the PI-based MPPT tracking while conserving almost similar results [9].

The flowchart of the proposed CSL-MPPT method is revealed in Fig. III.5. The flowchart includes six principal steps, five of them are periodically executed to ensure the MPP tracking.

*Step*①: Initialization of the duty cycle *D* based on Eq. (II.42).

*Step*②: Sensing V_{PV} and calculation of ΔV and ΔD.

Step ③: Calculation of *Q* using Eq. (III.1).

*Step*④: Decision of the direction of perturbation of *D*.

*Step*⑤: Storage of the actual values of the *D* and V_{PV}.

Step ⑥: Transmitting the updated *D* to the converter.

The last five steps keep executing periodically after a predefined sampling time, denoted by T_S.

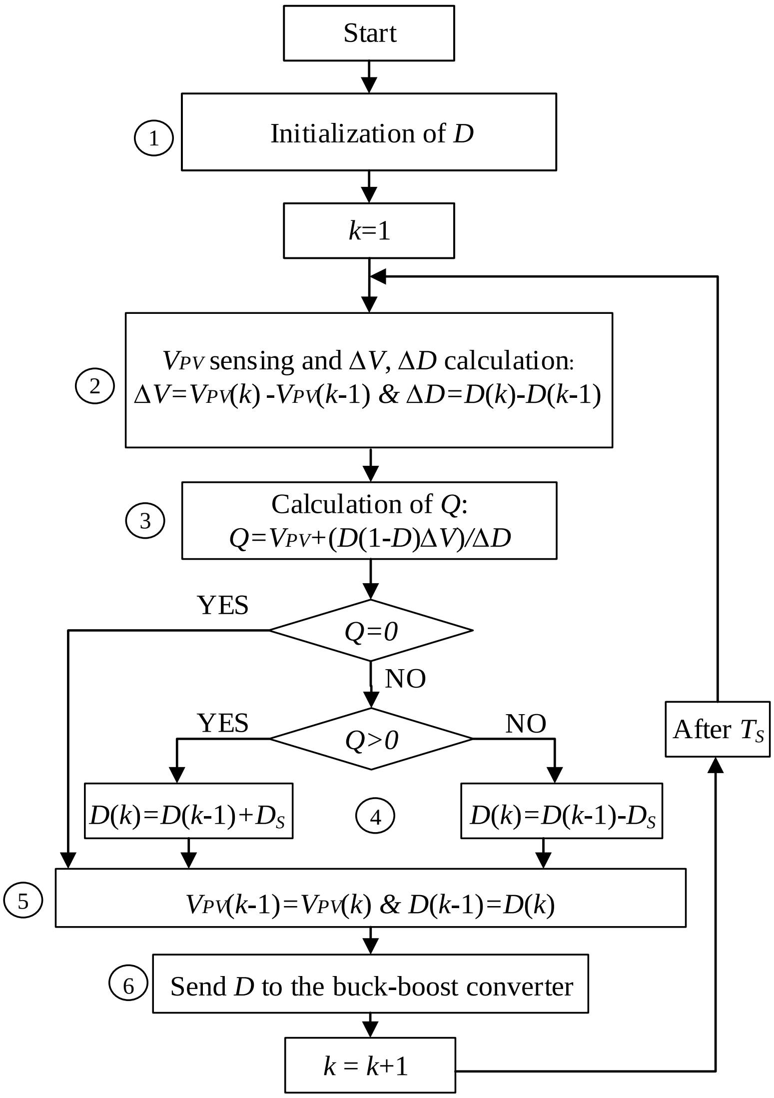

Figure III.5. Flowchart of the proposed CSL-MPPT algorithm.

Stateflow is a powerful tool for model-based controller design using a finite state. It contains tools making the development and debugging processes easy and fast, such as access to the values of variables during the algorithm execution, and the possibility to carry out checks of the errors when executing the algorithm. It provides an efficient C code generation for target hardware [15]. Fig. III.6 displays the chart of the CSL-based MPPT under the Stateflow environment. The CSL chart is a set of finite states that represent the possible operating modes of the CSL-MPPT algorithm. The execution steps of the CSL method are depicted in the flowchart of Fig. III.5 are reproduced in chart of Fig. III.6. Thus, the steps of construction of the CSL Stateflow chart are presented in Fig. III.6 as follows:

- The initialization of D and the step size of the duty cycle perturbation (D_S) is made in the first state labeled ①.
- V_{PV} is sensed after T_S= 20 ms and ΔV, ΔD, denoted by DV, DD, respectively, can be calculated during state ② activation.
- In state ③, ΔV, and ΔD values are used to calculate Q.
- The decision of the perturbation direction of D is made by executing either *Increases_Duty_Cycle* or *Decreases_Duty_Cycle* states ④ depending on the sign of Q.
- In state ⑤, the actual values of V_{PV} and D are stored for the next MPPT cycle.

The updated D is transmitted to the converter in state ⑥.

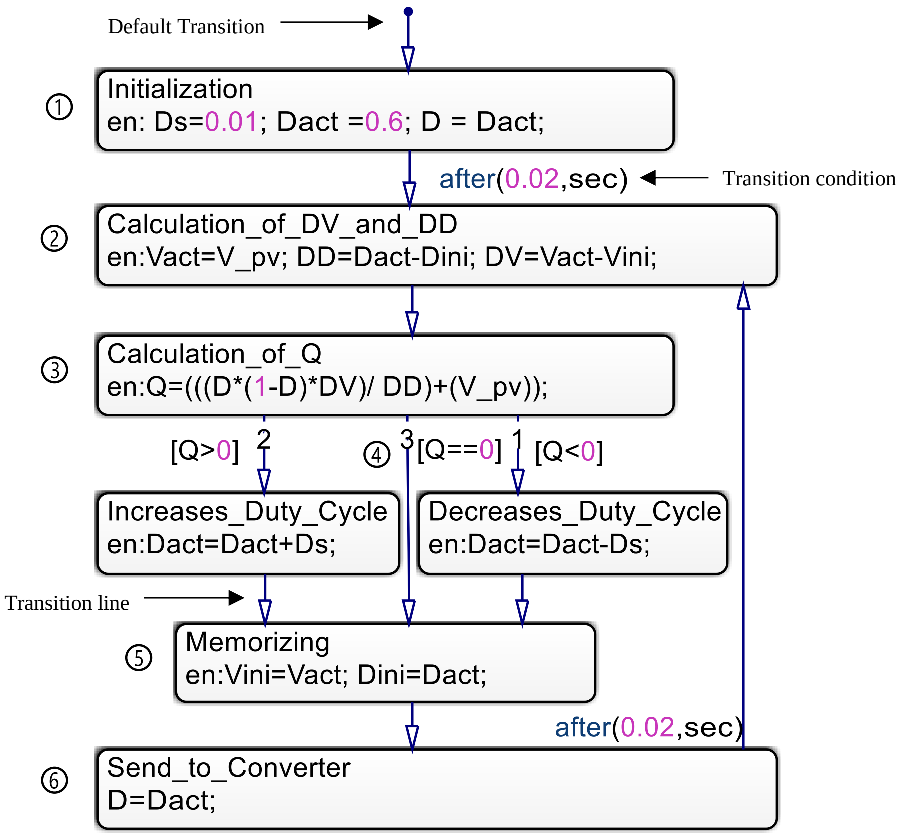

Figure III.6. Stateflow chart of the proposed CSL-MPPT algorithm.

III.4 Simulation of the proposed CSL-MPPT method

III.4.1 The test environment used for simulation

The simulation test of the proposed CSL-MPPT method is carried out under MATLAB/Simulink/Stateflow environment. The test workbench used for simulation is composed of the one-diode equivalent model of the PV panel, with specifications given in Table II.1. The latter is feeding a resistive load (R_L) through the buck-boost converter. The buck-boost is constructed to work in continuous conduction mode (CCM), with the next specifications: L=4 mH, C_1=3300 µF, and C_2=3300 µF, nominal output voltage V_{O_max} =30 V, efficiency of buck-boost converter is more than 92%, and switching frequency (f_s) equals to 20 kHz.

MPPT algorithms for PV systems are usually tested under the EN 50530 dynamic efficiency test [16], where the sharpest irradiance slope is 100 W/m^2/s (per second). Nevertheless, due to the expanding of the PV technology utilization in different projects such as car-mounted PV, and backpack PV, PV modules can be exposed to fast irradiance disturbance, i.e. up to 100 W/m^2/ms (per millisecond) [17]. Consequently, MPPT behavior is examined under very sharp irradiance variation, i.e. step waveform. The test profile used in the simulation is composed of three *P-V* curves applied successively in a time interval of 2 seconds. These three *P-V* curves are shown in Fig. III. 7(a). The curves 1, 2, and 3 are obtained by subjecting the PV panel to 900 W/m^2, 700 W/m^{2,} and 500 W/m^2, with MPP1 (17.36 V, 76.90 W), MPP2 (17.29 V, 59.50 W), and MPP3 (17.11 V, 41.90 W), and applied on the following time intervals in the test profile [0 s, 0.8 s], [0.8 s, 1.4 s], and [1.4 s, 2 s], respectively. The temperature is kept unchanged at 25° C throughout the testing period.

For further examination, MPPT behavior is examined also under temperature changing. The test profile used in the simulation is composed of three *P-V* curves applied successively in a time interval of 2 seconds. These three *P-V* curves are shown in Fig. III. 7(b). The curves 1, 2, and 3 are obtained by subjecting the PV panel to 25° C, 35° C, and 45° C, with MPP1 (17.3 V, 59.5 W), MPP2 (15.9 V, 54.5 W), and MPP3 (14.46 V, 49.6 W), and applied on the following time intervals in the test profile [0 s, 0.8 s], [0.8 s, 1.4 s], and [1.4 s, 2 s], respectively. The irradiance is kept unchanged at 700 W/m^2 throughout the testing period.

In the proposed method, MPPT sampling time T_S is 20 ms and the step size of duty cycle perturbation is 1%, i.e., $D_S = 0.01$.

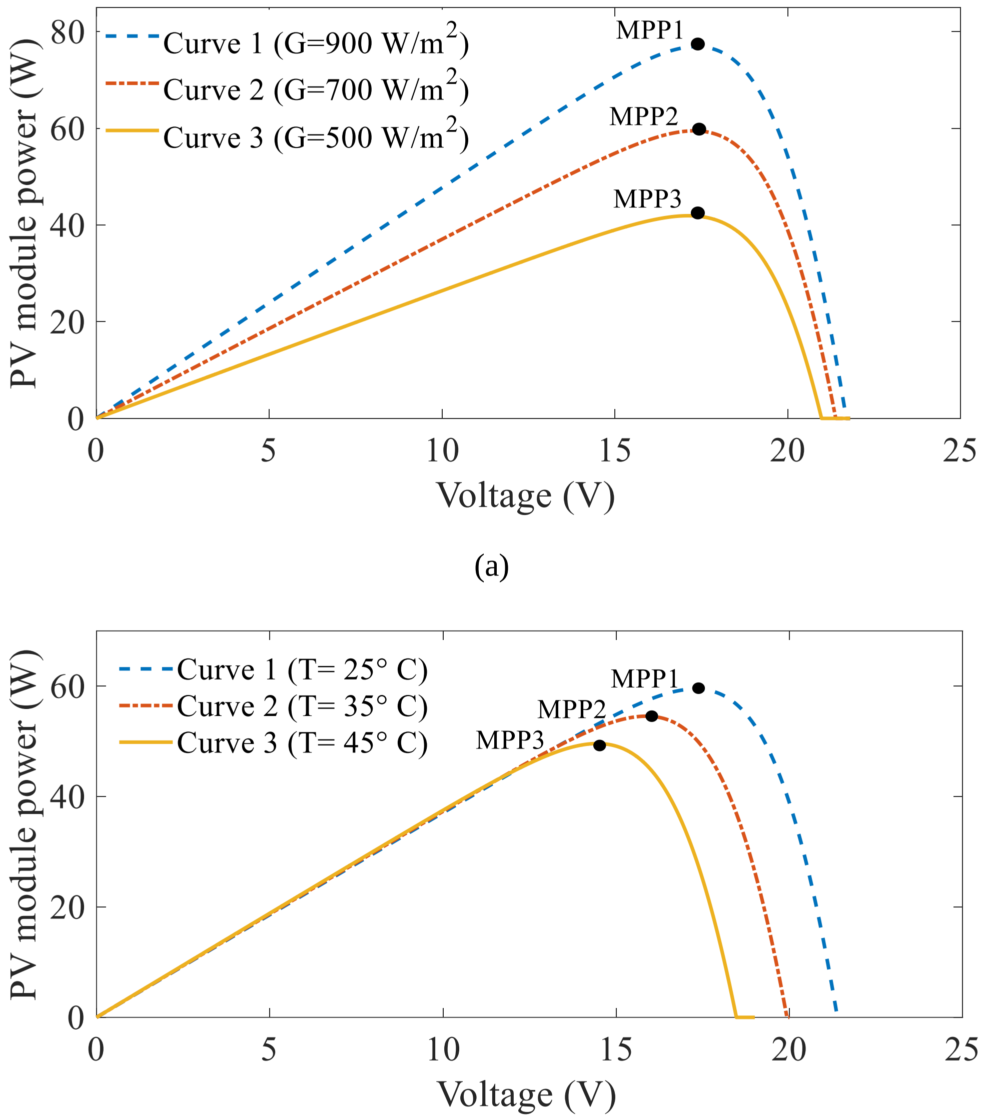

(a)

(b)

Figure III.7. *P-V* characteristics of the test profile: (a) *P-V* characteristics of the PV module under irradiance changing, and (b) *P-V* characteristics of the PV module under temperature change.

III.4.2 Results &discussion

The performance of the CSL-MPPT algorithm is compared with conventional P&O. Both MPPTs are examined under the test profile of three *P-V* curves mentioned earlier. For both algorithms, the waveforms of D, V_{PV}, and P_{PV}, are shown in Figs. III. 8(a), (b), and (c), respectively. At the beginning, MPP1 is tracked by both algorithms in less than 100 ms with similar tracking speed. MPP2 is tracked also within 80 ms, but this time CSL is a bit slower in tracking. The tracking of MPP3 has been successfully made by both algorithms with the same tracking speed. Consequently, both algorithms show almost similar tracking speed. In addition, the tracking efficiencies under this test profile are found equal to 98.82% for both algorithms. Hence, it can be concluded that the proposed CSL-MPPT has almost identical performance with the P&O.

Fig. III.9 shows a zoomed portion of the steady-state oscillation around the MPP using the CSL algorithm. The power versus time is shown in Fig. III. 9(a) where the peak-to-peak power oscillation is confined within 1.7 W. The three-level operation of D is shown in Fig. III. 9(b) where D oscillates around the optimal duty cycle value (D_{opt}) between three points: $A=D_{opt} - D_S$, $B=D_{opt}$, and $C=D_{opt} + D_S$. Fig. III.9(c) shows the duty cycle variation with respect to time.

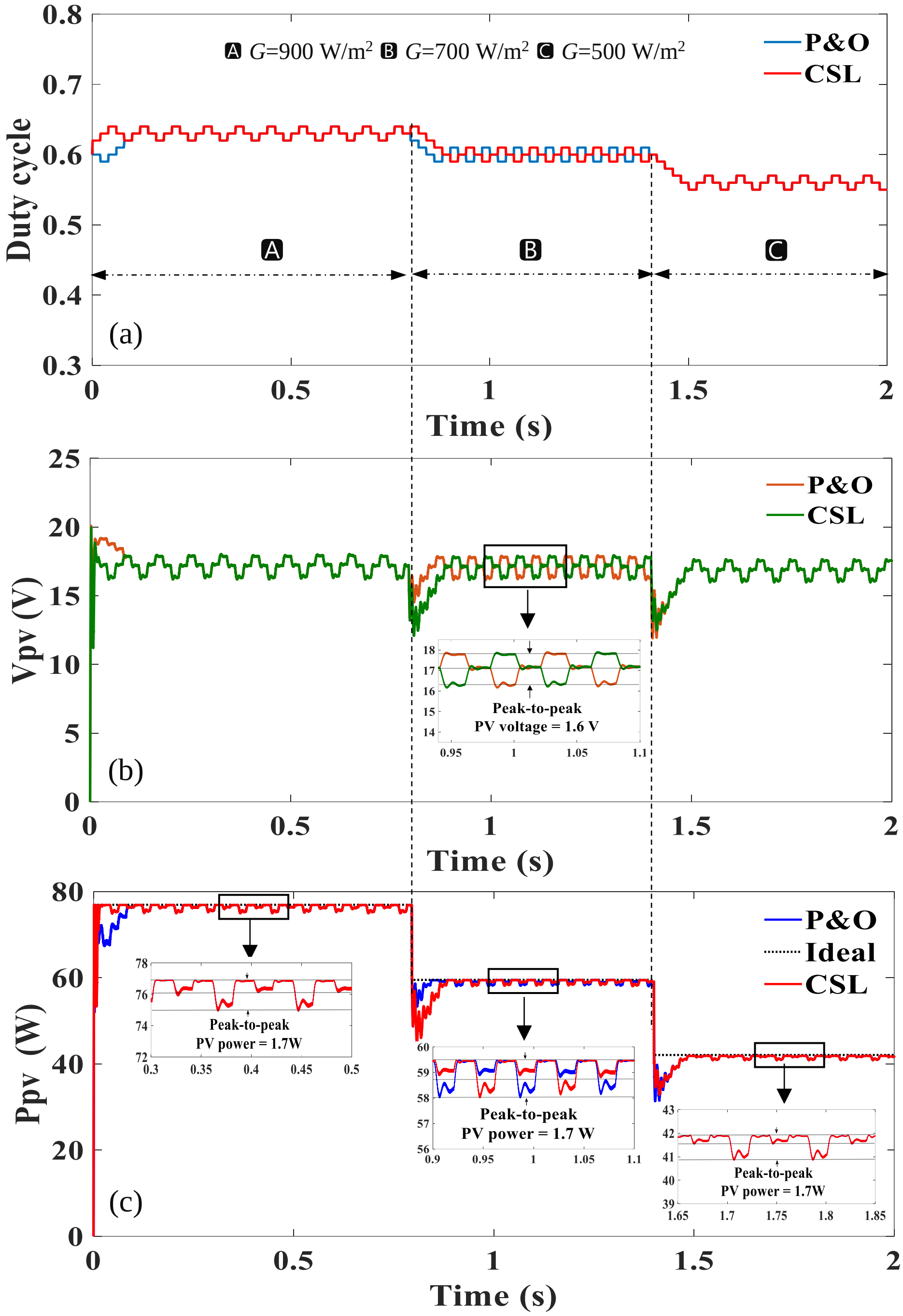

Figure III.8. Simulation result of tracking waveforms for both P&O-MPPT and CSL-MPPT Algorithms: (a) Duty cycle, (b) PV module voltage, and (c) PV module power.

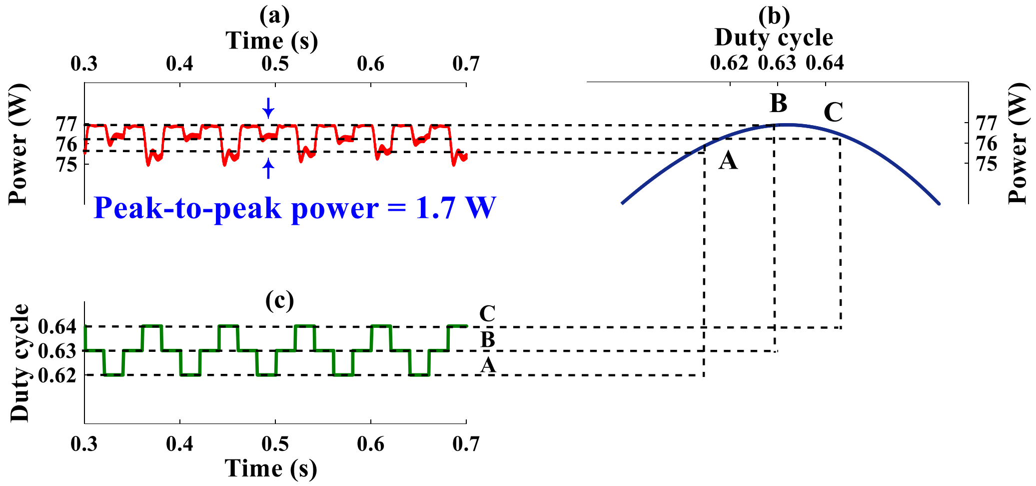

Figure III.9. Steady-state oscillation around the MPP using the CSL algorithm with three-level operation: (a) Power versus time, (b) PV power versus duty cycle, and (c) Duty cycle versus time.

The variation of Q is shown in Fig. III.10. When the MPP is tracked, Q oscillates around zero during the steady-state regime, it is pulled away from the zero during the search for new MPP (for MPP2 at 0.8 s, and MPP3 at 1.4 s).

A zoomed portion of the variation of Q together with D at the steady-state regime is shown in Fig. III.11, where the dynamic behavior of the model is considered in the simulation. As it can be seen in Fig. III.11, the oscillation of Q is irregular due to the inherent ripple of the pseudo-periodic step responses of the input capacitor voltage when the duty cycle is perturbed by the MPPT. Although Q can be easily influenced by this ripple, the tracking capability will not be influenced as long as the duty cycle step-size is chosen large enough to guarantee the correct measurement of the sign of Q. On the other hand, Fig. III.12 shows the variation of Q in the ideal case without considering the noise and the ripple of the input capacitor i.e., the operation in the Q-D characteristics reached directly the final value. It can be seen that Q is oscillating around fixed points during the steady-state.

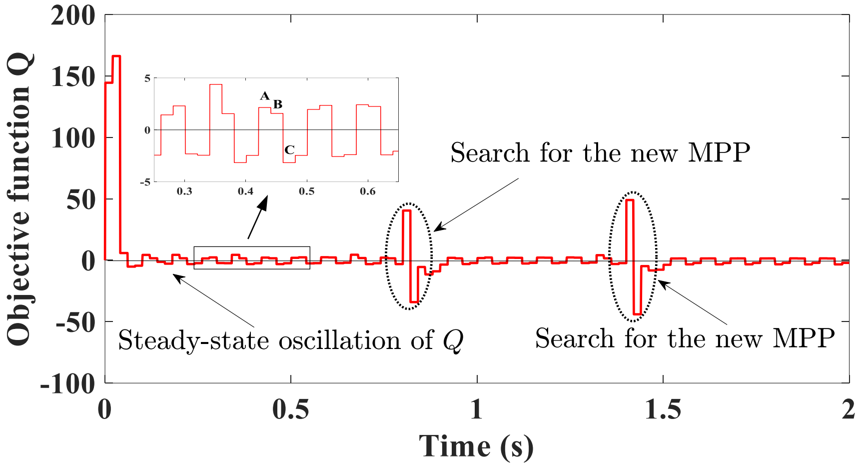

Figure III.10. Oscillation of Q around zero during MPP tracking.

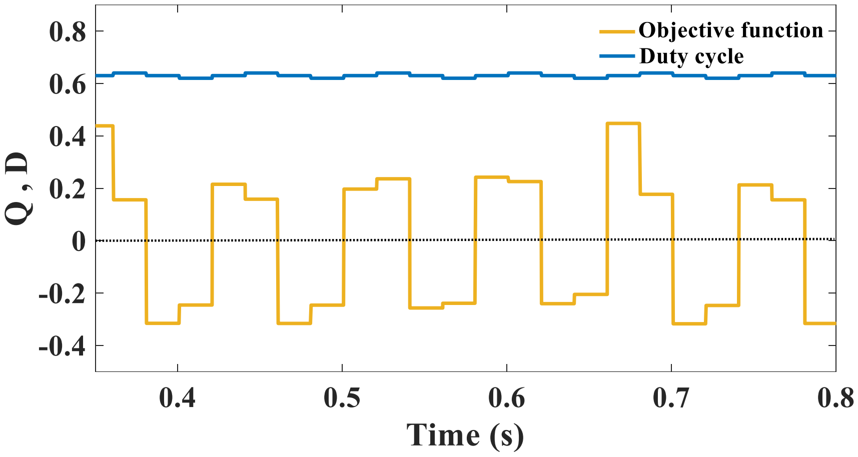

Figure III.11. Zoomed portion of Q oscillation considering the dynamics of the system.

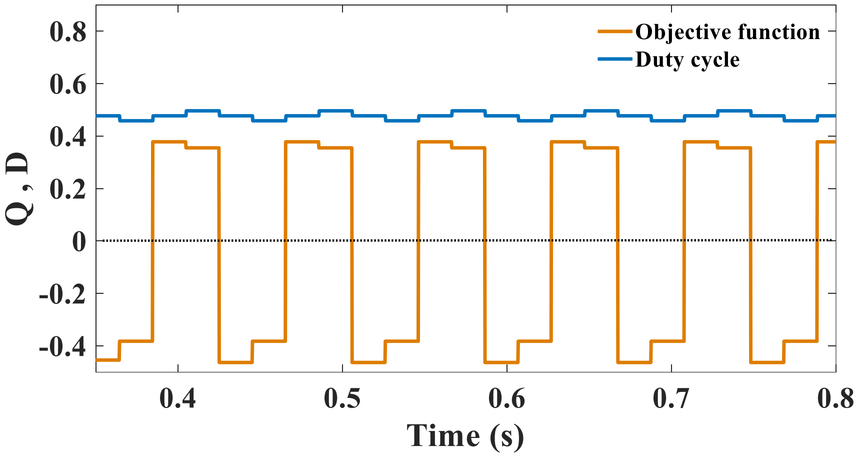

Figure III.12. Zoomed portion of the oscillation of Q using the ideal model.

For the load disturbance, the tracking performance of the CSL-MPPT algorithm is examined under variation of the load and compared with P&O algorithm, where a step-change in load is introduced at t = 0.8 s from 10 to 5 Ω. Then, it is stepped up to 10 Ω again at t = 1.4 s. The waveforms of D, V_{PV}, and P_{PV}, are shown in Figs. III. 13(a), (b), and (c), respectively. At the beginning, the MPP1 is tracked in less than 60 ms by proposed CSL-MPPT. Then, the MPP2 and MPPT3 are tracked within 180 ms. Consequently, the power is rapidly restored after a brief dip when the load change takes place. It can be concluded that, the tracking performance of the proposed CSL-MPPT is able to track the MPP under load disturbance effectively. Additionally, it has almost similar tracking speed to the P&O algorithm.

For further illustration of the accuracy of the proposed CSL-MPPT algorithm, its tracking performance is examined under temperature changes and compared with the P&O algorithm, where a step-change in the temperature is introduced at t = 0.8 s from 25° C to 35° C. Then, it is stepped up to 45° C again at t = 1.4 s. For this test, the irradiance level was fixed at 700 W/m^2 and 10 Ω for the load. The waveforms of D, V_{PV}, and P_{PV}, are shown in Figs. III. 14(a), (b), and (c), respectively. As expected, the proposed CSL-MPPT has effectively tracked the MPP of each temperature-changing level almost similar to the tracking performance of the P&O algorithm.

For more clarification, Fig. III.15 shows a zoomed portion of the tracking performance of CSL-MPPT of the PV-buck-boost converter system under variation of the load from 5 Ω to 10 Ω with fixed irradiance at 900 W/m^2. It can be seen, that the power versus time is shown in Fig. III. 15(a) where the perturbation steps of the tracking to new MPP are illustrated in Fig. III. 15(b). The increments of duty cycle operation are shown in Fig. III. 15(c) where the algorithm needs seven successive increments of duty cycle to reach the new MPP. Furthermore, the objective function versus time is shown in Fig. III. 15(d) where the perturbation steps to annul the objective function, which corresponds to tracking new MPP are illustrated in Fig. III. 15(e).

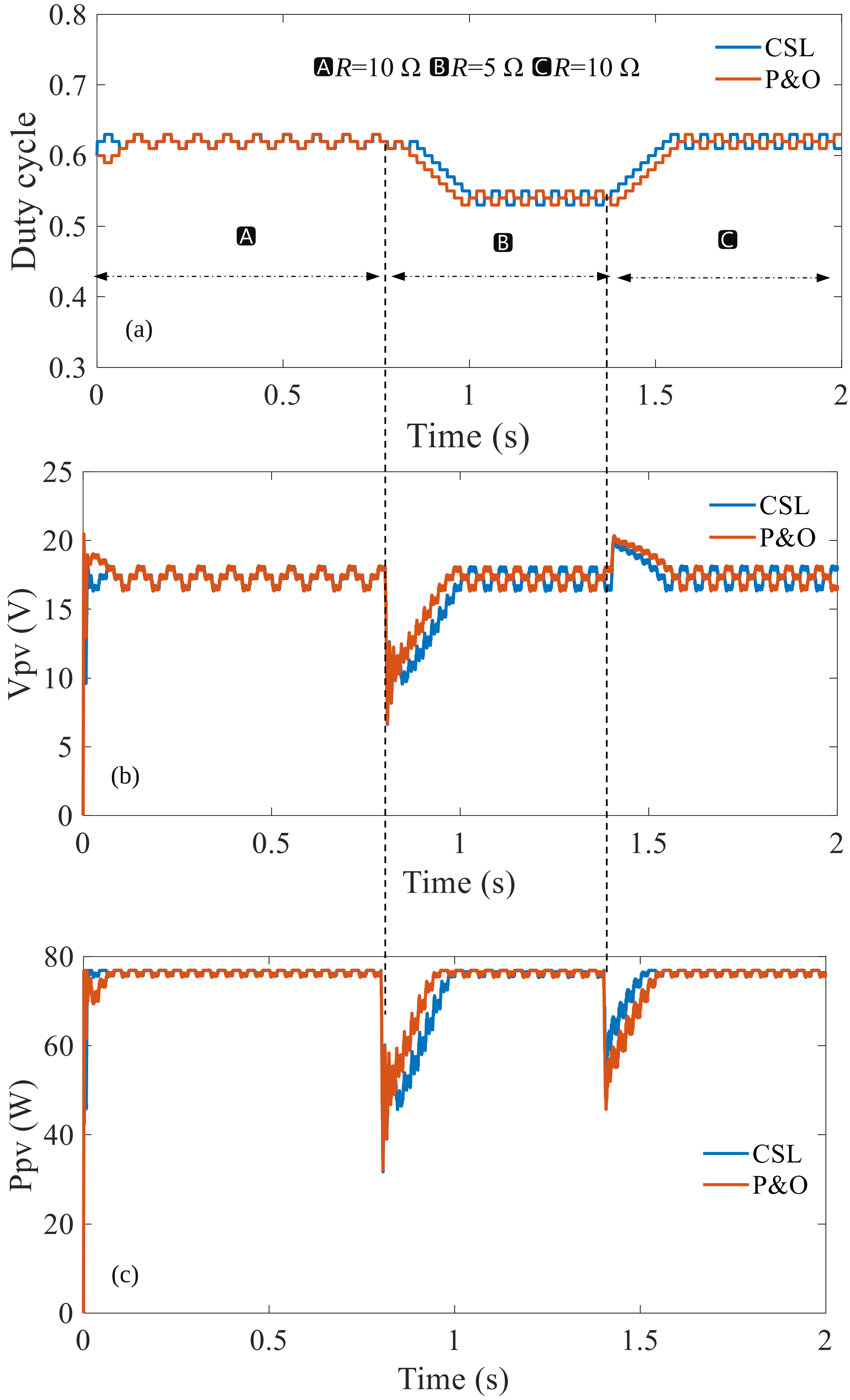

Figure III.13. Simulation result of tracking waveforms for proposed CSL and P&O under load disturbance from 10 Ω to 5 Ω, then from 5 Ω to 10 Ω with fixed irradiance at 900 W/m^2: (a) Duty cycle versus time, (b) PV module voltage versus time, and (c) PV module power versus time.

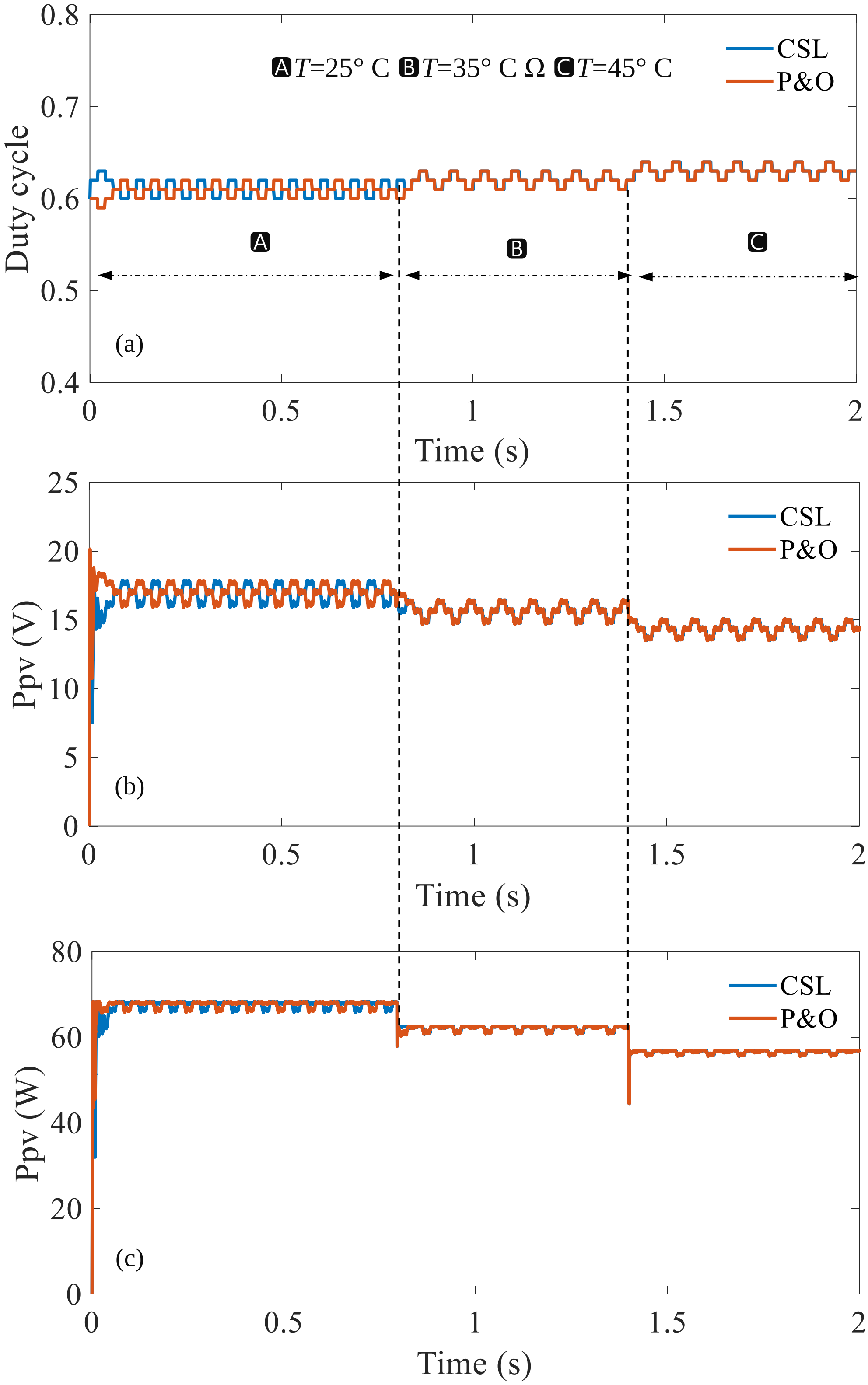

Figure III.14. Simulation result of tracking waveforms for proposed CSL and P&O under temperature changing from 25° C to 35° C, then from 35° C to 45° C with fixed irradiance at 700 W/m^2 and 10 Ω for the load : (a) Duty cycle versus time, (b) PV module voltage versus time, and (c) PV module power versus time.

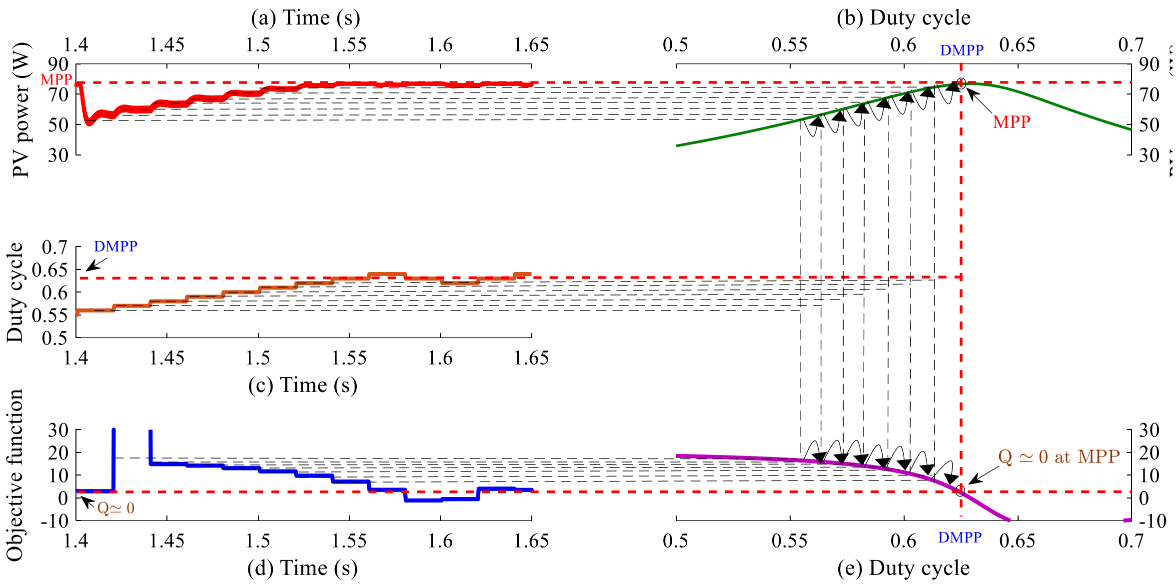

Figure III.15. Tracking performance of CSL-MPPT of the PV-buck-boost converter system under variation of the load from 5 Ω to 10 Ω with fixed irradiance at 900 W/m^2: (a) Power versus time, (b) PV power versus duty cycle, and (c) Duty cycle versus time, (d) Objective function versus time, and (e) Objective function versus duty cycle.

III.5 Hardware validation

III.5.1 Experimental set-up

The efficiency of the suggested CSL-MPPT is verified experimentally using the hardware test bench shown in Fig. III.16. The latter is composed of an Agilent PV array simulator (E4360A Modular SAS) used to emulate the electrical behavior of PV modules/arrays using DC voltage controlled-current source. The simulator is feeding a variable resistive load through a low power buck-boost converter (100 W) and the nominal output voltage V_{O_max} =30 V with the following specifications: L= 4 mH, C_1 = 3300 µF, and C_2 = 3300 µF, working under a switching frequency of f_s = 20 kHz. The LEM LV-25P hall-effect sensor is utilized to sense the PV module voltage and transmit the calibrated feedback signal (within the range 0 V-3.3 V) to the Arduino DUE board. Besides, the gate drive circuit based on the HCPL3120 IC driver and an isolated power supply are used to control the MOSFET power switch.

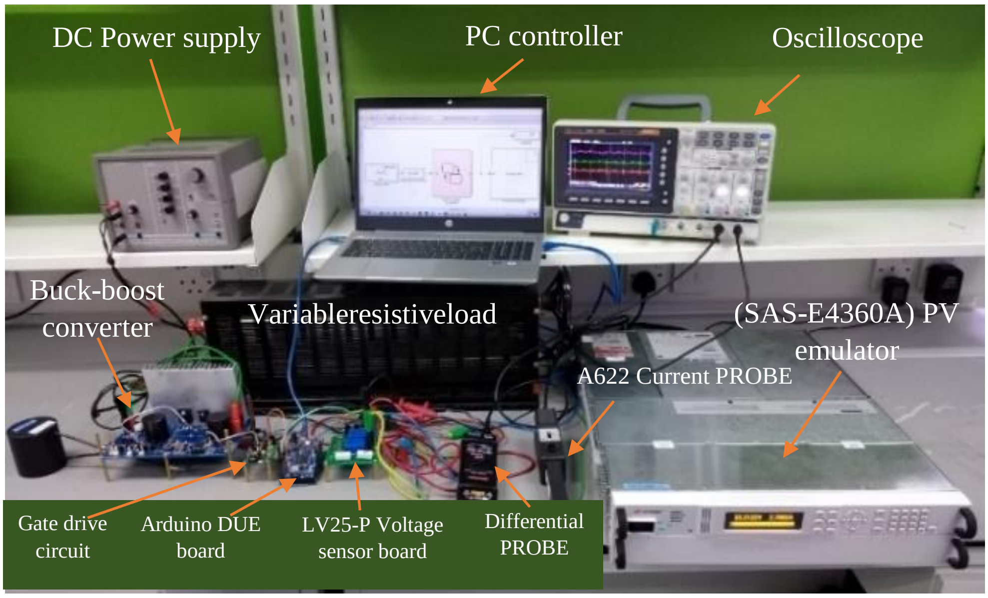

Figure III.16. Hardware set-up used for the experimental verification.

The Arduino DUE board is utilized as a target hardware for the CSL-MPPT controller developed under MATLAB/ Simulink/Stateflow environment. The support package of Matlab/Simulink for Arduino is utilized to transform the CSL controller into an Arduino-compatible C code, which is again compiled and loaded to the SAM3X8E microcontroller of the Arduino DUE. Fig. III.17 shows the model-based CSL controller compiled and loaded to the Arduino DUE using the Simulink support package for Arduino hardware [18]. During real-time operation, the numerical voltage value is transmitted to the CSL Stateflow chart (Explained earlier in *Section III.3.2*) through a dedicated read block for Arduino hardware wherein the input pin (ADC channel) of the sensed signal can be assigned.

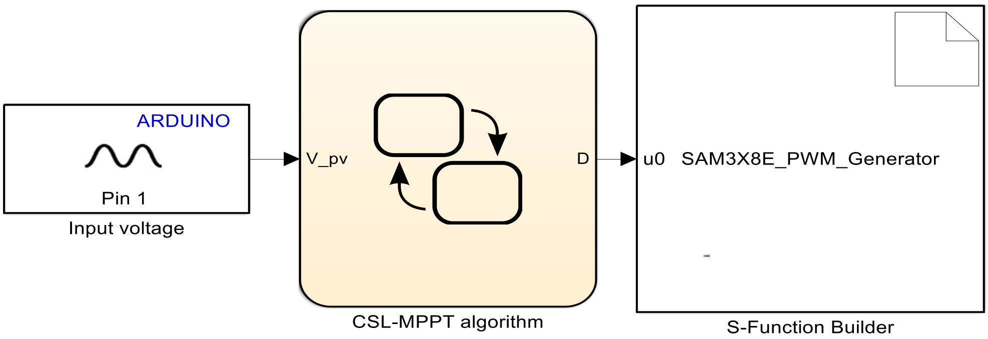

Figure III.17. Simulink model of CSL controller loaded to the target hardware.

The PWM module of the SAM3X8E microcontroller integrates eight separate channels, each one can generate two complementary outputs [19]. The characteristics of the output waveforms such as frequency, duty cycle, and polarity, can be configured through the dedicated control registers using assembly code. For this purpose, the S-function builder block is used to configure the PWM module and to generate the PWM signal according to the computed duty cycle value by the CSL Stateflow chart. The assembly code implemented through the S-function that is shown in Fig. III.18. The PWM module configuration can be summarized in the following steps:

Multiplexing the parallel input/output of port C (PIOC) with PWM channel 6 output: The register REG_PIOC_PDR is used to disable PIOC; then, REG_PIOC_ABSR register is used to assign the PIOC to peripheral A or B; after that, the PIOC is enabled again by using REG_PIOC_OER.

Switching frequency configuration: the channel mode register REG_PWM_CMR6 is used to set the required clock of channel 6 and the characteristics of the output waveforms. Then, the value of REG_PWM_CPRD6 is calculated such that the required frequency can be accurately generated, i.e., to get 20 kHz switching frequency, since the master clock (84MHz) is selected, the value of REG_PWM_CPRD6 is obtained as follows: 84MHz/20KHz=4200.

Updating the duty cycle value: the updating value of the duty cycle is configured through the REG_PWM_CDTY6 register as follows: REG_PWM_CDTY6=u0[0]×REG_PWM_CPRD6where u0[0] contains the computed duty cycle value obtained from the Stateflow of CSL-MPPT algorithm [19].

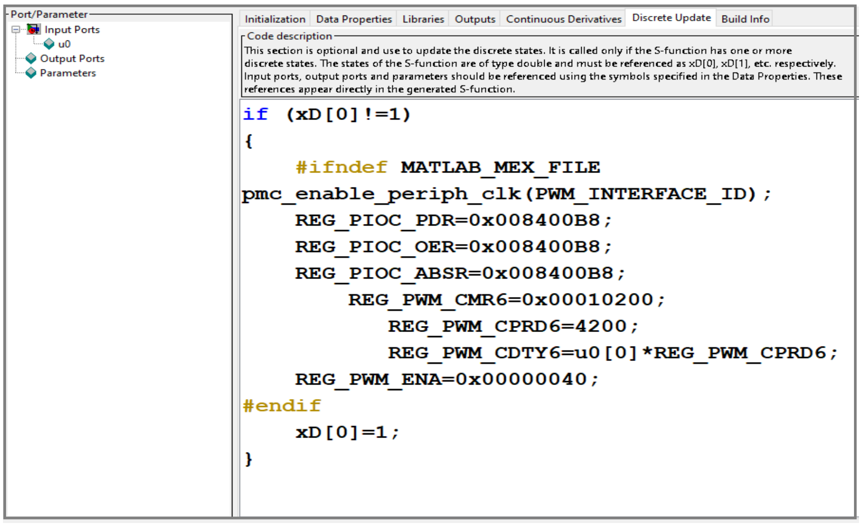

This section is optional and use to update the discrete states. It is called only if the S-function has one or more discrete states. The states of the S-function are of type double and must be referenced as xD[0], xD[1], etc. respectively. Input ports, output ports and parameters should be referenced using the symbols specified in the Data Properties. These references appear directly in the generated S-function.

```
if (xD[0]!=1)
{
    #ifndef MATLAB_MEX_FILE
pmc_enable_periph_clk(PWM_INTERFACE_ID);
    REG_PIOC_PDR=0x008400B8;
    REG_PIOC_OER=0x008400B8;
    REG_PIOC_ABSR=0x008400B8;
        REG_PWM_CMR6=0x00010200;
           REG_PWM_CPRD6=4200;
           REG_PWM_CDTY6=u0[0]*REG_PWM_CPRD6;
    REG_PWM_ENA=0x00000040;
#endif
    xD[0]=1;
}
```

Figure III.18. Utilization of S-function builder to configure the PWM module using assembly code.

III.5.2 Experimental results & discussion

The CSL-MPPT and P&O-MPPT methods are experimentally evaluated under the same operating condition with T_S = 200 ms, and D_S = 0.02. The tracking process is re-initialized every 15 min to avoid fault occurrence and software errors. Further, the tracking capability of the proposed CSL algorithm is proven under variable irradiance change and load disturbance.

III.5.2.1 Experimental validation under irradiance change test:

The transient state of the test profile is initialized the irradiance at 900 W/m^2, then stepped to 700 W/m^2 at t = 7 s, and stepped to 500 W/m^2 at t = 14 s, the results are shown in Fig. III.19. The voltage, current, and power oscillograms for both CSL and P&O algorithms are shown in Figs. III.19 (a) and (b), respectively. In addition, a zoomed portion of steady-state oscillation of voltage, current, and power of the CSL algorithm are shown in Fig. III.19 (c). As regards the tracking speed, both CSL and P&O can track MPP in less than 750 ms. Similar to the simulation finding, both algorithms have almost similar performance.

Table III.3 presents a comparison between the proposed CSL and conventional P&O algorithms from all aspects. From this table, it can be seen that both CSL and P&O have similar tracking performance. The CSL outperforms the P&O in terms of computational requirements are shown in Fig. III.20, where the computational burden and the sensors cost of implementation are decreased by 24.3%, and 27.95%, respectively. As can be seen in Table III.3, the computation time required by the P&O is higher than that required by the CSL algorithm. This is because the P&O needs two ADC for the current and voltage signals conversions, while the proposed CSL uses only one ADC for the voltage signal conversion.

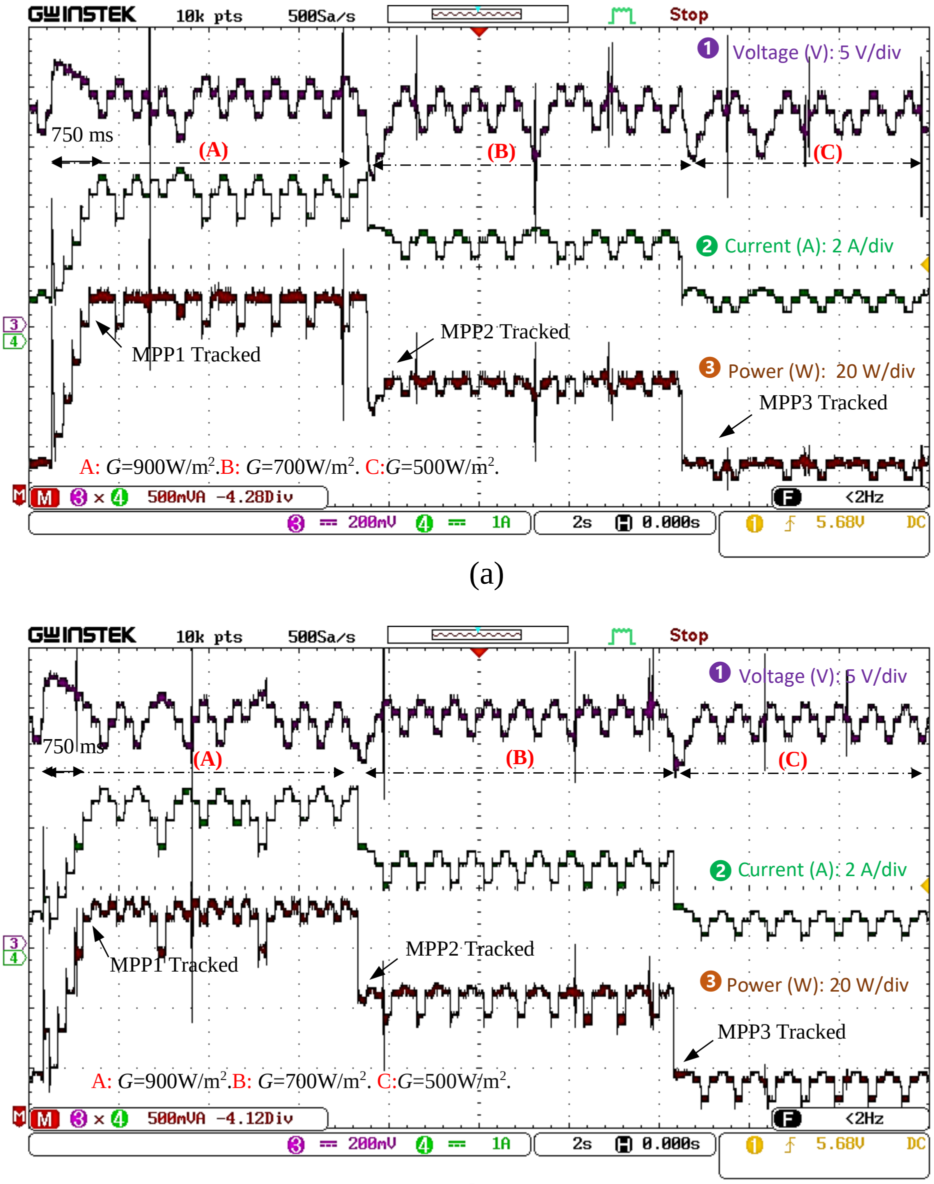

(a)

(b)

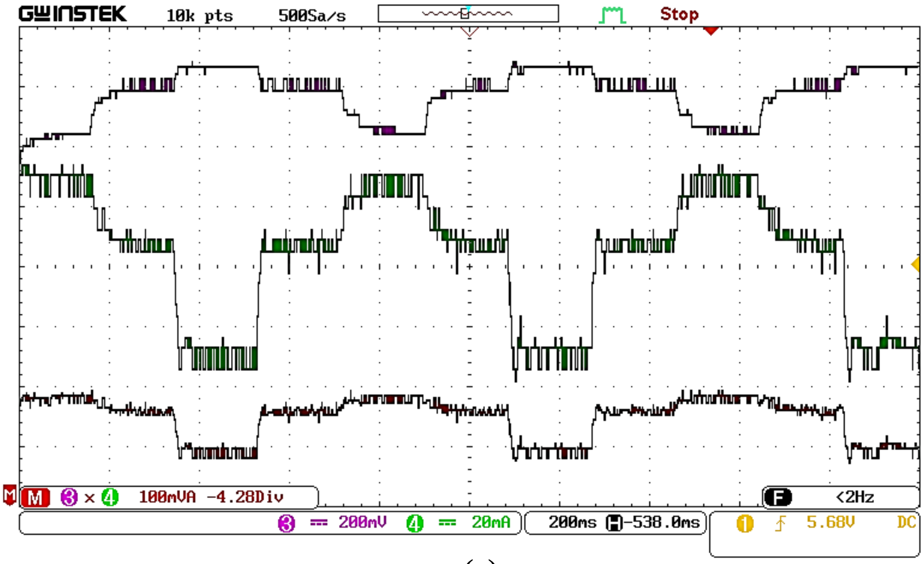

(c)

Figure III.19. Tracking performance under irradiance changes: (a) experimental waveforms of CSL-MPPT, (b) experimental waveforms of the P&O-MPPT, and (c) zoom portion of the three-level operation of the CSL-MPPT.

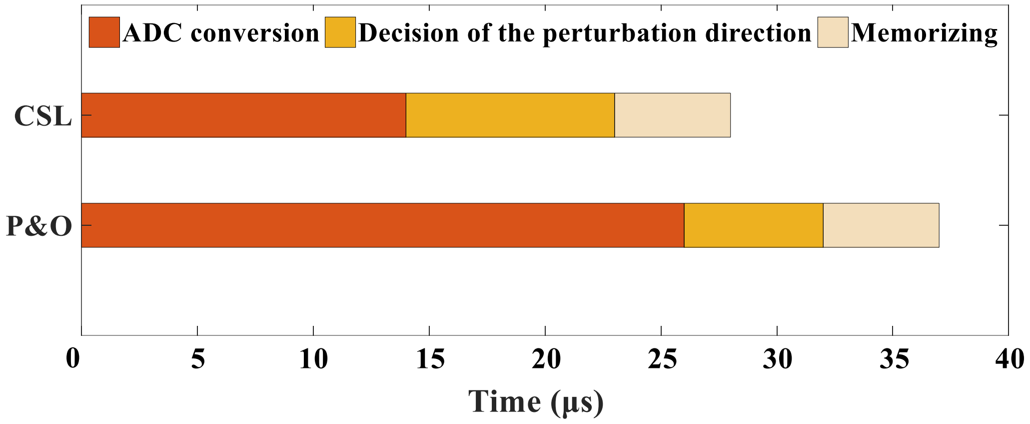

Figure III.20. Comparison of the computation time required by the CSL and P&O algorithms.

Table III.3. Performance Comparison Between the Proposed CSL and Conventional P&O Algorithm

Algorithm	Ripple in Power	Convergence Time	Efficiency	Computation Time	Sensors [20, 21] (Cost)
P&O	7.5 W	750 ms	98.4%	37 µs	Voltage and current (104.27 $)
CSL	7.5 W	750 ms	98.4%	28 µs	Voltage (75.13 $)

III.5.2.2 Experimental validation in presence of load disturbances:

To examine the influence of load changes on the performance of the proposed CSL-MPPT a step-change in load for CSL-MPPT is introduced at t = 7 s from 10 to 5 Ω. Then, it is stepped up to 10 Ω again at t = 15 s. The experimental results of the waveforms are displayed in Fig. III.21. As can be observed from these waveforms, the effect of the load change on the tracking performance of the CSL-MPPT is almost negligible; the power is rapidly restored after a brief dip when the load change takes place.

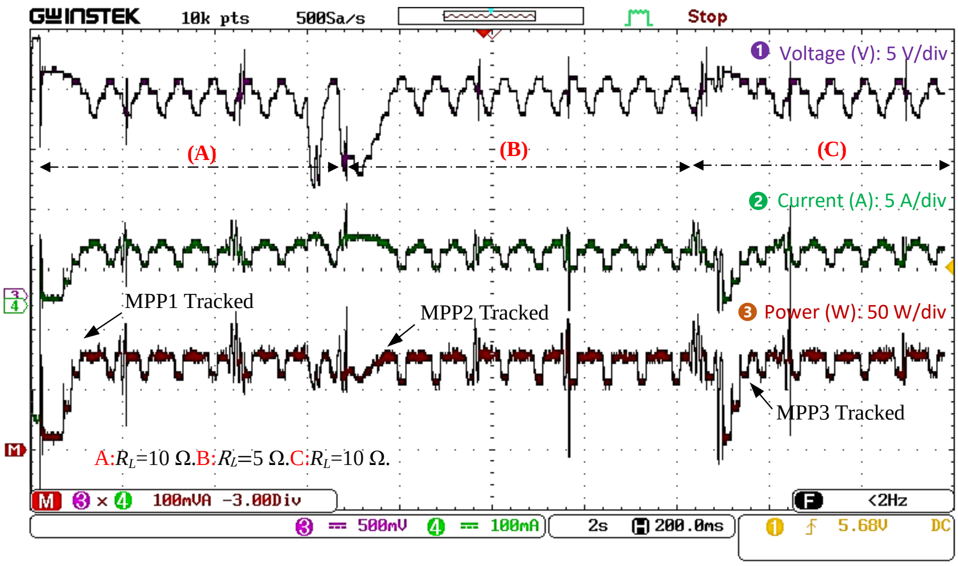

Figure III.21. Experimental waveforms of the CSL-MPPT in presence of the load disturbances.

III.6 Conclusion

This paper presents a current sensorless maximum power point tracking algorithm for PV systems implemented using Arduino DUE microcontroller. The proposed method is dependent on the buck-boost converter, where a predefined objective function derived from its mathematical model is used for its implementation. A comparative evaluation of the proposed method and conventional P&O algorithm has been carried out under Matlab/Simulink/Stateflow environment. Additionally, an experimental test has been carried out to validate the simulation where the Simulink support package for Arduino hardware was used to generate the code for the microcontroller. The reduction percentage of the total cost and the computation burden were 27.95%, and 24.3%, respectively. The proposed current sensorless scheme could be extended to deal with partial shading conditions.

III.7 References

[1] L. Achour, M. Bouharkat, O. Assas, and O. J. E. Behar, "Hybrid model for estimating monthly global solar radiation for the Southern of Algeria:(Case study: Tamanrasset, Algeria)," vol. 135, pp. 526-539, 2017.

[2] T. Kok Soon, S. Mekhilef, A. J. j. o. r. Safari, and s. energy, "Simple and low cost incremental conductance maximum power point tracking using buck-boost converter," vol. 5, no. 2, p. 023106, 2013.

[3] M. Fannakh, M. L. Elhafyani, and S. J. I. R. P. G. Zouggar, "Hardware implementation of the fuzzy logic MPPT in an Arduino card using a Simulink support package for PV application," vol. 13, no. 3, pp. 510-518, 2019.

[4] M. Killi and S. J. I. T. o. I. E. Samanta, "An adaptive voltage-sensor-based MPPT for photovoltaic systems with SEPIC converter including steady-state and drift analysis," vol. 62, no. 12, pp. 7609-7619, 2015.

[5] S. Motahhir, A. Chalh, A. El Ghzizal, and A. J. J. o. C. p. Derouich, "Development of a low-cost PV system using an improved INC algorithm and a PV panel Proteus model," vol. 204, pp. 355-365, 2018.

[6] M. Killi, S. J. I. J. o. E. Samanta, and S. T. i. P. Electronics, "Voltage-sensor-based MPPT for stand-alone PV systems through voltage reference control," vol. 7, no. 2, pp. 1399-1407, 2018.

[7] M. Kermadi, S. Mekhilef, Z. Salam, J. Ahmed, and E. M. J. I. T. o. E. E. S. Berkouk, "Assessment of maximum power point trackers performance using direct and indirect control methods," vol. 30, no. 10, p. e12565, 2020.

[8] M. Kermadi, E. M. J. R. Berkouk, and S. E. Reviews, "Artificial intelligence-based maximum power point tracking controllers for Photovoltaic systems: Comparative study," vol. 69, pp. 369-386, 2017.

[9] K. Ishaque, Z. Salam, A. Shamsudin, and M. J. A. E. Amjad, "A direct control based maximum power point tracking method for photovoltaic system under partial shading conditions using particle swarm optimization algorithm," vol. 99, pp. 414-422, 2012.

[10] M. Kermadi, Z. Salam, J. Ahmed, and E. M. J. I. T. o. I. E. Berkouk, "An effective hybrid maximum power point tracker of photovoltaic arrays for complex partial shading conditions," vol. 66, no. 9, pp. 6990-7000, 2018.

[11] A. Loukriz, M. Haddadi, and S. J. I. t. Messalti, "Simulation and experimental design of a new advanced variable step size Incremental Conductance MPPT algorithm for PV systems," vol. 62, pp. 30-38, 2016.

[12] N. Dasgupta, A. Pandey, A. K. J. S. e. m. Mukerjee, and s. cells, "Voltage-sensing-based photovoltaic MPPT with improved tracking and drift avoidance capabilities," vol. 92, no. 12, pp. 1552-1558, 2008.

[13] A. Harrag, S. Messalti, and Y. Daili, "Innovative single sensor neural network PV MPPT," in 2019 6th International Conference on Control, Decision and Information Technologies (CoDIT), 2019, pp. 1895-1899: IEEE.

[14] J.-J. E. Slotine and W. Li, Applied nonlinear control (no. 1). Prentice hall Englewood Cliffs, NJ, 1991.

[15] M. Kermadi, Z. Salam, and E. M. Berkouk, "A rule-based power management controller using stateflow for grid-connected PV-battery energy system supplying household load," in 2018 9th IEEE International Symposium on Power Electronics for Distributed Generation Systems (PEDG), 2018, pp. 1-6: IEEE.

[16] R. Bründlinger, N. Henze, H. Häberlin, B. Burger, A. Bergmann, and F. Baumgartner, "prEN 50530–The new European standard for performance characterisation of PV inverters," in 24th EU PV Conf., Hamburg, Germany, 2009: WIP-Renewable Energies Munich.

[17] I. G. Zurbriggen and M. J. I. T. o. I. E. Ordonez, "PV energy harvesting under extremely fast changing irradiance: State-plane direct MPPT," vol. 66, no. 3, pp. 1852-1861, 2018.

[18] Simulink Support Package for Arduino Hardware (https://www.mathworks.com/matlabcentral/fileexchange/40312-simulink-support-package-for-arduino-hardware), accessed on 7 September 2022.

[19] Atmel. SAM3X/SAM3A Series Datasheet; Atmel Corporation: San Jose, CA, USA, 2015; p. 1459., Arduino Due.

[20] L. I. SA;. LEM voltage sensor LV 25-P (https://www.lem.com/sites/default/files/products_datasheets/lv_25-p.pdf) [Online].

[21] L. I. SA. LEM current sensor LA 25-NP (https://www.lem.com/sites/default/files/products_datasheets/la%2025-np%20sp25.pdf) [Online].

CHAPTER IV

MODIFIED CURRENT SENSORLESS APPROACH FOR MAXIMUM POWER POINT TRACKING OF PARTIALLY SHADED PHOTOVOLTAIC SYSTEMS

IV.1 Introduction

Photovoltaic (PV) is one of the clean and sustainable energies that are considered the most promising solutions in renewable energy due to its environmentally-friendly property, limitless availability, lower maintenance costs, and silent working mode [1-4]. However, the main challenge in PV systems is that the electrical behaviors are non-linear in nature and change with environmental effects, such as sunlight irradiance and temperature. For this reason, the control of PV system requires a specific method to extract the maximum power point (MPP) from the PV source. In the past decades, several MPP tracking (MPPT) methods have been established to enhance the efficiency of photovoltaic systems. There was in fact, broad agreement that it is necessary to identify the global maximum power point (GMPP) when multiple peaks characterize the power-voltage (*P*-*V*) curve under partial shading conditions (PSCs).

Modified conventional MPPT techniques are less complex and efficient in GMPP tracking. Some typical examples of this are proposed in [5,6], where authors introduced novel MPPT approaches based on the $0.8\times V_{oc\_mod}$ model (V_{oc_mod} is the open-circuit voltage of a PV module) by exploiting the ability of $0.8\times V_{oc\_mod}$ model to assume that the peaks of a PV string are located nearly at the multiples of $0.8\times V_{oc\_mod}$. Fig. IV.1 shows the *P*-*V* characteristics of a PV array under three patterns. For these patterns, it can be seen that the local MPP (LMPP) region is confined within the $[D_{k,min}, D_{k,max}]$ interval, where D_{min} and D_{max} are, respectively, the lower and upper duty cycle (D) limits at every region k.

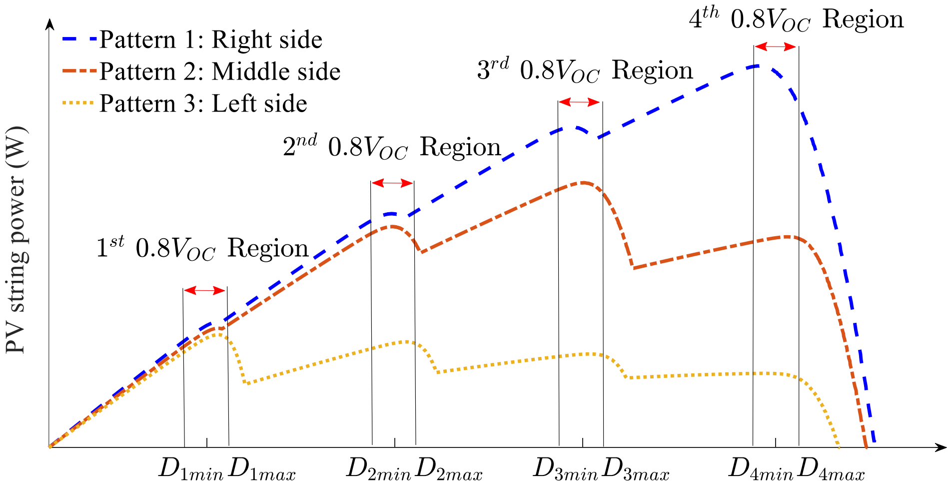

Figure IV.1. Three *P*-*V* patterns of a PV string composed of four modules, where MPP of each region (i.e., 1st, 2nd, 3rd, and 4th) is confined within the $k\times0.8V_{oc\_mod}$ region.

Nevertheless, the perturbative MPPT methods are still requiring more information on both sensed voltage and current to perturb the operating point towards the correct direction.

Even though the operating region of the buck-boost converter is the full *I-V* plane regardless of the load value [7], there is no attempt yet made to propose a current sensorless MPPT method using buck-boost converter to deal with PSCs. Hence, this work proposes a modified current sensorless MPPT (MCSL-MPPT) method to track GMPP under partial shading conditions with many features leading to enhance its efficiency. First, a simple and low-cost method without a current sensor is established to implement GMPPT using a buck-boost converter. Second, a direct MPPT control approach with defined lower and upper duty cycle limits for each LMPP with adaptive step-size gain is introduced to make the tracking process rapid so that it can climb the neighboring peak faster while keeping steady-state oscillation low. Third, the computational burden is reduced, since the proposed algorithm requires only one ADC conversion, unlike conventional methods, which require two ADC conversions to track the GMPP.

The rest of this chapter is organized as follows: Section 2 describes the details of the proposed MCSL-MPPT approach, which is established based on the steps to be followed deriving the objective function from the mathematical model of buck-boost converter. Section 3 presents the experimental results of the proposed method, which shows its capability of tracking the GMPP effectively and, thus, remarkably guarantees convergence even under partial shading patterns. Finally, Section 4 outlines the conclusions.

IV.2. Methodology

IV.2.1 TheproposedMPPT scheme

IV.2.1.1 Direct control scheme

The proposed MCSL-MPPT is shown in Fig. IV.2. The structure diagram under study is established based on direct control scheme since the MPPT is achieved using the information of the voltage sensor only. In this approach, the duty cycle update is generated directly from the objective function i.e., *Q-D* curve without requiring any control loop [8,9]. The power conversion between the source (PV string) and the load (resistive load) is achieved by involving a DC-DC converter type buck-boost. The buck-boost converter is chosen due to its capability to operate as a step-up/step-down converter as well as its operating in full range of the *I-V* characteristics plane. The direct control scheme reduces the hierarchy process of the control approach and eliminates the need of current sensor. The latter has a lower computational burden since only one ADC conversion is required. In addition to that, the tuning gain of PI parameters is not required in this approach.

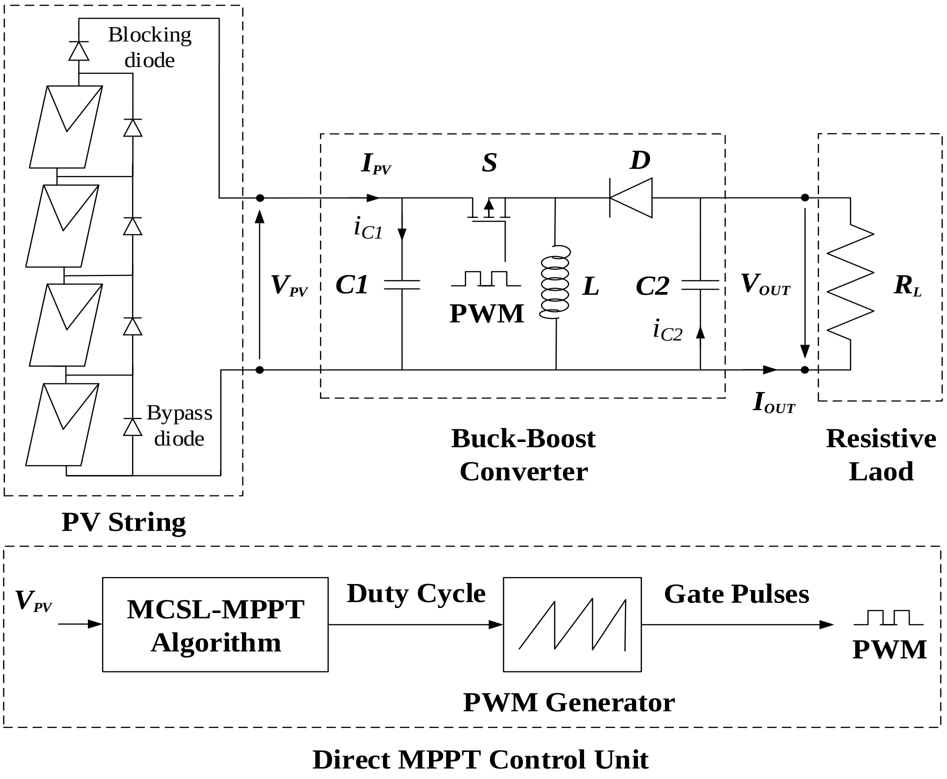

Figure IV.2. Structure diagram of the PV system under study and its associated MPPT control unit.

IV.2.1.2 Efficient MPPT search based on the objective function and duty cycle

As revealed in the proposed approach, the multiple peaks; P_{MPP1}, P_{MPP2}, P_{MPP3}, and P_{MPP4}, exist within optimal duty cycles (D_{MPP})i.e., D_{MPP1}, D_{MPP2}, D_{MPP3}, and D_{MPP4}. Respectively. Thus, these duty cycles operate with the optimal voltages (V_{MPP}) i.e., V_{MPP1}, V_{MPP2}, V_{MPP3}, and V_{MPP4}, respectively [5].

Significantly, the necessity to operate duty cycle in optimal voltages is to guarantee the operating point of Q mentione in Eq. (II.48) to be in the optimal region, which allows avoiding the duty cycle section that does not contain MPP. The establishment steps of duty cycle are studied for GMPP tracking according to [8]. In the proposed approach, the parasitic resistor effect is ignored. Eq. (IV.1) and Eq. (IV.2) describe the relationship between input and output voltage, and current of buck-boost with respect to duty cycle:

$$V_{out} = \frac{D}{1-D} V_{PV\_\mathrm{mod}} \tag{IV.1}$$

$$I_{out} = \frac{1-D}{D} I_{PV\_\mathrm{mod}} \tag{IV.2}$$

where the V_{out} and I_{out} represent the output voltage and current of buck-boost, respectively, and $I_{PV_mod}$is the current of PV module. Since $V_{out}= R_L I_{out}$, the duty cycle formula can be reformulated from Eqs. (IV.1)-(IV.2) as follows:

$$\sqrt{\frac{R_{PV}}{R_L}} = \frac{1-D}{D} \tag{IV.3}$$

where R_{PV} is the equivalent resistance seen by PV module. From Eq. (IV.3), $D = f(R_L, R_{PV})$ can be simplified as follows [7]:

$$D = \frac{1}{1+\sqrt{\dfrac{R_{PV}}{R_L}}} = \frac{1}{1+\sqrt{\dfrac{0.8V_{oc}/I_{MPP}}{R_L}}} \tag{IV.4}$$

where $R_{PV} = V_{MPP} / I_{MPP}$.It can be seen that the formula of the ratio of D is made depending on the PV module characteristics and load resistance. In MCSL-MPPT method, the number of bypass diodes (n) is exploited. The algorithm requires this number and the V_{oc_mod}. Since each part of the string can be subjected to different G, the start of the search at MPPs (local-global peaks) has to be in the optimal region of the P-D or Q-D curve i.e., $P=f(D)$, or $Q=f(D)$ (cf., Fig. IV.3). Thus, P and Q for each module of PV string can be written as:

$$\begin{aligned} P_{PV\_mod\ 1,2,3,4} &= P_{PV\_mod}(D(n))\big|_{n=1,2,3,4} \\ Q_{\ 1,2,3,4} &= Q\ (D(n))\big|_{n=1,2,3,4} \end{aligned} \tag{IV.5}$$

Unlike the conventional hill-climbing methods, the proposed approach is developed based on *Q-D* characteristics instead of the *P-D* characteristics. Fig. III.2 illustrates the perturbation of *Q* with respect to *D* and the projection on *P-D* as well as *V-D* characteristics. The objective is to annul *Q*; i.e., operating around zero to guarantee accurate MPP tracking (local-global).

In particular, as depicted in Fig. IV.2, the PV string is subjected to different solar irradiance values, which are set to 1, 0.8, 0.7, and 0.6 kW/m^2. As it can be seen that the operating points at multiple peaks exist with respect to optimal values of *D*, which also exists approximate to k×0.8×V_{oc_mod}. The value of duty cycle at GMPP (D_{GMPP}) is generated directly from MCSL-MPPT controller, which is given as follows [10]:

$$\begin{aligned} P_{GMPP} &= max\left(P_{MPP1}, P_{MPP2}, P_{MPP3}, P_{MPP4}\right) \\ D_{GMPP} &= D\ (P_{GMPP}) \end{aligned} \tag{IV.6}$$

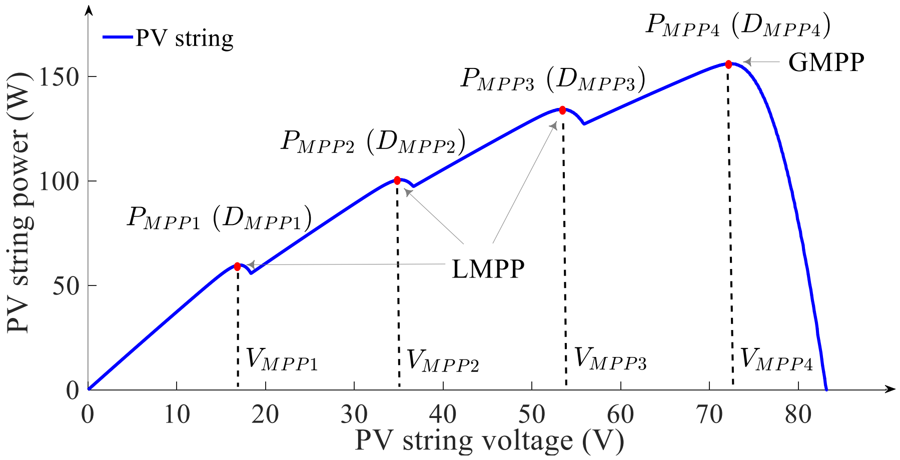

Figure IV.3. *P-V* curve of the one pattern of PV string containing four MPP peaks.

As mentioned earlier, during PSCs, the PV curve would be characterized by a multiple peaks curve, which is defined as an integral multiple obtained from 80% of V_{oc_mod} (i.e., $k \times 0.8 \times V_{oc\_mod}$). Based on these facts, calculating the lower and upper limits of duty cycle for buck-boost converter is involved. Depending on the works of [5,9], the duty cycle range can be expressed as:

$$D_{n\text{-}min} = \left. \frac{1}{1+\sqrt{\dfrac{R_{PV}/n}{R_L}}} \right|_{n=1,2,3,4} \tag{IV.7}$$

$$D_{n\text{-}max} = \left. \frac{1}{1+\sqrt{\dfrac{qR_{PV}/n}{R_L}}} \right|_{n=1,2,3,4} \tag{IV.8}$$

where n is the number of bypass diodes in series, and $q = 10$ is the ratio of the lower and upper values of solar irradiances. These values are set to 1000 W/m^2 and 100 W/m^2, respectively, as in [5].

R_{PV} value is obtained from the ratio of V_{MPP}/I_{MPP}, where R_{PV} changes by the environment parameters and the PV module characteristic. The equation that calculates the voltage and current at MPP of the PV module was expressed as:

$$V_{MPP} = 0.8 \times V_{OC} \tag{IV.9}$$

$$I_{MPP} = 0.9 \times I_{SC} \tag{IV.10}$$

where I_{SC} is the short-circuit current. Since the operating point is operated at MPP, the I_{MPP} is to be equal to $0.9I_{SC}$ as pointed out in literature [11].

IV.2.1.3 Flowchart of the proposed MCSL-MPPT method

The complete flowchart of the proposed MCSL-MPPT method is represented in Fig IV.4. To implement the proposed method, the manufacturer datasheet is taken into consideration; the setting and assigning of the following variables have to be initialized: V_{oc_mod}, I_{SC}, D, n, Q_{th}, and Q. In terms of operating principles, the proposed method is described hereafter:

The state of Q behaves as an unstable system during the start-up and when the sudden irradiance changes since its value is increased and then decreases at certain points, whereas the value of Q is oscillated around zero in the steady-state [12]. A fixed climbing factor (step-size) is insufficient to effectively behave to the MPPT controller during the PSCs. Concerning the proposed MPPT process, the adaptive climbing factor ($D_S \times \Phi_D$) is established to make the tracking process fast and minimize the perturbation step-size at steady-state oscillation in order to enhance the GMPP tracking efficiency. The latter was formulated below:

$$D(k+1) = D(k) \pm D_S \times \Phi_D \tag{IV.11}$$

where$\Phi_D$is a small factor of D_S. The latter is activated when Q is greater than $|Q_{\text{th}}|$, where Q_{th} is the threshold of Q.

As revealed in MCSL-MPPT algorithm, when duty cycle activates at the initial step on the right side of the PV curve the main function starts scanning from the right local region. Fig. IV.4(a) effectively explains the steps of global exploration improvement. The counter is involved to detect the local MPP in order to achieve fast peak detection. The GMPP tracking mechanism of the peak detection is formulated as follows:

$$\text{if } \left|\sum_{i=1}^{i=5} Slope\right| = \begin{cases} 5 \ldots\ldots\ldots\ldots \\ < 5 \ldots\ldots\ldots \end{cases} \begin{bmatrix} \text{MPPT not converged to stady-state} \\ \text{MPPT converged to stady-state} \end{bmatrix} \tag{IV.12}$$

The proposed algorithm defines the upper and lower limit values of D of every local peak by using the Eqs. (IV.7)-(IV.8). Besides it calculates and then perturbs D for each iteration by using Eq. (II.41), where the duty cycle update will be generated for the next iteration. These processes will be repeated for every iteration as a series of executions. Moreover, duty cycle perturbation will be updated by either $+D_S$ or $-D_S$. Meanwhile, the gradient (i) has been also involved in order to record the state of D when five consecutive iterations occur. For all five perturbations and through decrease or increase of duty cycle, the slope will be either negative or positive due to the operating point at LMPP shifting two times in the same direction and then shifting in the opposite direction again. In the meantime, the evaluation state of Q around zero is activated during the actual and old perturbation. In addition, the detector operates continuously to check PSCs occurrence by the following conditions hold [13]:

$$\left|\frac{\Delta P}{P}\right| > 0.1 \tag{IV.13}$$

$$\Delta P = P_{act} - P_{old} \tag{IV.14}$$

where P is given in Eq. (II.43), and ΔP is the perturbation of the power between the output power in actual and old instant measure. The objective is to annul Q and minimize steady-state oscillation.

To illustrate the operating principle of the proposed algorithm, the partial shading pattern shown in Fig. IV.3 is considered. The MCSL-MPPT algorithm starts the search from the extreme lower position of the P-V curve within the first pattern. After identifying the first peak-power $P(1)$ of duty cycle $D(1)$ corresponding to objective function $Q(1)$ at MPP1 (i.e., annulling $Q(1)$) within $0.8V_{oc_mod}$region, D perturbs five steps of (D_S),then decides if the absolute value of the slope equal to 5 or not. If yes, the tracking does not converge to the steady-state. When the latter is less than 5, the search will be stepped to the next region according to Eq. (IV.5) on $2\times0.8V_{oc\_mod}$, due to the tracking convergence on steady-state, as illustrated in Fig. IV. 4(c)-*LMPPT subroutine process*-. The algorithm repeats the search process until identifying the second peak-power $P(2)$ of $D(2)$, i.e., annulling $Q(2)$. The latter continuously operated using the same manner until reaching the terminus region i.e., $4\times0.8V_{oc\_mod}$. In this time, the algorithm judges between the maximum power of the multiple peaks i.e., max (P_{MPP1}, P_{MPP2}, P_{MPP3}, P_{MPP4}) according to Eq. (IV.6), after that, it stops the search because the GMPP has been tracked. The algorithm will be operating under duty cycle of GMPP (D_{GMPP}) i.e., $Q(D_{GMPP})$ to guarantee the annulling Q at this region. Continuing the GMPP tracking, the latter starts the checking on tracking process task to determine whether a new pattern occurs or not. If it does not occur, the gain $\Delta P/P$ will be less than 0.1. If a new pattern occurs, $\Delta P/P$ to be greater than 0.1 as shown in Fig. IV.4(b)-*GMPPT subroutine process*-. At this moment, the search process will start again from [D_{1min}, D_{4max}] to track the GMPP of the new PSC. The algorithm runs the search using the same manner until it reaches GMPP2. It repeats the judgment between the multiple peaks and then stops the exploration when guaranteed that GMPP2 is tracked.

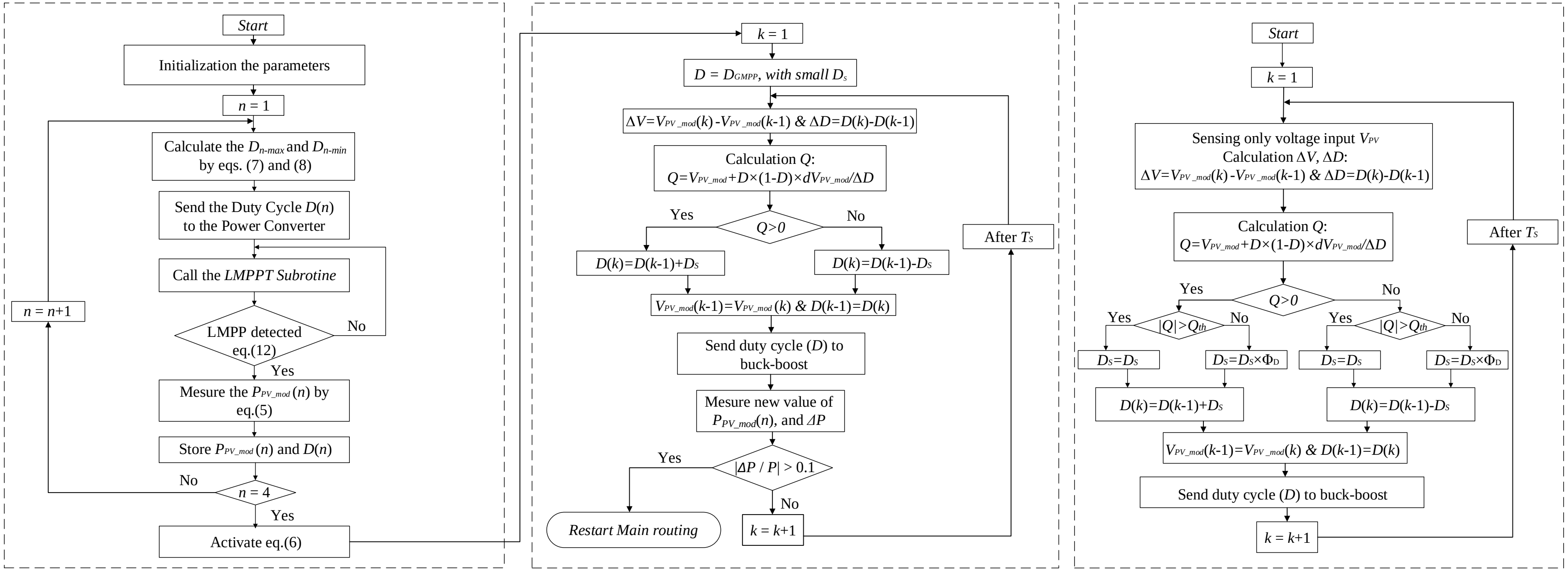

Main routing to track GMPP process
(a)

GMPPT Subroutine process
(b)

LMPPT Subroutine process
(c)

Figure IV.4. The flowchart of the MCSL-MPPT proposed method.

IV.3 Experimental evaluation

IV.3.1 Hardware set-up

The capability of the proposed MCSL-MPPT method is tested experimentally using test equipment shown in Fig. IV.5. The Chroma PV array simulation equipment (62000H Modular SAS) provides electrical behavior of the PV array/module exploiting the direct voltage and controlled-current, it yields *I-V* and *P-V* characteristics depending on the PV parameters. The proposed method has been implemented on low power (500 W) DC-DC buck-boost converter, with its specification design: L = 4mH, $C1$ =3300 µF, $C2$ =3300 µF and f = 20 kHz [14], and the resistive load R_L is 10 Ω. The MCSL-MPPT code is uploaded on TMS320F240 DSP, which acts as a controller board inside dSPACE DS1104.

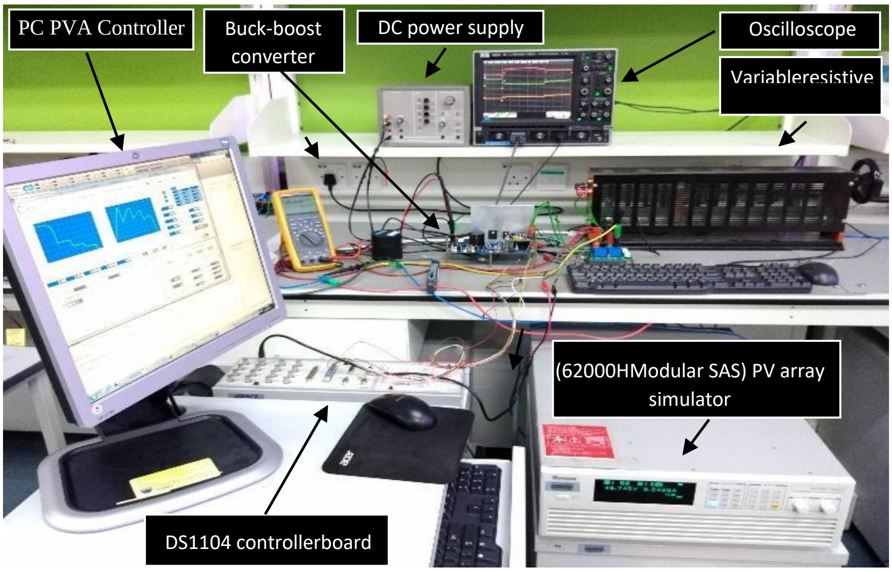

Figure IV.5. Hardware set-up used for the experimental evaluation.

Table IV.1. Characteristics of SUNPOWER SPR-76RE PV Panel at Standard Test Conditions (STC).

Parameters	Labels	Values
Max Power	P_{max}	75.99 W
Max Voltage	V_{max}	13.45 V
Max Current	I_{max}	5.65 A
Short-Circuit	I_{sc}	6.02 A
Open Circuit Vvoltage	V_{oc}	16.2 V
Number of cells	N_S	24

The MCSL-MPPT technique is developed under the finite state tool using the Stateflow in MATLAB/ Simulink/Stateflow environment [15], where the Target Link is utilized to convert the C code for the DS1104 board. The proposed algorithm is carried out depending on a direct control. Only one ADC input signal in this process is needed since the feedback is acquired only using the LV25-P voltage sensor [16]. The sampling time T_S is set to 100 ms, the adaptive step-size D_S is set to 2%, and then Φ_D is set to 0.25%. A PV string of four PV modules i.e., $n = 4$ is emulated using the 62000H modular SAS PV array simulator to validate the proposed method. Thus, the performance of the proposed algorithm is verified under several PSCs. The *P-V* and *I-V* curves of the patterns used for the test are described hereafter:

- ***Case one*:** as it can be seen in Fig. IV.6, there are two patterns, where Fig. IV.6(a) shows pattern one, and Fig. IV.6(b) shows pattern two, both have been deliberately chosen to contain one middle GMPP, and one left side GMPP, respectively. Thus, the patterns used are explained in the next paragraph: At first, the pattern one is subjected to different irradiances G: 0.8, 0.7, 0.6, 0.3 kW/m^2; the highest peak power (GMPP1: 35 V, 160 W) exists at the middle of the *P-V* curve. Pattern two is subjected to different irradiance profile G: 1, 0.4, 0.2, 0.1 kW/m^2; the highest peak power (GMPP2: 35 V, 97 W) exists at the left side of the *P-V* curve.

- ***Case two*****:** in Fig. IV.7, there are two patterns, where, Fig. IV.7(a) shows pattern one and Fig. IV.7(b) shows pattern two, which have been deliberately chosen to contain one right side GMPP, and one left side GMPP, respectively. The patterns used are explained in the next paragraph: At first, pattern one is subjected to different irradiances G: 0.9, 0.7, 0.6, 0.5 kW/m^2; the highest peak power (GMPP1: 52 V, 215 W) exists at the right side of the P-V curve. Pattern two is subjected to different irradiances G: 1, 0.4, 0.2, 0.1 kW/m^2; the highest peak power (GMPP2: 13 V, 76 W) is at the left side of the P-V curve.
- ***Case three*****:** Fig. IV.8(a) shows pattern 1, and Fig. IV.8(b) shows pattern 2. Both patterns have been deliberately chosen to contain one middle side GMPP and one right side GMPP, respectively. The patterns used are explained in the next paragraph: At first, pattern 1 is subjected to different irradiances G: 0.8, 0.7, 0.6, 0.3 kW/m^2; the highest peak power (i.e., GMPP1: 38 V, 160 W) exists at the middle side of P-V curve, and pattern 2 is subjected to different irradiances G: 0.9, 0.7, 0.6, 0.5 kW/m^2; the highest peak power (i.e., GMPP2: 52 V, 215 W) exists at the right side of P-V curve.

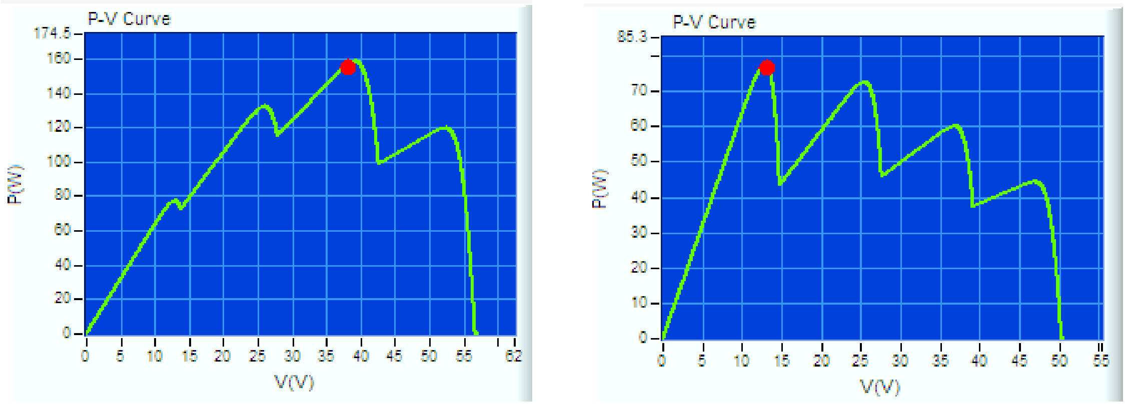

(a) (b)

Figure IV.6. *P-V* characteristics of the PV string under partial shading conditions, (a) Middle GMPPT case, (b) Left GMPPT case.

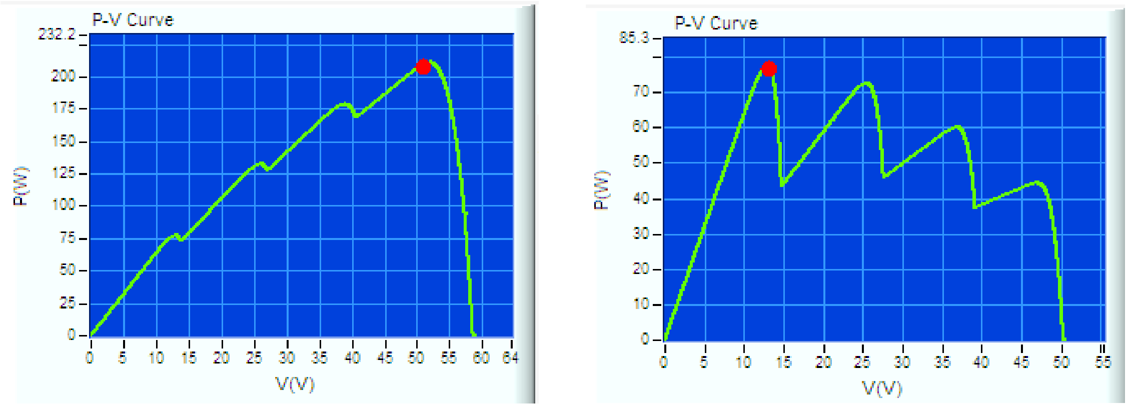

(a) (b)

Figure IV.7. *P-V* characteristics of the PV string under partial shading conditions, (a) Right GMPPT case, (b) Left GMPPT case.

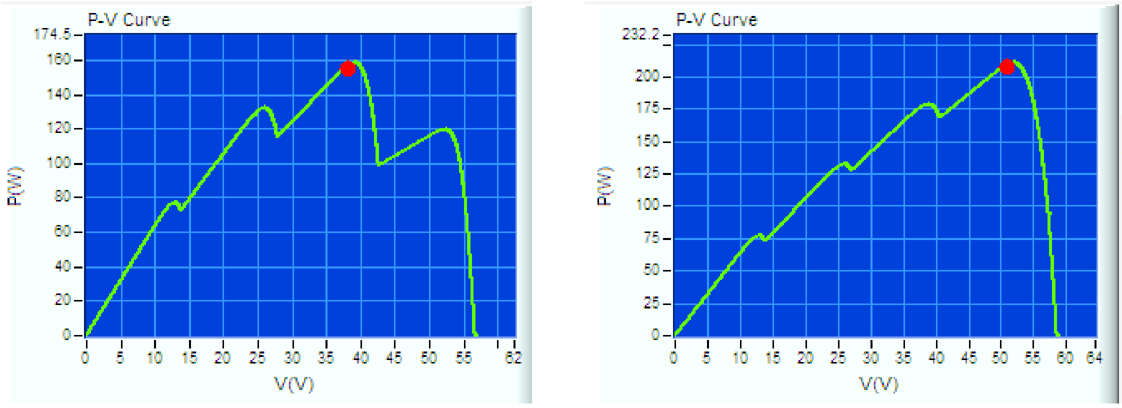

(a) (b)

Figure IV.8. *P-V* characteristics of the PV string under partial shading conditions, (a) Middle GMPPT case, (b) Right GMPPT case.

IV.3.2 Results and discussion

The tracking performance of the proposed algorithm is depicted in the oscillograms of Figs. IV.9, 10, and 11. The PV panel characteristics are listed in Table IV.1. The performance evaluation of the proposed method is presented in Table IV.2. Table IV.3 presents a comparison between the proposed MCSL with some typical methods, where it can be seen that the implementation cost has been reduced by 27.95%. The assessment includes different patterns; the peaks of the PV modules are designed under PSC that are composed of three cases as set hereafter: left side GMPP, middle GMPP, and right side GMPP. The tracking capability of the algorithm has been tested under the transition conditions from one pattern to other patterns (i.e., from middle to left, from right to left, and then from middle to right). The experimental results show the capability of the MCSL-MPPT method, where the steady-state oscillation accuracy i.e., the efficiency of the MPPT is equal to 99.6%. The timer trigger is set to 15 minutes [13]. Consequently, it can be revealed that the algorithm can track the GMPP locus almost perfectly.

It should be mentioned that the proposed method has a limitation. For large-scale PV applications, the tracking time for the global peak will be significant due to the high number of the bypass diodes. The proposed method is suitable for small-scale PV applications.

Table IV.2. Performance Evaluationof the Proposed MCSL-MPPT Algorithm.

PSC Scenarios	Convergence Time to Track GMPP		
	Left Side	Middle Side	Right Side
First Scenario: From Middleside GMPPT to Left side GMPPT Pattern.	2.6 s	2 s	-
Second Scenario: From Right side GMPPT to Leftside GMPPT Pattern.	3.2 s	-	1.6 s
Third Scenario: From Middle side GMPPT to Right side GMPPT Pattern.	-	1.8 s	1.4 s

IV.3.2.1 First Transition of the Patterns

For the first case, the tracking efficiency is depicted in Fig. IV.9(a), where the first global peak (GMPP1) exists at the middle side; and GMPP2 exists at the left side. The algorithm starts the tracking operation in the first, middle side case of the *P-V* curve within the optimal range (i.e., from D_{min1} to D_{max4}). After identifying the global peak power and confirming that the operating point is in the vicinity of annulling Q_{GMPP1} where the algorithm guarantees that GMPP1 is tracked. As it can be seen in the zoomed portion in Fig. IV.19(b), the convergence time is (T_{s_GMPP1} = 2 s). The algorithm scans the second pattern of the *P-V* curve that contains the left side GMPP and then starts the searching again from D_{min1} to D_{max4}. After identifying the global peak and confirming that the operation is near to annulling Q_{GMPP2} where the algorithm guarantees that the GMPP2 is tracked. From the zoomed portion in Fig. IV.9(c), the convergence time of GMPP2 is (T_{s_GMPP2} = 2.6 s). As expected, both patterns, GMPP1 and GMPP2 were tracked effectively in a short period of time by using the proposed MCSL-MPPT algorithm, as depicted in Fig. IV.9(a-b), and (c), respectively.

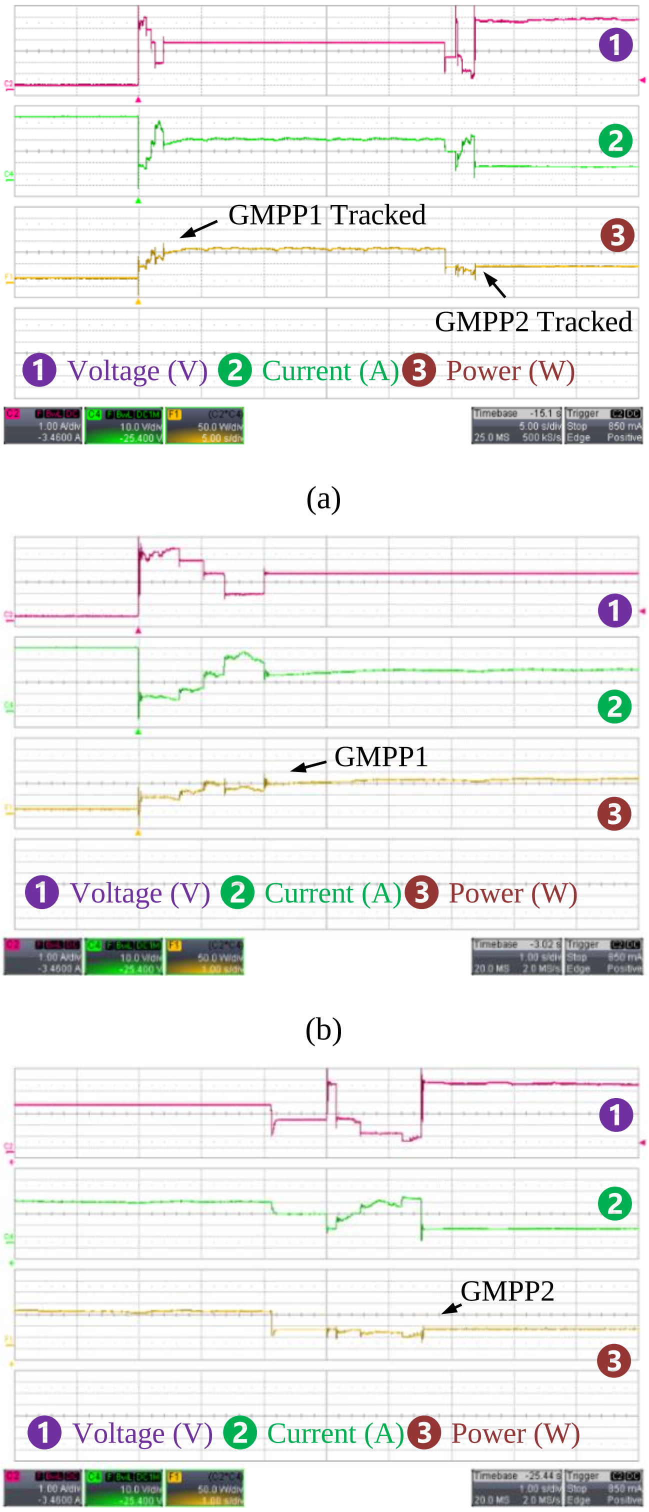

(a)

(b)

(c)

Figure IV.9. Outcomes test waveforms of the voltage, current, and power for the patterns while tracking the proposed method to the GMPP (a) Transition of the tracking from middle to left case. (b) A zoomed portion of the middle GMPPT case. (c) A zoomed portion of the left GMPPT case.

IV.3.2.2 Second Transition of the Patterns

For the second case, the tracking efficiency is depicted in Fig. IV.10(a), where the first global peak (GMPP1) exists at the right side and GMPP2 exists at the left side. The algorithm starts the tracking of GMPP in the right side of the *P-V* curve within the optimal range (i.e., from D_{min1} to D_{max4}). After identifying the global peak power and confirming that the operating point is in the vicinity of annulling Q_{GMPP1} where the algorithm guarantees that GMPP1 is tracked. As it can be seen in the zoomed portion in Fig. IV.10(b), the convergence time is ($T_{s\_ GMPP1}$ = 1.6 s). It scans to the second pattern that contains a left side GMPP and then starts the searching again from D_{min1} to D_{max4}. After identifying the global peak and confirming that the operation is near to annulling Q_{GMPP2} where the algorithm guarantees that the GMPP2 is tracked. As it is obvious from the zoomed portion in Fig. IV.10(c), the convergence time of GMPP2 is (T_{s_GMPP2} = 3.2 s). As expected, both peaks, GMPP1 and GMPP2 were tracked effectively in a short period of time by using the proposed MCSL-MPPT algorithm, as depicted in Fig. IV.10(a-b), and (c), respectively.

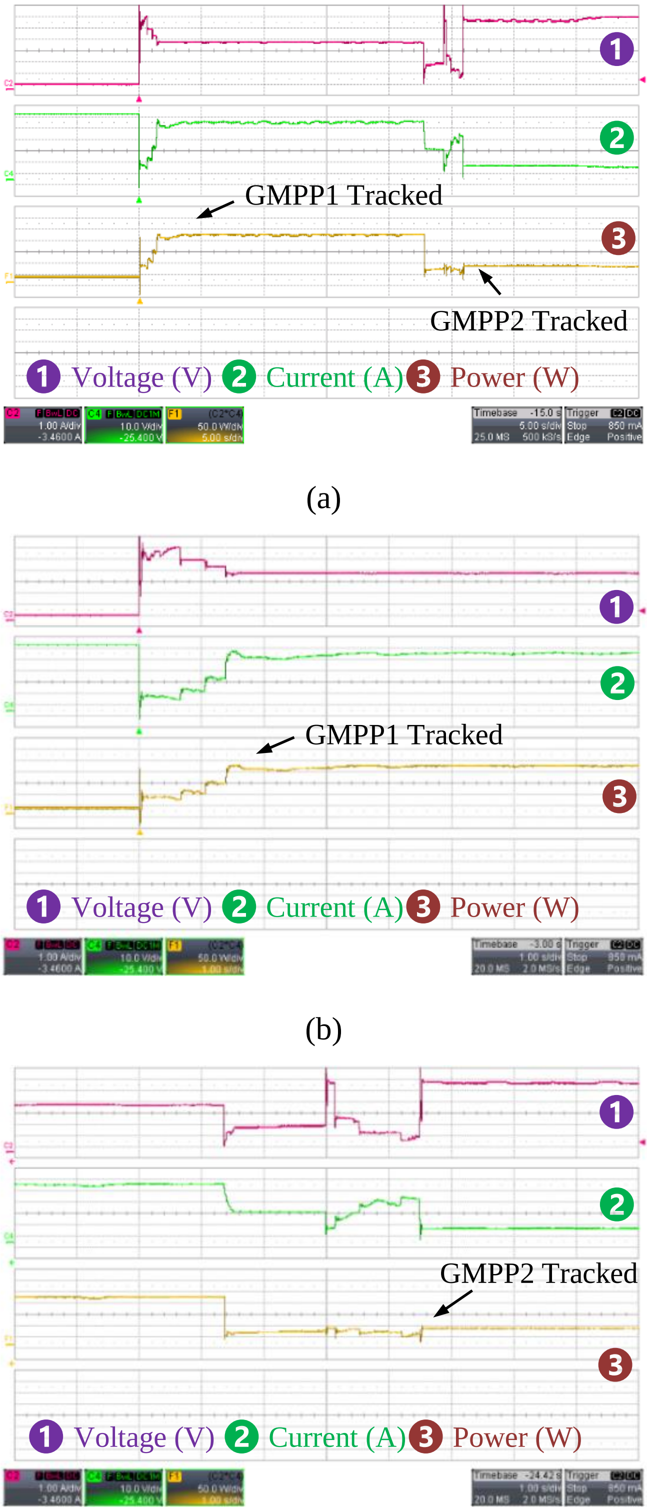

(a)

(b)

(c)

Figure IV.10. Outcomes test waveforms of the voltage, current, and power for the patterns while tracking the proposed method to the GMPP. (a) The transition of the tracking from right to Left case. (b) A zoomed portion of the right GMPPT case. (c) A zoomed portion of the left GMPPT case.

IV.3.2.3 Third Transition of the Patterns

For the third case, the tracking efficiency is depicted in Fig. IV.11(a). The first global peak (GMPP1) exists at the middle and the second global peak (GMPP2) exists at the right side. The algorithm starts tracking the middle GMPP within the optimal range (i.e., from D_{min1} to D_{max4}). After identifying the global peak power and confirming that the operating point is in the vicinity to annulling Q_{GMPP1} the algorithm at this point guarantees that GMPP1 is tracked. As it can be seen in the zoomed portion in Fig. IV.11(b), the convergence time is (T_{s_GMPP1} = 1.8 s). The algorithm scans the second pattern that contains a right side GMPP and then starts the searching again from D_{min1} to D_{max4}. After identifying the global peak and confirming that the operation is near to annulling Q_{GMPP2} where the algorithm guarantees that the GMPP2 is tracked. As obviously in the zoomed portion in Fig. IV.11(c), the convergence of GMPP2 time is (T_{s_GMPP2} = 1.4 s). As expected, both patterns, GMPP1 and GMPP2, are tracked effectively by using the proposed MCSL-MPPT algorithm in a short period of time (cf, Fig. IV.11(a-b), and (c)), respectively.

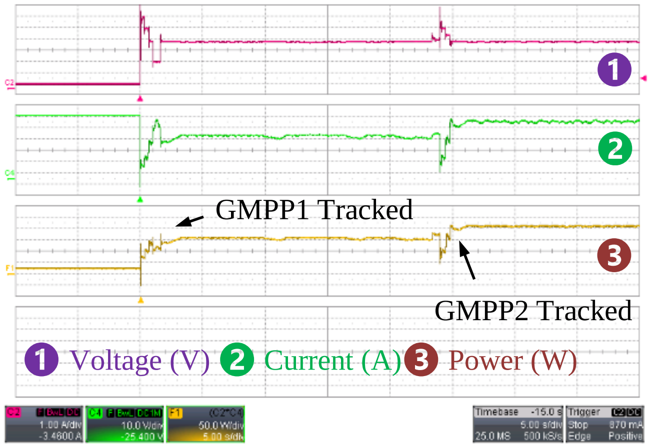

(a)

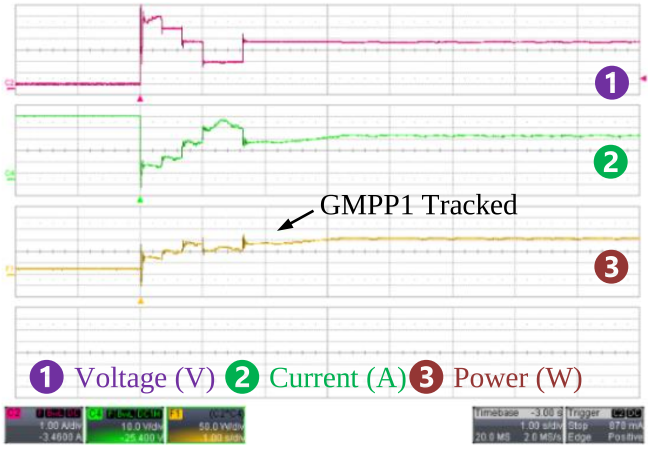

(b)

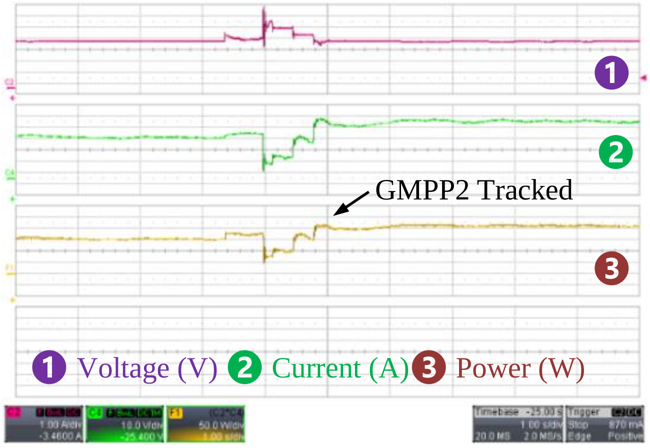

(c)

Figure IV.11. Outcomes test waveforms of the voltage, current, and power for the patterns while tracking the proposed method to the GMPP. (a) Transition of the tracking from middle to right case. (b) A zoomed portion of the middle GMPPT case. (c) A zoomed portion of the right GMPPT case.

Table IV.3. Comparison Between the Proposed MCSL with Some Typical Methods.

Algorithm	Sensor used	Tracking GMPP ability under PSCs	Power efficiency	Cost [16,17]
HC [18]	Voltage and current	No	-	104.27 $
P&P [19]	Voltage and current	No	-	104.27 $
SIV [20]	Voltage	No	-	75.13 $
0.8V_{OC}[6]	Voltage and current	Yes	96%	104.27 $
Modified INC [9]	Voltage and current	Yes	High	104.27 $
ST [21]	Voltage and current	Yes	99.7%	104.27 $
Proposed	Voltage	Yes	99.6%	75.13 $

Moreover, more relevant MPPT techniques were studied which are presented in Table I.3 and assessed with our proposed controller presented in Table VI.4 according to the criteria mentioned in the tables.

Table IV.4. Technical Specifications and Performance Evaluation of the Proposed MCSL-MPPT Approach.

Category		**MPPT algorithm**	**DC-DC Converter used**	**Sensor used**		**Computational burden**	**Steady-state oscillation level**	**Tracking ability under PSC test**	**Sensor cost**
				Current	**Voltage**				
Proposed method	One ADC channel	MCSL	Buck-boost	No	Yes	Low	Low	High	Low

IV.4 Conclusion

A new global maximum power point tracking method for partially shaded PV systems has been proposed in this paper. The scheme was a modified current sensorless approach to track the GMPP. The target is to reduce the cost of implementation of the MPPT technique when the PV system is subjected to PSCs.

The main contributions in our work are highlighted as follows:

- The proposed method is capable of tracking the global peak when the PV system is subjected to PSC without the use of any current sensor. By using the voltage sensor only for the tracking, the cost of implementation is reduced by 27.95%.
- A predefined objective function derived from the mathematical model of buck-boost converter is used in the MCSL-MPPT algorithm approach.
- The direct MPPT control technique is introduced to define lower and upper duty cycle limits for every local peak – thus making the tracking faster. An adaptive step-size gain is also incorporated to reduce the steady-state oscillation.
- The performance of the proposed method is validated experimentally using a real converter prototype where the proposed MCSL-MPPT is implemented on low-cost controller using Stateflow tool from Matlab.

IV.5 References

[1] L. Achour, M. Bouharkat, O. Assas, and O. J. E. Behar, "Hybrid model for estimating monthly global solar radiation for the Southern of Algeria:(Case study: Tamanrasset, Algeria)," vol. 135, pp. 526-539, 2017.

[2] F. Hosseini-Fashami, A. Motevali, A. Nabavi-Pelesaraei, S. J. Hashemi, K.-w. J. R. Chau, and S. E. Reviews, "Energy-Life cycle assessment on applying solar technologies for greenhouse strawberry production," vol. 116, p. 109411, 2019.

[3] H. Ghasemi-Mobtaker, F. Mostashari-Rad, Z. Saber, K.-w. Chau, and A. J. R. E. Nabavi-Pelesaraei, "Application of photovoltaic system to modify energy use, environmental damages and cumulative exergy demand of two irrigation systems-A case study: Barley production of Iran," vol. 160, pp. 1316-1334, 2020.

[4] A. Nabavi-Pelesaraei et al., "Prospects of solar systems in production chain of sunflower oil using cold press method with concentrating energy and life cycle assessment," vol. 223, p. 120117, 2021.

[5] M. E. J. I. T. o. I. A. Başoğlu, "An improved 0.8 V OC model based GMPPT technique for module level photovoltaic power optimizers," vol. 55, no. 2, pp. 1913-1921, 2018.

[6] Z. Bi, J. Ma, K. L. Man, J. S. Smith, Y. Yue, and H. J. I. T. o. I. A. Wen, "An Enhanced 0.8$\text {V} _\text {OC} $-Model-Based Global Maximum Power Point Tracking Method for Photovoltaic Systems," vol. 56, no. 6, pp. 6825-6834, 2020.

[7] M. Kermadi, S. Mekhilef, Z. Salam, J. Ahmed, and E. M. J. I. T. o. E. E. S. Berkouk, "Assessment of maximum power point trackers performance using direct and indirect control methods," vol. 30, no. 10, p. e12565, 2020.

[8] K. Ishaque, Z. Salam, A. Shamsudin, and M. J. A. E. Amjad, "A direct control based maximum power point tracking method for photovoltaic system under partial shading conditions using particle swarm optimization algorithm," vol. 99, pp. 414-422, 2012.

[9] K. S. Tey and S. J. I. T. o. I. E. Mekhilef, "Modified incremental conductance algorithm for photovoltaic system under partial shading conditions and load variation," vol. 61, no. 10, pp. 5384-5392, 2014.

[10] M. Kermadi, Z. Salam, J. Ahmed, and E. M. J. I. T. o. I. E. Berkouk, "An effective hybrid maximum power point tracker of photovoltaic arrays for complex partial shading conditions," vol. 66, no. 9, pp. 6990-7000, 2018.

[11] D. Zhou, H. Liu, H. Ma, X. Wang, X. Zhang, and Y. J. I. T. o. I. T. S. Dong, "Driving behavior prediction considering cognitive prior and driving context," vol. 22, no. 5, pp. 2669-2678, 2020.

[12] M. Killi and S. J. I. T. o. I. E. Samanta, "An adaptive voltage-sensor-based MPPT for photovoltaic systems with SEPIC converter including steady-state and drift analysis," vol. 62, no. 12, pp. 7609-7619, 2015.

[13] M. Kermadi, Z. Salam, J. Ahmed, and E. M. J. I. T. o. I. E. Berkouk, "A high-performance global maximum power point tracker of PV system for rapidly changing partial shading conditions," vol. 68, no. 3, pp. 2236-2245, 2020.

[14] I. Shams, S. Mekhilef, and K. S. J. J. o. C. P. Tey, "Advancement of voltage equalizer topologies for serially connected solar modules as partial shading mitigation technique: A comprehensive review," vol. 285, p. 124824, 2021.

[15] M. Kermadi, Z. Salam, and E. M. Berkouk, "A rule-based power management controller using stateflow for grid-connected PV-battery energy system supplying household load," in 2018 9th IEEE International Symposium on Power Electronics for Distributed Generation Systems (PEDG), 2018, pp. 1-6: IEEE.

[16] L. I. SA;. LEM voltage sensor LV 25-P. [Online].

[17] L. I. SA. LEM currentsensor LA 25-NP [Online].

[18] M. Lasheen, M. J. E. c. Abdel-Salam, and management, "Maximum power point tracking using Hill Climbing and ANFIS techniques for PV applications: A review and a novel hybrid approach," vol. 171, pp. 1002-1019, 2018.

[19] V. Jately and S. J. E. Arora, "Development of a dual-tracking technique for extracting maximum power from PV systems under rapidly changing environmental conditions," vol. 133, pp. 557-571, 2017.

[20] M. Killi, S. J. I. J. o. E. Samanta, and S. T. i. P. Electronics, "Voltage-sensor-based MPPT for stand-alone PV systems through voltage reference control," vol. 7, no. 2, pp. 1399-1407, 2018.

[21] S. Hosseini, S. Taheri, M. Farzaneh, and H. J. I. T. o. P. E. Taheri, "A high-performance shade-tolerant MPPT based on current-mode control," vol. 34, no. 10, pp. 10327-10340, 2019.

GENERAL CONCLUSION

General conclusion

In recent years, as a solution to the complex issue of decreasing fossil fuel resources and rising energy demand, photovoltaic solar systems are getting more popular.

The thesis starts with an in-depth review of the different MPPT methods previously suggested in the literature to address both partially shaded and uniform environmental conditions. There are four distinct categories. First, the conventional MPPT techniques, these techniques are based on the perturbing of the duty cycle step by step to clamping toward the right maximum power. These methods actually track the maximum power point. However, they failed in handling partial shading conditions.

The second category of MPPT algorithms was established according to modifications made to the first category technique, which enhanced the stage of searching on GMPP by incorporating additional instructions for faster tracking such as 0.8Voc; this assumed any LMPP exists around the k0.8Voc region. However, the enhancement provided by this technique still used two sensors' information for the right operation to track GMPP.

The third category consists of MPPT algorithms that use a soft computing technique, like particle swarm optimization (PSO). These methods use their effective search and optimization capabilities to locate the GMPP. They have some benefits, like the ability to deal with partial shading conditions, but they also have some major disadvantages, like a high computational burden.

The fourth type is the hybrid MPPT, which uses two or more methods, like combining a conventional method like P&O with a metaheuristic method like PSO. During the search for GMPP, the metaheuristic PSO algorithm gives multiple solutions in each iteration provided by the random numbers in its mechanism of optimization. Even though this method worked, it still used information from two sensors to track the GMPP.

The *P-V* path and the use of two sensors in its work are attributed to the lack of any attempt to use another path in the process of tracking GMPP.

In the following chapters of the thesis, a performance assessment of the typical DC-DC converters for MPPT control i.e., buck, boost, and buck-boost-based control methods are studied. An in-depth analysis of the *P-D* characteristics as well as the (PV-Converter) objective function *Q-D* characteristics is performed.

Under the same testing situations, three topologies are analyzed, and their behaviors are studied in terms of the operating region. The results exhibit an existing non-operational region under large irradiance and load changes for the buck and boost converter. In contrast, compared to the buck-boost converter, this operates in the full operation region for *P-D* and *Q-D* characteristics and performs solutions better than the other topologies.

The primary objective of this research is to reduce the number of sensors used for MPPT controllers. And then, the purpose of providing the tracking capability under partial shading conditions using only a voltage sensor.

This scheme combines the modified current sensorless CSL and a 0.8*Voc*. The improved CSL incorporates the adaptive step size (ASS) mechanism to minimize the region within the *P-V* curve that is determined by 0.8*Voc*. MCSL is improved by incorporating mechanisms that detect LMPP quickly and skip regions that do not have LMPP. The proposed scheme offers several advantages: (1) it is unnecessary to use a current sensor, (2) the steady state is enhanced, and (3) the GMPP tracking is guaranteed under different partial shading scenarios.

The performance of the proposed methods are evaluated using an experimental prototype based on PV array simulator and a buck boost converter driven by Arduino Due for the first proposed CSL method and the TMS320F240 DSP on the dSPACE DS1104 platform for the second proposed MCSL.

Future prospects

As perspectives, we can propose the continuity of the following studies:

In future works, we will investigate the use of the current sensorless scheme to track the maximum power for the grid-tied photovoltaic inverters. Involve the proposed methods in the applications of PV storage energy. Combine the proposed MCSL-MPPT method with artificial intelligence methods for diagnosis of photovoltaic system faults. Use the proposed method in electric vehicle (EV) charging.

APPENDICES

APPENDIX I

Simulink model of the photovoltaic module

A.I.1 Simulink model of the photovoltaic module 85 W

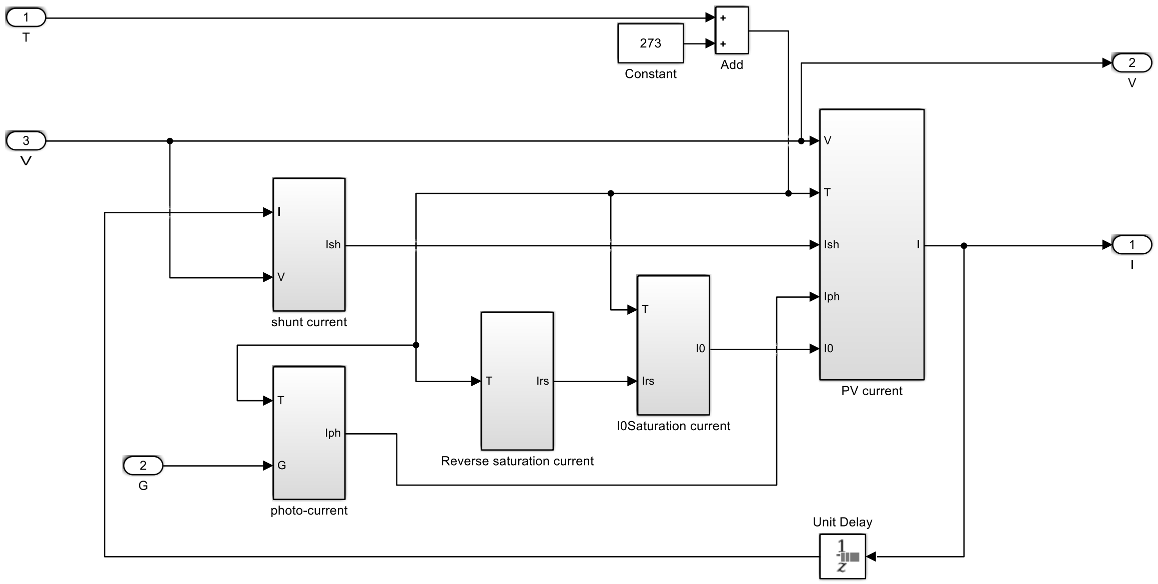

Figure A.I.1 A complete Simulink model of the PV module.

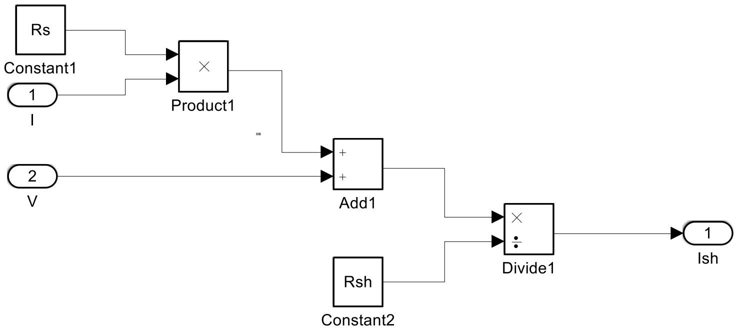

Figure A.I.2 Shunt current of the PV module.

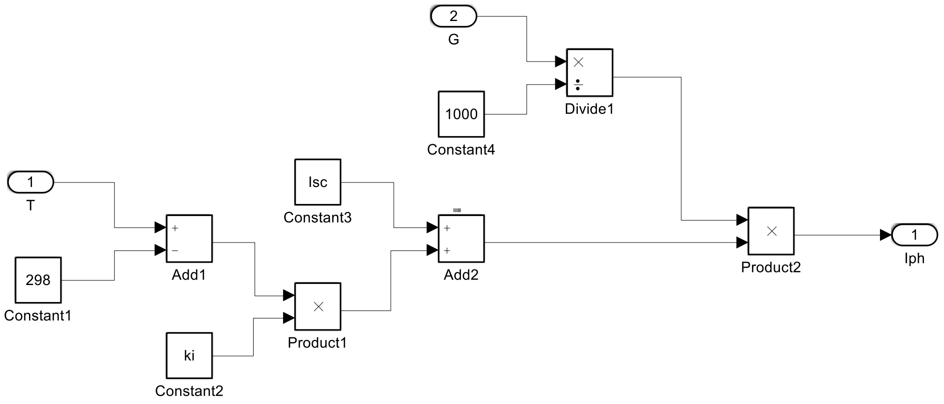

Figure A.I.3 Photo-current generated by the PV cell.

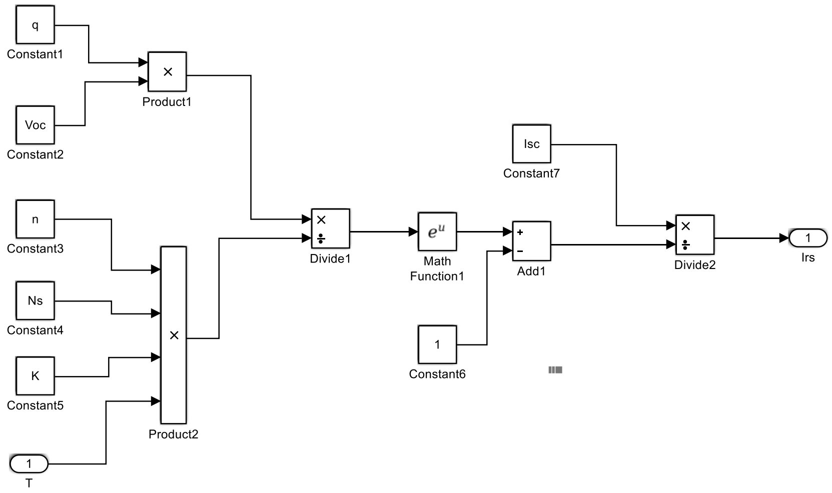

Figure A.I.4 Reverse saturation current of the PV cell.

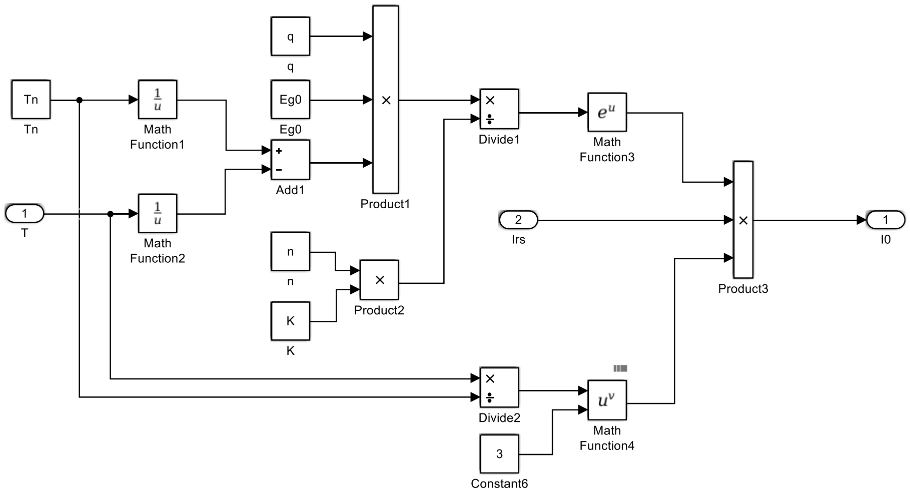

Figure A.I.5 Saturation current of the PV cell.

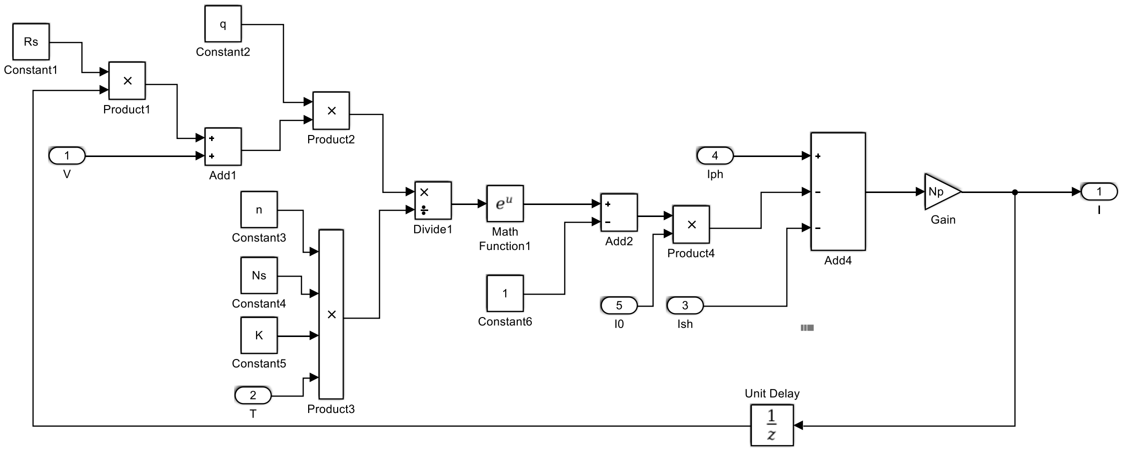

Figure A.I.6 PV current generation block.

APPENDIX II

Design and technical specification of the DC-DC converters

A.II.1 Technical specification and design of buck converter

At standard condition test STC, the PV source circuit should be working at MPP as can be seen by V_{MPP} and I_{MPP} where the duty cycle for buck converter is given by the following formula:

$$D = \frac{V_{O\_\mathrm{MAX}}}{V_{MPP}}$$

where V_{O_MAX} is the maximum output voltage that can be generated by the converter.

The value of the inductance L and the capacitance C_{in} can be calculated by the following equations respectively:

$$L = \frac{V_{O\_\mathrm{MAX}}\left(1-D\right)}{\Delta I_L f_{sw}}$$

$$C_{in} = \frac{I_{MPP}\left(1-D\right)}{\Delta V_{PV} f_{sw}}$$

These values are considered with the assumption that the converter is working in continuous conduction mode (CCM).

A.II.2 Technical specification and design of boost converter

Regards to the standard condition test STC, the PV source circuit should be working at MPP as can be seen by V_{MPP} and I_{MPP} where the duty cycle for boost converter is given by the following formula:

$$D = 1 - \frac{V_{MPP}}{V_{O\_\mathrm{MAX}}}$$

where V_{O_MAX} is the maximum output voltage that can be generated by the converter.

The value of the inductance L and the capacitance C_{in} can be calculated by the following equations respectively:

$$L = \frac{V_{MPP} D}{\Delta I_L \, f_{sw}}$$

$$C_{in} = \frac{\Delta I_L}{8 \Delta V_{PV} \, f_{sw}}$$

These values are considered with the assumption that the converter is working in continuous conduction mode (CCM).

A.II.2 Technical specification and design of buck-boost converter

Regards to the standard condition test STC, the PV source circuit should be working at MPP as can be seen by V_{MPP} and I_{MPP} where the duty cycle for buck-boost converter is given by the following formula:

$$D = \frac{V_{O\_\mathrm{MAX}}}{V_{O\_\mathrm{MAX}} + V_{MPP}}$$

where V_{O_MAX} is the maximum output voltage that can be generated by the converter.

The value of the inductance L and the capacitance C_{in} can be calculated by the following equations respectively:

$$L = \frac{V_{MPP} D}{\Delta I_L \, f_{sw}}$$

$$C_{in} = \frac{I_{MPP} \left(1 - D\right)}{\Delta V_{PV} \, f_{sw}}$$

These values are considered with the assumption that the converter is working in continuous conduction mode (CCM).

APPENDIX III

Configuration of the PWM using assembly code

A.III.1 Microcontroller Atmel SAM3X8E (Aduino DUE)

In this study, it is worth noting the attractive characteristics of Microcontroller (MCU) in Arduino Due board as depicted in Table A.III.A and Fig.A.III.1 such as the processor speed clock of 84 MHz. Fig.A.III.1 shows that 32-bit registers also have great flexibility in generating the PWM unlike the other microcontroller boards, which have the ability to control eight separate channels, and each channel can control two outputs with opposite signals. In this study, as mentioned in Fig.A.III.2 and Fig.A.III.3 it can be an easy way to configure these peripheries through the user interface and also the same way for duty cycle and dead time etc. On the other hand, all channels can synchronize with each other, where we can generate a duty cycle at the same time for all these channels. In addition, the internal and external interrupts can also be programmed by the user interface.

TABLE A.III.1

Different features of Arduino DUE				
Arduino DUE Main Characteristic				
Type	Processor	Clock	Width of Register	Digital I/O
ARM Cortex-M3	SAM3X8E	84 MHz	32-bit	54 pins
				12 PWM output
				12 analog input

As it can be seen in Fig. A.III.1, the different speed clocks of the most popular Arduino boards, which can be observed in the Arduino Due, have a faster speed clock compared to the other boards.

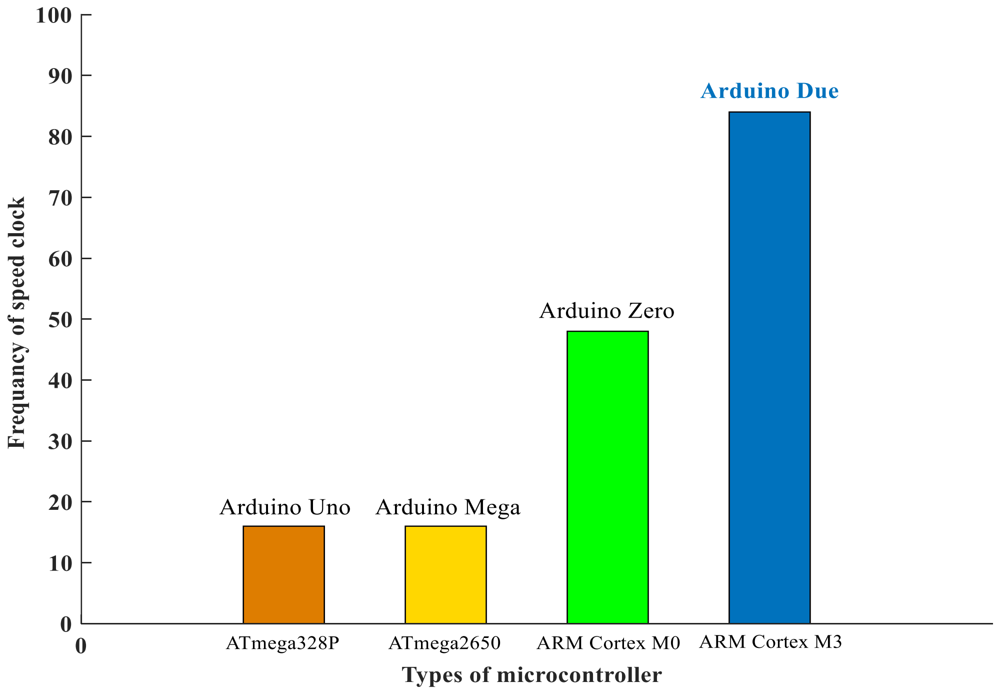

Figure A.III.1. Types of the Arduino boards.

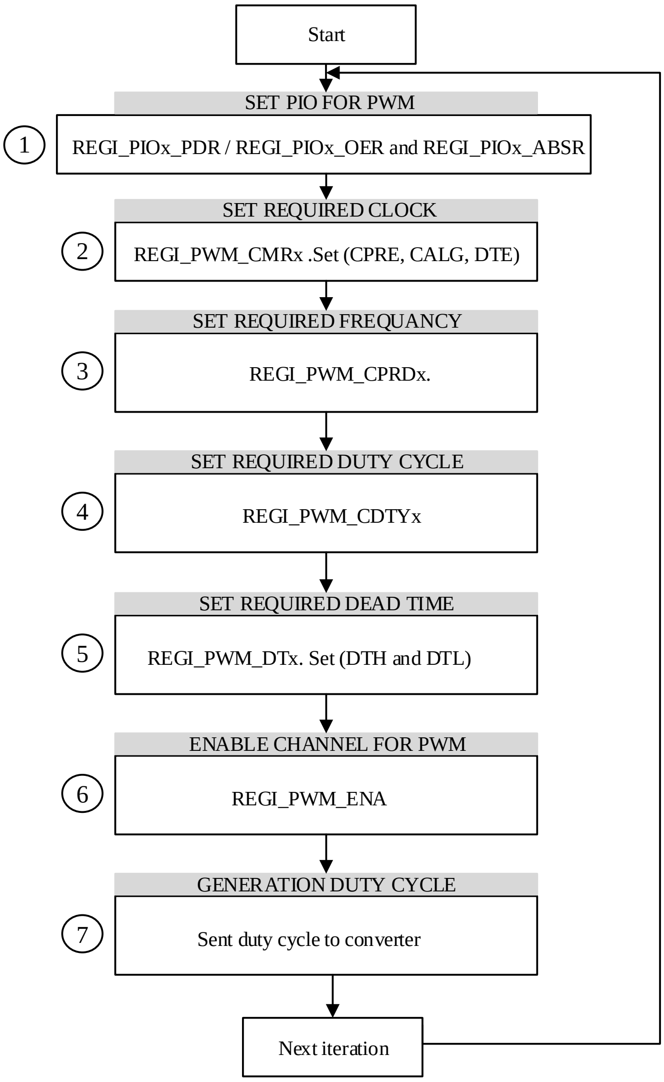

Figure A.III.2 Flowchart of the steps to be followed for generating the PWM with more flexibility

A.III.2 Generation the duty cycle of the PWM

A.III.2.1 Waveform generation period

Generation period for Fast PWM by using the following equation as:

A.III.2.1.1 *Left aligned*

$$T_{period\_PWM} = \frac{Y \times CPRD}{M\_CK}$$

where M_CK is the master clock, which the highest amount of clock can generated by the Microcontroller.

A.III.2.1.2 *Center aligned*

$$T_{period\_PWM} = \frac{2 \times Y \times CPRD}{M\_CK}$$

A.III.2.2 Waveform duty cycle

A.III.2.2.1 *Duty cycle by left aligned mode*

In order to configure the duty cycle for generation-fast PWM the following equation considers the left aligned and the center aligned curve as follows:

$$D_{LA} = \frac{(T_{period\_PWM} - 1/\,f_{ch})CLK \times CPRD}{T_{period\_PWM}}$$

A.III.2.2.2 *Duty cycle by canter aligned mode*

$$D_{CA} = \frac{((T_{period\_PWM}\,/\,2) - 1/\,f_{ch})CLK \times CPRD}{(T_{period\_PWM}\,/\,2)}$$

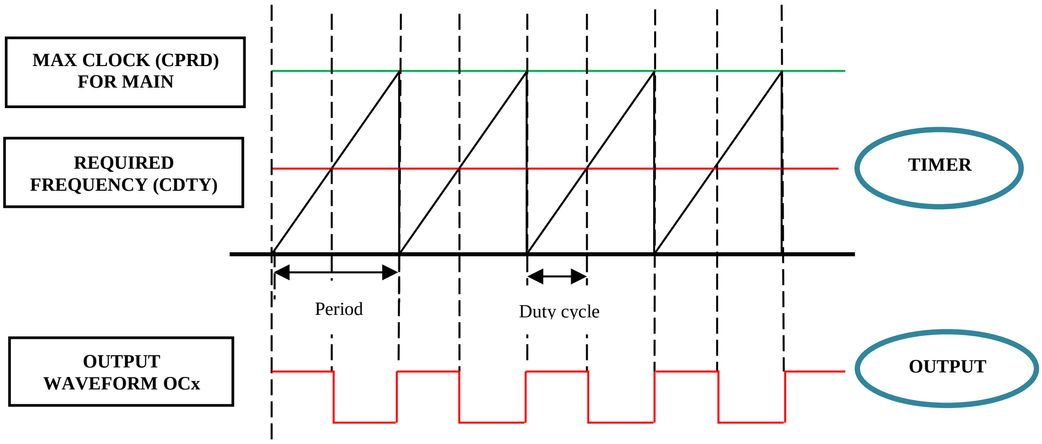

Figure A.III.3 Output waveform of PWM according to Fast PWM configuration.

APPENDIX IV

State flow of the modified current sensorless MPPT technique

As it can be seen in Fig A.VI.1 the stateflow and finite state of the proposed MCSL model-based controller. It provides an efficient MCSL C code generation for hardware implementation. Fig A.VI.1 displays the chart of the MCSL-based MPPT under the Stateflow environment. The MCSL chart is a set of finite states that represent the possible operating modes of the MCSL-MPPT algorithm. The execution steps of the MCSL method are depicted in the flowchart of Fig IV.4 are reproduced in a chart of Fig A.VI.1. Thus, the steps of construction of the MCSL Stateflow chart are presented in Fig A.VI.1 as follows:

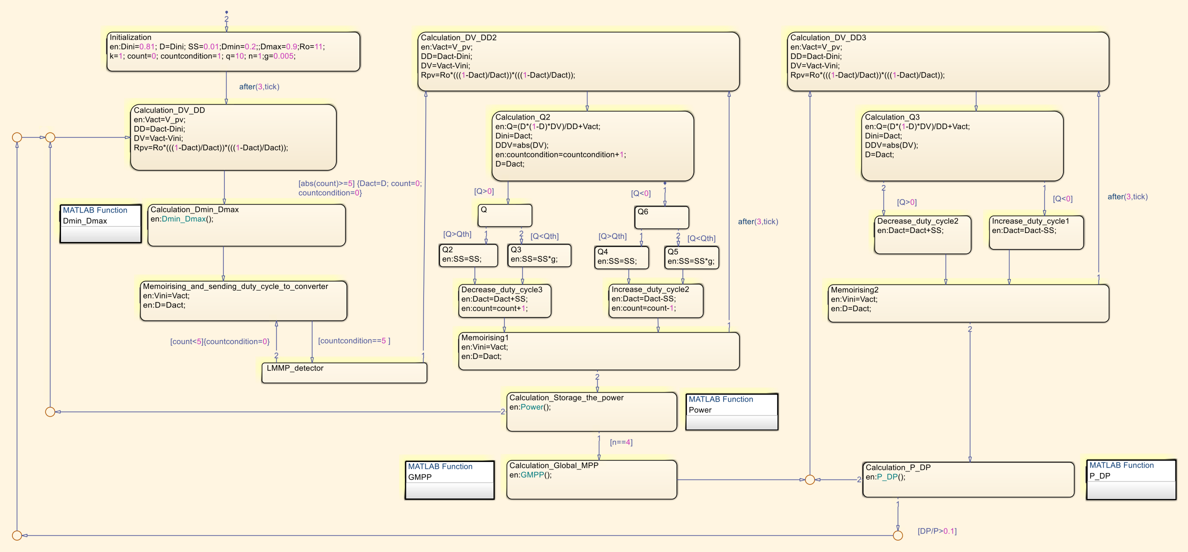

Figure A.VI.1 Stateflow chart of the proposed modified current sensorless MPPT method.

APPENDIX V

List of scientific publications

A.IV.1. List of the international publications

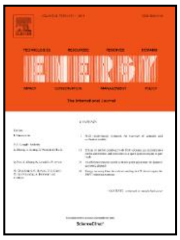

Obeidi Nabil, Mostefa Kermadi, Bachir Belmadani, Abdelkrim Allag, Lazhar Achour, Nadhir Mesbahi, Saad Mekhilef, "***A modified current sensorless approach for maximum power point tracking of partially shaded photovoltaic systems."*** Energy 263 (2023): 125618. Elsevier.

Obeidi Nabil, Mostefa Kermadi, Bachir Belmadani, Abdelkrim Allag, Lazhar Achour, Saad Mekhilef, ***A current sensorless control of buck-boost converter for maximum power point tracking in photovoltaic applications***. Energies, 15(20), 7811. (2022) MDPI.

A.IV.2. List of the national publication

- ✓ Harmonic Filter in its Experimental Environment. In journal: J. Sc. and Tech, Vol. 01, Issue 01, 2019/ ISSN 2676 – 1874.

A.IV.3. List of international conference publications

- ✓ Obeidi Nabil, Bachir Belmadani, Abdelkrim Allag, "***Implementation of a new MPPT Technique for PV systems using a Boost Converter driven by Arduino MEGA***" / December 2018 DOI: 10.1109/CCEE.2018.8634503 Conference: 2018 International Conference on Communications and Electrical Engineering (ICCEE), El oued-Algeria.
- ✓ Improvement of MPPT using a Low Cost Automatic Dry-Cleaning via Robot with DC-DC Converter for Solar Photovoltaic Panels. / The Fifth International Conference on Mechanics and Energy (ICME'2019) and will appear in the ICME'2019 proceeding.

A.IV.4. List of national conference publications

- ✓ Obeidi Nabil, Bachir Belmadani, Abdelkrim Allag, "***Design increment conductance (IncCond) maximum power point tracking controller for buck converter implementation using Arduino DUE board"***/ In University of Batna 2, Algeria.
- ✓ Obeidi Nabil, Bachir Belmadani, Abdelkrim Allag, ***"Digital implementation of MPPT technique for PV systems driven by an embedded board with buck-boost converter"***, Algerian Symposium on Renewable Energy and Materials ASREM2020 Médéa-Algeria.
- ✓ Obeidi Nabil, Bachir Belmadani, Abdelkrim Allag, "***A low cost current sensorless MPPT technique using boost converter based on Stateflow for PV systems***", the first

doctoral sysmposium on technology process, mechanical and electrical engineering (DST’01-2019), hassiba benboouali university of Chlef , Algeria.

- ✓ Obeidi Nabil, Bachir Belmadani, Abdelkrim Allag, “***Performance evaluation of different current sensorless controllers based on DC-DC converter mathematical models for RES***”, the second doctoral sysmposium on technology process, mechanical and electrical engineering (DST’02-2022) hassiba benboouali university of Chlef, Algeria.